

DISS. ETH NO. 27875

TWO-DIMENSIONAL
POLARON-POLARITONS:
INTERACTIONS AND TRANSPORT

A thesis submitted to attain the degree of
DOCTOR OF SCIENCES of ETH ZURICH
(Dr. sc. ETH Zurich)

presented by
PATRICK KNÜPPEL

Master of Science ETH in Physics,
ETH Zurich

born on 07.06.1992

citizen of Austria and Germany

accepted on the recommendation of

Prof. Dr. Ataç İmamoğlu	Examiner
Dr. Iacopo Carusotto	Co-Examiner
Dr. Sylvain Ravets	Co-Examiner
Dr. Jacek Szczytko	Co-Examiner

2021

Abstract

In this dissertation, we explore the interplay between strongly correlated electrons and optical polaritons confined to two dimensions. This is implemented experimentally with gallium arsenide quantum wells hosting a two-dimensional electron gas (2DEG). The structure is further embedded in an optical microcavity to reach the strong light-matter coupling regime. Optically created excitons in the quantum well act as impurities in the surrounding electron gas, forming collective excitations termed Fermi polarons. The resulting polaron-polariton modes are used to study the quantum Hall effect and allow tailoring photonic properties via control over the electrons.

The electronic ground states in the integer and fractional quantum Hall regimes are investigated using polariton spectroscopy. This tool allows probing the spin polarization of the 2DEG by optical means. Many-body spin textures are studied around integer filling, in particular for the case of vanishing g-factor which is expected to favor large skyrmions. Using an optimized device structure, we advance polariton spectroscopy by drastically reducing unwanted modifications of the electron density upon optical illumination. We observe coupling of the polaron-polaritons to different fractional quantum Hall states as the filling factor is varied. In a second part, a polariton Hall bar device is fabricated to investigate the connection between electronic and polariton transport in two dimensions. We demonstrate acceleration of polaritons by shaping the electron density with external electric and magnetic fields. For a spin polarized electron gas, we demonstrate the creation of spin density gradients. They are used to route polaritons on the Hall bar device in a spin selective manner, reminiscent of an optical spin Hall effect. In the last part, we present four-wave mixing experiments performed with polaron-polaritons. The nonlinear optical response of polaritons is measured

while they are coupled to different quantum Hall states. A surprising increase in nonlinear signal is found for the specific filling fractions $2/3$ and $2/5$. These results demonstrate enhanced polariton-polariton interactions both compared to other fillings and to the case of exciton-polaritons without 2DEG. This constitutes a step towards polariton blockade and suggests that nonlinear optics may allow us to extract properties of the correlated electronic states beyond linear spectroscopy.

Kurzfassung

In dieser Dissertation wird das Zusammenspiel von stark korrelierten Elektronen und optischen Polaritonen in zwei räumlichen Dimensionen untersucht. Die experimentelle Realisierung basiert auf Quantentöpfen aus Galliumarsenid in dotierten Heterostrukturen, worin ein zweidimensionales Elektronengas erzeugt wird. Diese Strukturen werden in optische Resonatoren integriert um das Regime starker Kopplung zwischen Licht und Materie zu erreichen. Exzitonen im Quantentopf lassen sich als mobile Störstellen im Fermisee aus Elektronen betrachten, genannt Fermi-Polaronen. Die resultierenden Polaron-Polariton-Moden sind nützlich um den Quanten-Hall-Effekt (QHE) zu untersuchen, sowie um die emittierten Photonen mit neuen Eigenschaften auszustatten.

Bei tiefen Temperaturen und im externen Magnetfeld tritt im zweidimensionalen Elektronengas der QHE ein. Dabei ordnen sich die Elektronen zu exotischen Zuständen, welche wir mittels Polaritonspektroskopie untersuchen. Dieses Werkzeug erlaubt uns die Polarisation der Elektronenspins zu messen. Zusammen mit dem integralen QHE tritt ein ferromagnetisch geordneter Zustand auf, dessen Spintexturen wir studieren. Im Spezialfall eines verschwindenden g -Faktors, welchen wir durch zwei sich kreuzende Landau-Levels im Valenzband erreichen, werden besonders grosse Skyrmion-Texturen erwartet. Wir präsentieren eine optimierte Probenstruktur die weniger anfällig ist auf Veränderungen der Elektronendichte durch optische Anregung und bringen hiermit die Polaritonspektroskopie voran. Damit demonstrieren wir die Kopplung der Polaron-Polaritonen an verschiedene fraktionelle Quanten-Hall-Zustände. Als nächstes fertigen wir eine Probe mit Hallbar Struktur, mit dem Ziel die Verbindung zwischen Transport von Elektronen

und Polaritonen zu erforschen. Mit externen elektrischen und magnetischen Feldern gelingt es uns die Elektronendichte zu verformen, womit wir beschleunigende Potentiale für Polaritonen erzeugen. Weiterhin zeigen wir die Existenz von Gradienten in der Spindichte im Quanten-Hall-Regime. Dies erlaubt uns ein Analogon des optischen Spin-Hall-Effekts zu realisieren und Polaritonen abhängig von ihrem Pseudospin in verschiedene Richtungen zu lenken. Im letzten Teil widmen wir uns den Wechselwirkungen von Polaritonen untereinander. Mithilfe von Vier-Wellen-Mischung charakterisieren wir die optische Nichtlinearität der Polaritonen als Funktion des Füllfaktors. Es präsentiert sich eine überraschend starke nichtlineare Antwort des Systems bei Kopplung an die fraktionellen Zustände $2/3$ und $2/5$. Diese Resultate suggerieren einerseits erhöhte Interaktionen zwischen Polaritonen, andererseits die Möglichkeit mittels nichtlinearer Spektroskopie neue Informationen über Quanten-Hall-Zustände zu gewinnen.

Contents

Abstract	1
Kurzfassung	3
Contents	5
1 Introduction	9
1.1 Scope of this Dissertation	10
2 Cavity QED with Exciton-Polaritons and a 2D Electron System	13
2.1 Introduction to Exciton-Polaritons	14
2.1.1 Quantum Wells based on GaAs Heterostructures . . .	14
2.1.2 Microcavities and Strong Light-Matter Coupling . . .	19
2.2 Introduction to 2D Electron Systems	24
2.2.1 Doped Semiconductor Heterostructures	24
2.2.2 Integer and Fractional Quantum Hall Effects	25
2.2.3 Trions and Exciton-Polarons	28
2.3 Experimental Methods	32
2.3.1 Cryogenic Systems	32
2.3.2 Optical Measurement Setup	35
2.4 Sample Design and Characterization	38
2.4.1 Sample A – Low Density 2DEG	39
2.4.2 Sample B – High Density 2DEG	41
2.4.3 Sample C – Tunable Hole Gas	43
2.5 Polaron-Polariton Spectroscopy	44

3	Polaron-Polaritons in Integer and Fractional Quantum Hall States	49
3.1	Optical Excitations in Magnetic Fields	51
3.2	Landau Quantization and Integer Quantum Hall States . . .	52
3.2.1	Cavity Spectroscopy in the IQH Regime	57
3.2.2	Electronic Spin Polarization and Skyrmion Formation	60
3.2.3	Skyrmions at a Landau Level Crossing	64
3.3	Fractional Quantum Hall States	67
3.3.1	Composite Fermions and Incompressibility	70
3.3.2	Effective Polaron-Polariton Mass	72
3.3.3	High Field and Density Limits	75
3.3.4	Optical Power Dependent Effects	76
3.4	Conclusion and Perspectives	80
4	Transport of Polaritons with External Electric and Magnetic Fields	83
4.1	Experimental Methods and Sample Characterization	85
4.1.1	Polariton Hall Bar	85
4.1.2	Electrical Transport Properties	88
4.1.3	Optical Imaging Setup	89
4.1.4	Cavity Wedge and Polarization Eigenbasis	92
4.2	Polariton Transport by Electric Fields	94
4.2.1	Electron Density Gradients	94
4.2.2	Polariton Acceleration	98
4.2.3	Coupled Oscillator Model	100
4.3	Polariton Transport by Magnetic Fields	105
4.3.1	Acceleration by Hall Voltage	105
4.3.2	Spin Density Gradients	105
4.3.3	Polariton Spin Sorting	108
4.4	Conclusion and Perspectives	111
5	Polariton Interactions in the Fractional Quantum Hall Regime	113
5.1	Experimental Methods and Polariton Spectroscopy	115
5.1.1	Setup and Linear Polariton Spectroscopy	115
5.1.2	Time-Resolved Four-Wave Mixing Setup	117
5.2	Time-Resolved Interaction Measurements	122
5.2.1	Enhanced Nonlinear Response at Fractional Fillings .	122

5.2.2 Interactions and Kerr Model for an Intrinsic QW . . .	128
5.2.3 Interaction Strength in FQH States	131
5.2.4 Increase of Polariton Coherence Time	136
5.3 Conclusion and Perspectives	137
 6 Summary and Outlook	 139
 Bibliography	 143
 List of Figures and Tables	 171
 Acknowledgments	 175
 Curriculum Vitae & Publication List	 177

Chapter Introduction

1

During the 20th century, tremendous progress was made in understanding the microscopic laws of nature. Quantum mechanics took many mysteries out of atoms and helped to make sense of the materials that surround us. Quantum electrodynamics unified the description of atoms and photons and their interactions. Our ability to control and manipulate quantum states in the laboratory has grown astonishingly, leading to the implementation of ideas once put forward as thought experiments. This has led to a deeper understanding of—while also highlighting remaining philosophical problems with—the fundamentals of quantum mechanics and is spurring applications in quantum communication and information processing [1]. One of the biggest challenges is the drastic increase of complexity of a microscopic description of matter as the number of particles is increased. Its exponential scaling renders it intractable for classical computers, in most cases already in the two-digit range of particle numbers. A way forward was proposed by Feynman [2] suggesting to use quantum machines to simulate other physical systems and to check the sufficiency of our descriptions thereof.

One such strategy constitutes quantum simulation with photons [3, 4]. Their greatest advantages lie in their almost lossless transmission through free space, optical fibers or wave guides and the many degrees of freedom offered by electromagnetic modes to encode information. However, it is difficult to engineer the interactions necessary to create entanglement, the primary resource for quantum operations. A potential remedy is provided by strong light-matter interactions where polariton modes emerge. They are hybrid particles between light and matter, inheriting their properties from both constituents. The goal is to leverage suitable materials to enhance entanglement generating interactions. A promising example are Rydberg atoms, for

which single photon blockade has been achieved [5–7]. This entails an interaction strong enough for a single photon to prevent the injection of a second one, thereby also realizing a single photon source. Another example is given by excitons, bound electron-hole pairs in semiconductor materials, which led to many exciting discoveries [8, 9]. Most notably, the interactions inherited from excitons allowed for the observation of Bose-Einstein condensation [10] and superfluidity [11] of polaritons. Simulators based on exciton-polaritons [12–16] are being developed, where the technology of semiconductor fabrication and integrated photonics could be leveraged [17, 18]. This might be beneficial to scale the system to larger numbers of particles, compared to an optical lattice arrangement or cloud of Rydberg atoms. Current limitations of exciton-polaritons are their weak inter-particle interaction strength and the difficulty to manipulate them with external control fields due their electrical charge neutrality. Our approach combines this exciton-polariton platform with a two-dimensional electron gas (2DEG) [19]. This combination provides new degrees of freedom to modify the material resonances that hybridize into polaritons. Immersing exciton-polaritons in the Fermi sea of electrons constitutes an impurity problem interesting in its own right, the Fermi polaron [20, 21]. Furthermore, the 2DEG on itself has prospects for topological computation [22] and photons might be used to measure and manipulate the associated anyons [23, 24] or to emulate their behavior [25–27].

1.1 Scope of this Dissertation

In the following chapter, we review the elements that form the constituents of our experimental platform: quantum wells with excitons as their elementary optical excitations and optical microcavities. These are the tools that allow for reaching the strong light-matter coupling regime and thereby the hybridization of light with matter to create polaritons. The two-dimensional (2D) electron gas is introduced, which hosts the quantum Hall (QH) effect in an external magnetic field. We introduce the experimental methods employed to perform optical spectroscopy at cryogenic temperatures as well as the design and characterization of the heterostructures under study. Equipped with these ingredients, we delve into the combined system, where

polaron-polaritons are created which are both sensitive to the electron gas through Coulomb interactions and directly accessible to optical spectroscopy due to their photon component.

Chapter 3 introduces polaron-polaritons from the vantage point of a spectroscopy tool. Coulomb interactions are responsible for the dressing of excitons with electron-hole pair excitations in the 2D electron gas. But when the electronic ground state evolves from a weakly interacting Fermi sea to correlated QH states, also the coupling to excitons is drastically modified. This renders polaron-polaritons susceptible to the properties of the electronic ground state. A phenomenology of polaron-polariton spectra in the integer and fractional quantum Hall regimes is presented. Through polarization resolved spectroscopy, we can assess the electronic spin polarization. Using this tool, we study skyrmions which are many-body excitations accommodating charge excitations out of quantum Hall states. On the technical side, the robustness of the developed heterostructures to undesired perturbations due to optical excitation is demonstrated.

In Chapter 4, we begin to explore the polaron-polariton platform from the opposite perspective—instead of probing the quantum Hall phases by polariton spectroscopy, we use the matter component to engineer functionalities for polaritons and thereby the emitted photons. By tailoring the electron gas, we find a new way to route polaritons, a step towards engineering artificial gauge fields for polaritons [28], addressing one of the main limitations of exciton-polaritons. We developed a polariton Hall bar device to explore the interplay between optical and electronic transport. With this, we demonstrate the creation of electron density gradients across the 2DEG. These density gradients provide means to accelerate polaritons across the Hall bar using external electric and magnetic fields. In external magnetic fields, we are able to convert density gradients to spin density gradients, which in turn allow for polarization selective acceleration of polaritons.

Finally, polariton interactions are studied in Chapter 5, providing previously unexplored possibilities to move towards the strongly interacting limit. A four-wave mixing setup is introduced to extract the nonlinear optical response of polaron-polaritons. We benchmark our method using exciton-polaritons, then probe polariton interactions as they are coupled to different electronic ground states. Strikingly, we find an enhanced response for the quantum Hall states $\nu = 2/5$ and $\nu = 2/3$. The result suggests enhanced

1. Introduction

polariton-polariton interactions strengths relative to both neighboring fillings and to the intrinsic exciton-polariton case. This motivates further studies of the photon correlations emerging at these filling factors with prospects for photon blockade [29–32]. While open questions remain about the underlying mechanisms, the fact that the enhanced nonlinearity only occurs at isolated filling factors suggests that nonlinear spectroscopy could reveal signatures of the many-body system not accessible using linear optical or transport measurements.

Cavity QED with Exciton-Polaritons and a 2D Electron System

We introduce concepts this thesis builds upon: two-dimensional electronic and optical systems in gallium arsenide, light-matter coupling and exciton-polariton formation, and the quantum Hall effect. We present experimental methods, as well as the structure of the studied samples and some of the design considerations behind them. We show experiments that characterize those samples and discuss their optical response in the absence of magnetic fields and how it is affected by the presence of a two-dimensional electron gas. Embedding such 2D systems into an optical resonator leads to the creation of polaron-polaritons.

Many surprising physical effects arise in two-dimensional electronic and photonic systems. Most notably, the integer and fractional quantum Hall effects, with discoveries like dissipation-less edge currents, composite fermions and particles carrying fractional charge [33, 34]. For photons, creating confinement creates a low-frequency cutoff which results in a parabolic instead of linear dispersion relation. Bose-Einstein condensation of photons [35] and exciton-polaritons [10] was observed in such circumstances. In the following sections, we outline how we realize a combination of a two-dimensional electronic and photonic system.

2.1 Introduction to Exciton-Polaritons

2.1.1 Quantum Wells based on GaAs Heterostructures

Crystals of gallium arsenide (GaAs) can be produced with very high purity and feature both outstanding optical and electrical properties. For this reason and their properties outlined below, the GaAs family materials are the experimental platform of our choice. The band structure characterizes the single particle energy-momentum relationship of electrons in a crystal. Gallium arsenide is a semiconductor with zinc blende crystal structure. Its band structure is depicted for bulk GaAs in Fig. 2.1(a). The band gap minimum lies in the Γ -valley, i.e. a region without electronic states between valence band and conduction band around zero energy on the y -axis. For a semiconductor at zero temperature, the valence bands are completely filled with electrons (states below zero energy in Fig. 2.1(a)), while the conduction bands (states above zero energy) are empty. The band gap is direct, meaning that the conduction band minimum occurs at the same lattice momentum as the valence band maximum. Since optical photons carry negligible momentum compared to massive electrons, this property leads to favorable luminescence properties. Excited carriers relaxing towards the lowest energy states within the bands can efficiently recombine around the Γ -point. The lowest energy conduction band (cb) corresponds to s -type orbitals ($L = 0$) and has spin $S = 1/2$, with spin projection $s_z = \pm 1/2$ along the z -direction and is therefore two-fold degenerate. The highest energy valence band (vb), on the other hand, is p -like ($L = 1$) with spin $S = 1/2$. The states carrying total angular momentum $J = 3/2$ are labeled heavy holes (hh) for $j_z = \pm 3/2$ and light holes (lh) for $j_z = \pm 1/2$. Only this limited set of bands around the Γ -point will be relevant for our discussions. Spin-orbit coupling ensures that the next closest subband, the split-off valence band with $J = 1/2$, is shifted down in energy by about 340 meV [36]. The dispersion of the energy E with momentum \vec{k} around the band extremum at the Γ -point is approximately parabolic $E(k) = \frac{\hbar^2 k^2}{2m^*}$. Electrons in this band behave almost like free electrons but with a reduced effective mass m^* . For the conduction band in GaAs, $m^* = 0.067 m_e$, with m_e being the free electron mass.

To achieve two-dimensional confinement, GaAs can be interfaced with other materials with different band gap to create heterostructures. Alu-

minium arsenide (AlAs) has almost the same lattice constant (566.1 pm) as GaAs (565.3 pm, at room temperature) [36, 37] which allows alloying them in fractions x into a ternary compound $\text{Al}_x\text{Ga}_{1-x}\text{As}$. For $x < 0.45$, the band gap remains direct but its energy is increasing with x . For a fraction $x > 0.45$, the band gap becomes indirect with the X-valley becoming the lowest energy conduction band state. Combinations of single crystalline materials can be grown by molecular beam epitaxy (MBE) to form heterostructures. Thereby, material properties, as for example the band gap, can be engineered at will within a large parameter space given by all available material combinations. Starting from a GaAs substrate, uniform two-dimensional layers can be grown in the xy -plane with precision down to almost single atomic layers, while the composition of the materials may be varied in the growth or z -direction. The compound $\text{Al}_x\text{Ga}_{1-x}\text{As}$ is prominently used in our heterostructures. In Fig. 2.1(b), empirical approximations to the band gaps E_g are shown for GaAs (black line) and $\text{Al}_{0.19}\text{Ga}_{0.81}\text{As}$ (dashed line) [36, 37] as function of temperature. To good approximation, the band gap $E_g = (1.424 + 1.247x)$ eV [37] depends linearly on the aluminum fraction x , indicated in Fig. 2.1(c) for room temperature (RT), where the black line shows the band gap as function of x . The red curve shows an estimate based on interpolated empirical data for the optical refractive index n [38], also as a function of aluminum content x close to zero temperature (right y -axis in red). This variation of E_g and n is extraordinarily useful to create optoelectronic devices, since the admixture of aluminum content x can be well controlled during MBE growth. It will be used to engineer the electronic and optical properties in our samples.

Effective two-dimensional systems can be realized by restricting the motional degrees of freedom to two dimensions. This is achieved by confining electronic motion in, say, the z -direction which restricts the electron momentum k_z to discrete values. Quantum wells (QWs) that spatially confine both electrons and holes in the z -direction (also called type-I band alignment) can be realized by embedding a low aluminum content region with higher aluminum content on both sides. Such a structure is depicted in Fig. 2.2(a), showing the energy of the band edges for conduction and valence bands and confined states in the GaAs regions. For small enough well width, the motion in the z -direction is quantized into subbands j while the dispersion in the

2. Cavity QED with Exciton-Polaritons and a 2D Electron System

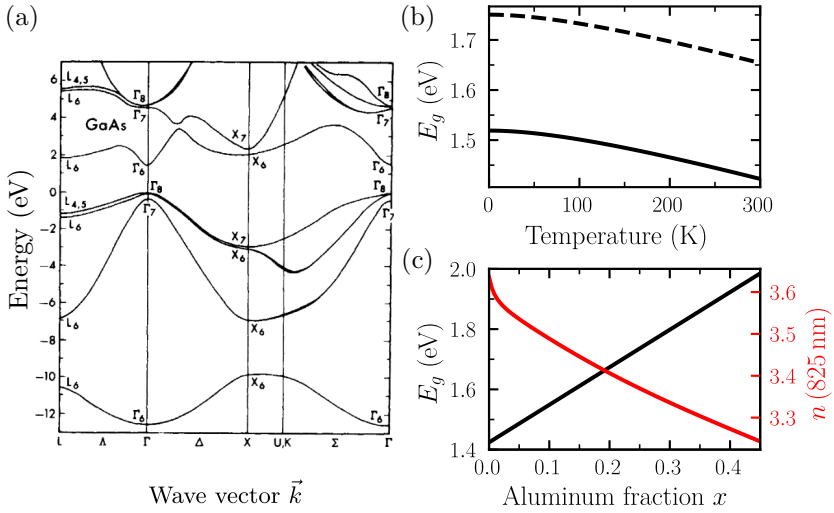


Figure 2.1: Band structure and material properties of GaAs. (a) Band structure calculation for GaAs with direct band gap at the Γ point. Figure adapted from [39]. (b) Band gap E_g of GaAs (solid line) and $\text{Al}_{0.19}\text{Ga}_{0.81}\text{As}$ (dashed line) as a function of temperature [36]. (c) RT Band gap E_g [37] and low temperature optical refractive index n [38] at wavelength 825 nm for $\text{Al}_x\text{Ga}_{1-x}\text{As}$ as a function of aluminum content x . The index of refraction of AlAs at low temperature is 2.95 [38].

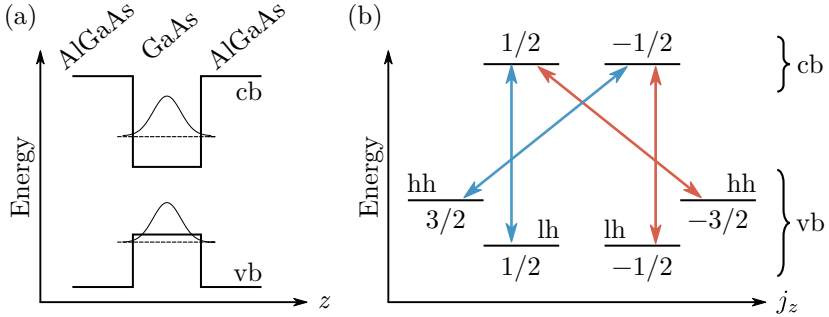


Figure 2.2: Gallium arsenide quantum well and allowed optical transitions. (a) Schematic of a GaAs/AlGaAs QW with confined states in the growth direction (z). (b) Relevant states and selection rules with optically bright transitions marked with red and blue arrows. Spin projections indicated for electrons in the conduction band and total angular momentum of holes (opposite sign for electrons) in the valence band. Blue transitions correspond to exciton / photon spin $m_z = +1$, red to $m_z = -1$.

plane remains parabolic

$$E_j(\vec{k}_{\parallel}) = E_j + \frac{\hbar^2 \vec{k}_{\parallel}^2}{2m^*}, \quad (2.1)$$

with the effective mass m^* not necessarily coinciding with the bulk values. We denote the in-plane momentum with $\vec{k}_{\parallel} = (k_x, k_y)$ and the out-of-plane momentum as $k_{\perp} = k_z$. The confinement also lifts the degeneracy between the light and heavy hole bands [40]. At the interface between GaAs and AlAs, the conduction band offset to valence band offset divides into a ratio of about 65 : 35, hence resulting in deeper potential barrier for the electrons [41].

Optical transitions correspond to photon absorption and emission events. Different types of transitions exist and are subject to various constrains from transition matrix elements and selection rules. We are concerned with inter-band transitions, where an electron is excited across the band gap of the semiconductor forming a band electron-hole pair. It turns out that the lowest energy, elementary optical excitations occur at an energy slightly below the band gap. These excitations, termed excitons, are bound states of an electron

2. Cavity QED with Exciton-Polaritons and a 2D Electron System

and a hole. Disregarding decay or recombination, they are mathematically analogous to the hydrogen atom but at different energy scales. Due to the low effective mass and high dielectric constant ($\epsilon \approx 13$) in GaAs, the binding energy in a 10 nm QW is on the order¹ of $E_B \approx 10$ meV, and the Bohr radius is about $a_B \approx 10$ nm.

Starting with the ground state of the semiconductor as vacuum state $|0\rangle$, we denote with \hat{x}_k^\dagger the bosonic creation operator for an exciton with momentum \vec{k} . The excitons inherit their dispersion from the band structure $E_x(k_{\parallel}) = E_x(0) + \hbar^2 k_{\parallel}^2 / (2m_x)$ with the exciton mass m_x given by the sum of the electron and hole masses. The exciton energy $E_x(k_{\parallel} = 0) = \hbar\omega_x$ corresponds to the optical transition frequency ω_x and contains the confinement energy in the QW as well as the exciton binding energy. The constituting electron and hole can carry angular momentum and spin, which leads to the existence of different exciton species. We consider only the optically active combinations with $|\Delta j_z| = 1$, indicated in Fig. 2.2(b). This schematic shows the relevant electronic states of the hh and lh valence and conduction bands, labeled with their angular momentum projections. Furthermore, we use the ground state excitonic states, i.e. the 1s bands which have the largest binding energy. While the in-plane momentum is conserved during photon emission and absorption events, the QW heterostructure breaks translational symmetry in z -direction. The excitons hence couple to a one-dimensional continuum of radiation modes and spontaneously emit with a rate [43]

$$\Gamma_x = \frac{e^2}{4\epsilon_0 n} \frac{1}{m^* c} f_x \quad (2.2)$$

with oscillator strength f_x per unit area, c the speed of light and ϵ_0 the vacuum permittivity. In the envelope function approximation, the exciton wave function is written as product of an envelope $\chi_{c,v}(z)$ and a function describing the relative in-plane motion of electron and hole $\phi(r_e - r_h)$. Then

¹The values are increased in QWs with respect to the bulk, 3D GaAs case ($E_B = 4.2$ meV [42]) due to confinement and depend on the thickness of the well. These quantities are further modified in a magnetic field or in the presence of itinerant charge carriers.

the oscillator strength reads [43]

$$f_x = \frac{2}{m^* E_g} |p_{cv}|^2 \left| \int \chi_c(z) \chi_v(z) dz \right| |\phi(0)|^2 \quad (2.3)$$

with p_{cv} the inter-band momentum matrix element. For 1s excitons one finds $\phi(0) = \sqrt{8/\pi} a_B^{-1}$, leading to $f_x \propto a_B^{-2}$.

Excitons $\hat{x}_{\vec{k}}^\dagger$ can be well approximated as bosons, behaving as eigenstates of a harmonic oscillator for each \vec{k} . But they are composite particles made up of fermions. Interactions between excitons, especially in the limit of high exciton densities, lead to an anharmonic spectrum. At very high densities $N \geq (\pi a_B^2)^{-1}$ when excitons start to overlap spatially, the Mott transition occurs to unbound electron-hole pairs [44].

2.1.2 Microcavities and Strong Light-Matter Coupling

Optical resonators can store energy in the form of electromagnetic radiation by supporting field patterns (modes) that reproduce themselves after a number of round-trips. They can be used to spectrally filter, store and spatially confine beams of light. The possibility to engineer light-matter interactions makes them a key ingredient for constructing lasers. We will make use of optical microcavities to confine light and thereby enhance light-matter interactions for a quantum well placed at the position of maximum electric field amplitude inside the cavity. Viewed from another perspective, we suppress the spontaneous emission of the QW by removing the electromagnetic continuum of modes in the z -direction and instead provide only one resonator mode k_z for the QW to emit into. We review a few resonator properties before discussing how polariton modes emerge in the strong-coupling regime.

We use one of the simplest resonator designs, the Fabry-Pérot resonator. It consists of a dielectric spacer or cavity layer surrounded by reflecting planar mirrors. The thickness of the spacer is the cavity length L and defines the resonance wavelengths $\lambda_q = 2nL/q$ for $q = 1, 2, 3, \dots$ integers. As mirrors, dielectric layers of optical thickness $\lambda/4$ are stacked with alternating refractive indices. This realizes a distributed Bragg reflector (DBR). A noteworthy difference to a metallic mirror is the penetration of the electric field

2. Cavity QED with Exciton-Polaritons and a 2D Electron System

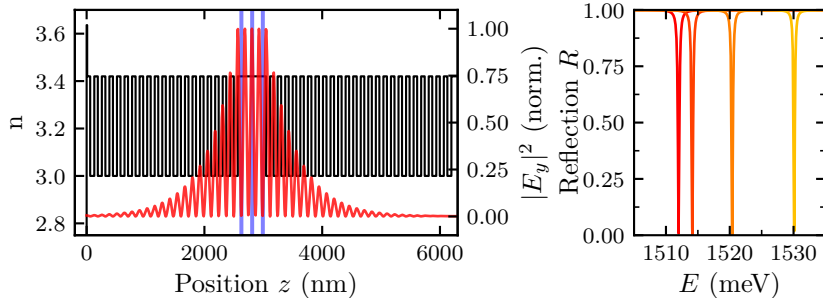


Figure 2.3: Transfer matrix simulation of the optical microcavity of sample A. (a) The electric field (red) is confined to the cavity region in the center by the DBR mirrors with refractive index contrast in black. The blue vertical lines indicate the positions of the QW (center, antinode of electric field) and doping layers (surrounding the QW, nodes of electric field). Top surface at 0 nm. (b) Microcavity reflectivity (s -polarization) for normal incidence 0° (red), increasing to 10° , 20° and 30° (yellow).

into the mirror layers which increases the mode volume [45]. Typically, the refractive index of dielectric DBR layers has a much smaller imaginary part compared to metals, resulting in a reduction of optical losses. The geometry being planar allows to integrate it into one monolithic structure during MBE growth, resulting in a stable and robust resonator. The corresponding disadvantage is a lack of tunability. In practice, the wafers are grown with a radial thickness gradient from the center to the perimeter, which allows for tuning the cavity length and thereby the resonance wavelength λ_q by selecting the radial position on the wafer.

Such a structure is displayed in Fig. 2.3(a), outlining the refractive index contrast of the DBR layers in black. The red curve (right y -axis) shows the modulus squared of the electric field. In the center, the electric field is maximum. The penetration of the field into several layers of the mirrors is also visible, which sets the effective cavity length L_{eff} , the relevant quantity replacing L when calculating the mode volume of the resonator. A photon is stored for a time τ_{cav} in the cavity that increases with the reflectivity of the enclosing mirrors. The mirror reflectivity \mathcal{R} scales with the number of

$\lambda/4$ -pairs $2N$ as

$$\mathcal{R} = 1 - 4 \frac{n_r}{n_l} \left(\frac{n_2}{n_1} \right)^{2N}, \quad (2.4)$$

with $n_{r,l}$ the surrounding refractive indices on the right and left sides, $n_1 > n_2$ the indices of the alternating $\lambda/4$ layers. The quality factor of the cavity $Q = \omega\tau_{\text{cav}} = \omega/\gamma_{\text{cav}}$ relates the mirror quality to the storage time τ_{cav} or loss rate γ_{cav} for a given frequency ω . It is approximately given by [8]

$$Q = \frac{\pi(\mathcal{R}_1\mathcal{R}_2)^{1/4}}{1 - (\mathcal{R}_1\mathcal{R}_2)^{1/2}}, \quad (2.5)$$

in terms of the front and back mirror reflectivities $\mathcal{R}_{1,2}$.

While the momentum is restricted in the z -direction, the photons are free to travel in the xy -plane. The cavity dispersion relation [8] reads

$$E_{\text{cav}} = \frac{\hbar c}{n_{\text{cav}}} \sqrt{k_{\perp}^2 + k_{\parallel}^2} \approx E_{\text{cav}}(k_{\parallel} = 0) + \frac{\hbar^2 k_{\parallel}^2}{2m_{\text{cav}}} \quad (2.6)$$

with the effective photon mass in the cavity $m_{\text{cav}} = E_{\text{cav}}n_{\text{cav}}^2/c^2$. The structure is translationally invariant in the xy -plane and therefore the in-plane momentum is conserved for light entering and exiting the cavity structure. This leads to a one-to-one correspondence of in-plane momentum inside the cavity to angle of incidence θ viewed from outside. For small $k_{\parallel} \ll k_{\perp}$ [8]

$$k_{\parallel} \approx \frac{2\pi}{\lambda} \theta, \quad (2.7)$$

which is very convenient for experimental purposes: By exciting and detecting at specific angles θ , the dispersion relation can be mapped out directly. Figure 2.3(b) shows the cavity reflection signal (reflected intensity for s -polarization) as a function of energy $E = \hbar\omega$ for $\theta = 0, 10, 20, 30^\circ$ from red to yellow. As expected, the energy where incoming photons are resonant with the cavity mode increases with the angle of incidence.

Photons take many round-trips before leaving the cavity, which is equivalent to observing an electric field enhancement in the center of the cavity. The enhanced electric field amplitude allows boosting light-matter interactions if an optically active material is placed close to the maximal field E_{max} .

2. Cavity QED with Exciton-Polaritons and a 2D Electron System

We consider a two-dimensional quantum well and how its excitons couple to the optical microcavity. Due to momentum conservation, the interaction will be of the form [8]

$$H_{\text{int}} = \hbar\Omega_R \left(\hat{a}_{\vec{k}_{\parallel}}^{\dagger} \hat{x}_{\vec{k}_{\parallel}} + \hat{a}_{\vec{k}_{\parallel}} \hat{x}_{\vec{k}_{\parallel}}^{\dagger} \right) \quad (2.8)$$

for a cavity photon in a particular longitudinal mode $\hat{a}_{\vec{k}_{\parallel}}$ and the light-matter interaction strength Ω_R (Rabi coupling), assumed to be independent of k_{\parallel} . This coupling rate depends on the oscillator strength of the underlying optical transition and is enhanced by the microcavity [9]

$$\Omega_R = \left(\frac{4\pi\omega}{L_{\text{eff}}} f_x \right)^{1/2} \frac{E(z)}{E_{\text{max}}}, \quad (2.9)$$

with $E(z)$ the electric field at the position z of the quantum well. If this coupling rate exceeds the dissipation rate of the cavity γ_c and non-radiative decay rate of excitons γ_x , the system enters the strong-coupling regime and the interaction term Eq. (2.8) hybridizes the exciton and photon modes into new eigenmodes \hat{p} , \hat{q}

$$\begin{pmatrix} \hat{p}_{k_{\parallel}} \\ \hat{q}_{k_{\parallel}} \end{pmatrix} = \begin{pmatrix} -C(k_{\parallel}) & X(k_{\parallel}) \\ X(k_{\parallel}) & C(k_{\parallel}) \end{pmatrix} \begin{pmatrix} \hat{a}_{k_{\parallel}} \\ \hat{x}_{k_{\parallel}} \end{pmatrix} \quad (2.10)$$

called polaritons² [46]. The coefficients $X, C \in \mathbb{C}$ quantify the composition in terms of the bare exciton and cavity fields. The corresponding eigenenergies for the upper (\hat{q}) and lower (\hat{p}) polaritons are given by

$$E_{\text{UP,LP}}(k_{\parallel}) = \frac{1}{2} \left(E_x + E_{\text{cav}}(k_{\parallel}) \pm \sqrt{4\Omega_R^2 + (E_x - E_{\text{cav}}(k_{\parallel}))^2} \right). \quad (2.11)$$

For a given Ω_R , this energy depends on the detuning $\Delta = E_{\text{cav}} - E_x$. This dependence is plotted in Fig. 2.4(a). The dashed lines mark the energies E_x (red) and E_{cav} (green), the uncoupled eigenstates. Full lines mark the polariton energies, the new eigenmodes. The exciton and cavity contents $|X|^2$ and $|C|^2$ can be tuned between zero and one by varying Δ , with both polariton branches representing a 50:50 mixture at resonance $\Delta = 0$. The

²We abbreviate \vec{k}_{\parallel} by k_{\parallel} and assume an isotropic dispersion in x, y .

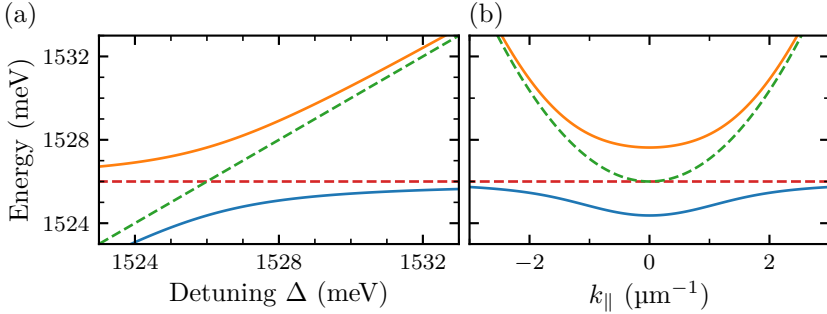


Figure 2.4: Polariton anticrossing and energy-momentum dispersion relation. (a) Anticrossing between exciton (red dashed) and cavity (green dashed) resonances, as the cavity energy is tuned $\Delta = E_{\text{cav}} - E_X$. The modes hybridize and form lower (blue) and upper (orange) polariton modes. (b) Polariton energy-momentum dispersion relation for fixed $\Delta = 0$, stemming from the parabolic dispersion of the cavity mode (green dashed).

dependence of the eigenenergies on in-plane momentum can be obtained by inserting the exciton and cavity dispersions. The resulting in-plane energy-momentum relation of polaritons is plotted in Fig. 2.4(b). Here, a parabolic cavity dispersion Eq. (2.6) was inserted (green dashed line) and the exciton energy is assumed constant (red dashed line), which is a good approximation due to $m_x \gg m_{\text{cav}}$. Again, the lower and upper polariton eigenmodes are drawn as full lines. The in-plane momentum conservation and correspondence to optical angle of incidence remains valid, which renders the polariton dispersion relation experimentally accessible by angle resolved spectroscopy.

Polaritons inherit properties from both their components. Through cavity decay γ_{cav} , polaritons decay into photons at a rate proportional to the cavity content $|C|^2$, but at a photon energy corresponding to Eq. (2.11). Through the exciton content $|X|^2$, the polaritons inherit a finite amount of interactions. Electron or hole exchange leads to interactions between excitons given by $U_x = 6e^2 a_B / \epsilon$ in the Born approximation [9, 47, 48], which results in a Kerr-type nonlinearity for polaritons $U_p = |X|^4 U_x$. These interactions are responsible for bi-stability, superfluidity and Bose-Einstein condensation, and in most cases, can be described by a mean-field description [8, 9].

2.2 Introduction to 2D Electron Systems

2.2.1 Doped Semiconductor Heterostructures

In its intrinsic form, the electrical properties of GaAs are poor, the conductivity being low. To introduce additional carriers, a small amount of impurities can be introduced to the host crystal. By providing bound electrons (holes) slightly below the conduction band (above the valence band), additional carriers can contribute to transport after thermal excitation. At large enough doping densities, an impurity band can form that conducts electricity even at $T = 0$. However, incorporating impurities comes with the undesired side effect of strong scattering of the charge carriers on the ionized donor (acceptor) sites left behind [49]. This can be avoided in heterostructures where the dopants are spatially separated from the conducting quantum well of interest (modulation or remote doping). The energy structure in the z -direction can be engineered such that the conduction band in the QW is below the Fermi energy at equilibrium, i.e. electrons are populating the QW. As impurities, Silicon (Si) replacing a Ga atom is often used for electron (n -type) doping and Carbon (C) replacing an As atom for hole (p -type) doping. Populating a quantum well with electrons (or holes) creates a two-dimensional electron (hole) gas. The density of states in two dimensions for a parabolic band dispersion is constant (spin degeneracy g_s)

$$D(E) = \frac{g_s m^*}{2\pi\hbar^2}, \quad (2.12)$$

and the states are occupied up to the Fermi energy E_F . It is related to the sheet density of electrons per area $n_e = D \cdot E_F$ and defines the Fermi momentum k_F via $E_F = \hbar^2 k_F^2 / (2m^*)$.

To probe electrical transport through the 2DEG as well as to thermally anchor it, electrical contacts are established to outside reservoirs. Thermal anchoring is necessary to experimentally control the electron temperature, especially at low temperatures close to 0 K where heat transport occurs mostly via electron scattering. Depositing a metal electrode on the surface of a semiconductor creates a Schottky barrier. Most metals form a barrier on GaAs such that the Fermi energy in the metal is about 0.8 eV above the conduction band in GaAs [40]. A depletion region forms in the vicinity of

the interface and applying an additional voltage to the metal gate can be used to control the charge carrier density in the QW via the field effect. The transport characteristics of a Schottky barrier are diode-like. For electrical transport measurements of a 2DEG, it is usually more desirable to have linear current-voltage relation, or ohmic contacts. The Schottky barrier can be avoided by annealing an eutectic mixture (often based on germanium and gold) to form an alloy with ohmic behavior between the surface electrode and the 2DEG. Indium can also be used for annealing and to create ohmic contacts to the 2DEG.

The simplest description of electric transport in response to an electric field \vec{E} is through Ohm's law for the current density $\vec{j} = \sigma \vec{E}$. In terms of resistivity $\rho = \sigma^{-1}$, the matrix inverse of the conductivity, it reads

$$\begin{pmatrix} E_x \\ E_y \end{pmatrix} = \begin{pmatrix} \rho_{xx} & \rho_{xy} \\ -\rho_{xy} & \rho_{xx} \end{pmatrix} \cdot \begin{pmatrix} j_x \\ j_y \end{pmatrix}. \quad (2.13)$$

By performing a magneto-transport experiment with magnetic field in z -direction in a Hall bar or van der Pauw device geometry, ρ_{xx} and ρ_{xy} can be independently measured. In this scenario, a current is sourced in the longitudinal (x) direction and the contact voltages are read out to infer the electric fields E_x, E_y . This turns out to be a very useful tool to characterize the 2DEG, through [40]

$$\rho_{xx} = \frac{m^*}{n_e e^2 \tau} \quad (2.14)$$

$$\rho_{xy} = \frac{B}{|e| n_e}, \quad (2.15)$$

both the sheet density n_e and the scattering time τ can be extracted. The scattering time is related to the mobility $\mu = |e| \tau / m^*$. In the Drude model of diffusive transport, the electron drift velocity is $v_x = \mu E_x$ ($B = 0$).

2.2.2 Integer and Fractional Quantum Hall Effects

In the last section, we found the classical Hall resistance ρ_{xy} to increase linearly with B . In clean samples, at low temperatures and in external fields in the range of Tesla, a more intricate dependence of ρ_{xy} and ρ_{xx} was ob-

2. Cavity QED with Exciton-Polaritons and a 2D Electron System

served. The integer quantum Hall effect (IQHE) [50] and fractional quantum Hall effect (FQHE) [51] are characterized by a quantized Hall resistance ρ_{xy} and zeros in the longitudinal resistance ρ_{xx} . An example of such a quantum transport measurement is reprinted in Fig. 2.5(a), illustrating both these features in the resistivities ρ_{xx} , ρ_{xy} occurring at particular magnetic fields (x -axis).

In a magnetic field, parabolic energy bands of charged particles are quantized into Landau levels (LLs) $E_n = \hbar\omega_c(n + 1/2)$ which are degenerate states with the spectrum of a harmonic oscillator. Their energy separation is given by the cyclotron frequency $\omega_c = \frac{eB}{m^*}$ and the degeneracy of each level is $n_B = \frac{B}{h/e} = \frac{1}{2\pi l_B^2}$, given by the density of magnetic flux quanta threading the sample surface [34]. The characteristic length scale $l_B = \sqrt{\hbar/eB}$ is called the magnetic length. By normalizing the electron density n_e by the flux density, the filling factor

$$\nu = \frac{n_e}{n_B} = \frac{\hbar n_e}{eB} \quad (2.16)$$

is obtained. Its integer part counts the number of completely filled Landau levels. The IQHE occurs at integer values of ν , while the FQHE is visible at particular rational fractions $\nu = p/q$. To account for different subbands that form LLs, we add an energy offset E_0 and a Zeeman term accounting for the electron spin projection s along the magnetic field

$$E_n = E_0 + \left(n + \frac{1}{2}\right) \hbar\omega_c + g\mu_B s B \quad (2.17)$$

to the Landau level dispersion (g : g-factor of the electron, μ_B : Bohr magneton).

Considering disorder and confinement at the edge of the sample provides a picture to qualitatively understand the IQHE. A schematic, disregarding the Zeeman splitting, is shown in Fig. 2.5(b). Landau levels have a finite width in energy (shaded in gray) due to various broadening mechanisms, for example the random electrostatic potential by the donor impurities in the doping layers. Raising the magnetic field from zero starts to separate the overlapping LLs in energy. Longitudinal conductance oscillations are obtained as the Fermi energy (at fixed electron density) crosses the discrete LL spectrum when the magnetic field is tuned (Shubnikov–De Haas effect).

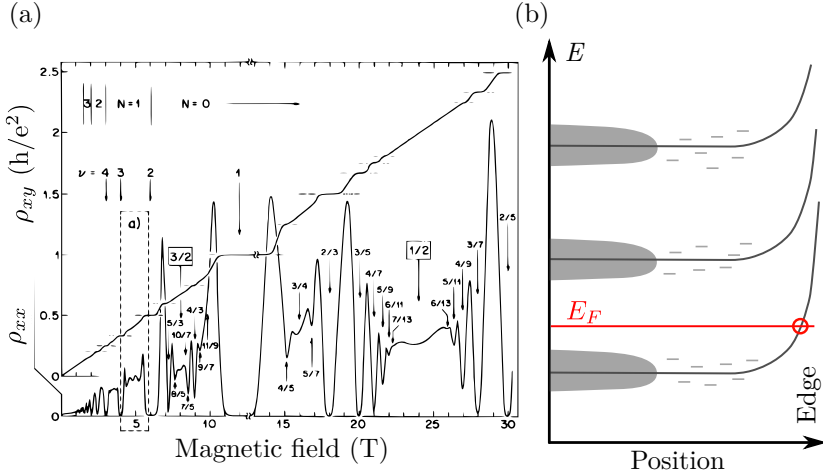


Figure 2.5: Integer and fractional quantum Hall effects. (a) Magneto-transport experiment showing the evolution of the longitudinal ρ_{xx} and transverse resistance ρ_{xy} . Figure from [54]. (b) Schematic of Landau level broadening due to disorder and increase in energy at the sample edge. States in the bulk are localized by disorder, while the edge confinement ensures that the Fermi energy E_F crosses $[\nu]$ edge states.

When the cyclotron energy exceeds the LL broadening, the Fermi energy may be situated in an energy gap, as drawn in Fig. 2.5(b). The combination of magnetic field and disorder leads to localization of carriers in the bulk, preventing them from contributing to electronic transport. The electrons become incompressible, there is no phase space available to move without traversing the energy gap. However, the confinement by the system boundary ensures that each LL below the Fermi energy in the bulk will cross the Fermi energy E_F (red line) towards the sample edge. It turns out that each edge states contributes one conductance quantum h/e^2 [52]. To understand the fractional quantum Hall plateaus, it is necessary to consider Coulomb interactions between electrons. The transport signatures of the IQHE repeat themselves at rational fractions of ν , suggesting the formation of new energy gaps induced by electron-electron interactions. Many electrons correlate their motion and form quasiparticles with fractional charge [53].

For reference regarding the different energy scales, we quote approximate numerical values for GaAs based systems as a function of magnetic field in Tesla. The cyclotron energy $\hbar\omega_c = 1.7 \times B \text{ meV T}^{-1}$ (20 K T^{-1}) turns out to be very large compared to the Zeeman energy $E_Z = 25 \times B \text{ } \mu\text{eV T}^{-1}$ (0.3 K T^{-1}). An energy scale relevant for interactions is the Coulomb energy $E_C = \frac{e^2}{4\pi\epsilon_0\epsilon l_B} \approx 4.3 \text{ meV}/\sqrt{\text{T}}$.

2.2.3 Trions and Exciton-Polarons

Having introduced the basic properties of 2D electron systems, we would like to discuss their optical properties, at energies below the band gap. A natural starting point is to consider how excitons could be modified in the presence of an additional electron, leading to the trion picture; or in the presence of a Fermi sea of electrons, which will lead to the polaron picture. Bound complexes of charges with an exciton were first suggested by Lampert [55] but only later observed in experiments [56–58]. This was enabled by the enhanced binding energies of these complexes in quantum well structures as compared to bulk crystals [59]. These complexes can only be observed at temperatures below their binding energy, and for rather low electron densities before screening takes over and the complexes are ionized. At zero magnetic field, only the singlet trion configuration is bound [59, 60]. Even at high electron densities, interaction effects still play a role [61] and the transition from trion complexes at low densities to the Fermi edge singularity at high densities was studied [62].

Pioneering studies reported the modifications to polariton resonances when a 2DEG is embedded in a microcavity [63–65]. A linear relationship was found between the electron (hole) density and the oscillator strength of the trion-like resonance by measuring the normal mode splitting $\Omega_R^2 \propto f$. In the context of polariton thermalization and Bose-Einstein condensation [8], interactions between polaritons and electrons have been proposed and analyzed as a mechanism for polariton thermalization [66–69]. Also the limit of high carrier densities has been studied both experimentally [70] and theoretically [71].

More recently, there has been renewed interest in the nature of optical excitations of intermediate density electron gases [21, 72, 73]. Instead of starting with an exciton and analyzing molecular complexes with charges, a

many-body perspective can be taken, treating the exciton as an impurity in a Fermi sea (Fermi polaron). These developments have been spurred by a confluence of experiments with ultracold atomic gases, where atomic impurities are studied, immersed in a Bose-Einstein condensate [74–76] or Fermi gas of atoms [77]. In the solid state context, these excitations may be described by dispersive interactions between the polarizable excitonic component of the polariton and charge-density fluctuations of the Fermi sea [78–80]. Recently, it has been demonstrated in transition metal dichalcogenide monolayers that an accurate description of optical excitations in the presence of a degenerate electron gas is provided by the concept of Fermi polarons [20, 81–83]. These polaronic states consist of an exciton dressed by collective trion-hole excitations of the Fermi sea, where the spin of the photo-excited electron is opposite to that of the dressing Fermi sea electrons [21, 72, 84].

At the time of this writing, the discussion how to contrast and reconcile the trion and polaron based pictures and more detailed calculations as to their properties is progressing rapidly [85–88]. We chose to present our work from the polaron perspective and use its nomenclature to label our resonances. We refer to trions as excitons bound to localized electrons, excitations that could be observable, akin to emission from excitons localized by donor/acceptor sites [89, 90]. However, they should have vanishing oscillator strength in a two-dimensional system—at odds with resonant absorption experiments and observed strong light-matter coupling [21]. However, we want to clarify that, as the theoretically more refined collective trion-hole and polaron models are explored, it appears that the two points of view converge, yielding identical results for many experimental signatures [91], except for an energy shift between polaron and trion [88]. Hence, we do not claim that our experiments can rule out one of the two perspectives at this stage. We further remark that the polaron description applies well to excitons in TMD materials due to the large exciton binding energy and symmetry between electron and hole masses. In GaAs, a simple description based on the so-called Chevy Ansatz [92] is rendered more difficult due to the large heavy hole mass compared to the lighter conduction band electrons. However, we expect this restriction to be lifted in the presence of an external magnetic field, the case considered in Chapter 3.

We turn to experiments and show exemplary spectroscopic data of optical resonances in a quantum well subjected to a 2D sheet of charge carriers in

2. Cavity QED with Exciton-Polaritons and a 2D Electron System

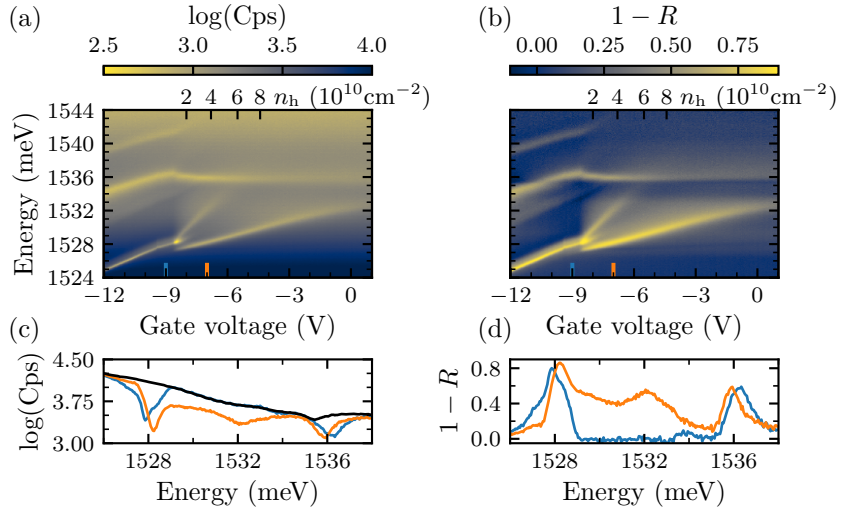


Figure 2.6: Spectroscopy of a 2D hole gas as a function of density n_h , including the depleted case $n_h = 0$ of an empty QW. (a) Raw WL reflection counts per second (Cps) in logarithmic scale. (b) Reference spectrum subtracted to obtain absolute reflectivity, linear scale. Dark blue, $R = 1$, is where all light is reflected. Yellow color is assigned to $0 < R < 1$, where the sample absorbs light. (c) Line-cuts into (a) at $V_g = -9 \text{V}$ (blue) and -7V (orange) and the reconstructed background spectrum (black). (d) The same line-cuts for the normalized reflectivity (b).

Fig. 2.6. Focusing on Fig. 2.6(a), unprocessed reflection spectra are shown along the y -axis for a 2D hole gas³ where the hole density is controlled by the gate voltage V_g . The hole density is zero on the left-hand side, becomes finite above -9 V and is increasing towards the right-hand side. Starting out with a depleted quantum well, we expect excitonic resonances. Three resonances are visible, which we attribute to the heavy hole exciton (1524 meV), light hole exciton (1534 meV) and $2s$ heavy hole exciton (1540 meV). In the range from $V_g = -12$ V to -9 V, the gate voltage controls the electric field in z -direction. The energies of the resonances shift due to the Stark effect. Following the resonances to finite hole density, they split into the lower energy attractive and higher energy repulsive polarons. The attractive polaron resonance appears at an energy below the exciton, separated by the trion binding energy. The repulsive light hole branch is almost invisible, presumably due to vanishingly small binding energy of the associated trion. Line-cuts for the cases of excitons (blue) and attractive and repulsive polarons (orange) are shown in Fig. 2.6(c), corresponding to $V_g = -9$ V and $V_g = -7$ V, respectively. It is interesting to note the strikingly different energy scaling of the light hole resonance as compared the the heavy hole resonance. As n_h becomes finite, the Fermi energy resides inside the heavy hole valence band but not in the light hole band, i.e. all charge carriers are heavy holes. As they fill up available states in the heavy hole band, the optical absorption is pushed towards higher and higher energy. This effect is absent for the light hole transition, and the resonance even red-shifts further with density due to increased attraction to the higher density hole gas. The other panels Figs. 2.6(b) and 2.6(d) serve to illustrate the background subtraction procedure explained later in Section 2.3.2. They contain the same data but normalized with the reconstructed reference spectrum of the light source (black line in Fig. 2.6(c)).

³Electron and hole gases behave qualitatively similar. Holes having a larger effective mass, they tend to localize faster and display lower transport mobilities, i.e. shorter timescales between scattering events.

2.3 Experimental Methods

2.3.1 Cryogenic Systems

Many energy scales of interest in our experiments are lower than the thermal energy $k_B T$ at ambient temperatures. In particular, this applies to the exciton and trion binding energies, where increased temperatures lead to a broadening of the optical transitions as the kinetic energy of electrons and holes is increased. Scattering mechanisms via phonons and electrons are also greatly suppressed at low temperatures. Most stringently, some fractional quantum Hall states have small energy gaps governed by Coulomb interactions corresponding to millikelvin temperatures. For those reasons, we performed our experiments below $T = 100$ mK. Liquid nitrogen and liquid Helium-4 can be used to achieve bath temperatures of 77 K and 4.2 K. Alternatively, a pulse tube refrigerator can provide cooling power down to the single Kelvin range. Sub-Kelvin temperatures can be reached by using dilution refrigerators, where a liquid Helium-3 and Helium-4 mixture is kept in conditions where it separates in two phases: a ^3He -rich phase and a ^3He -poor phase. The cooling power stems from separating ^3He from the rich into the dilute phase. This process is continuously repeated by extracting ^3He from the dilute phase and circulating it back into the mixing chamber.

We used two experimental setups depicted schematically in Fig. 2.7. A dilution refrigerator⁴ that inserts into a liquid ^4He bath which is accessible for optical experiments via a single-mode optical fiber. The bath cryostat is equipped with a superconducting solenoid magnet⁵ that allows applying magnetic fields up to 16 T. The sample is mounted in a fixed copper holder, while the confocal objective and fiber tip can be translated in all three dimensions. This allows to chose the x, y position on the sample as well as to move the focal point of the objective with respect to the sample in the z -direction. The electron temperature achieved in the sample tends to be above the base temperature of the dilution refrigerator. To establish an estimate for the electron temperature, we track the evolution of the optical signature of a fragile quantum Hall state ($\nu = 2/5$, detailed later in Chapter 3) while warming up the cryostat. In Fig. 2.8, the time evolution of

⁴Leiden Cryogenics MCK 76-400, Attocube ULT-CFM.

⁵Cryogenic Ltd. low-loss liquid helium system with 16 T superconducting magnet.

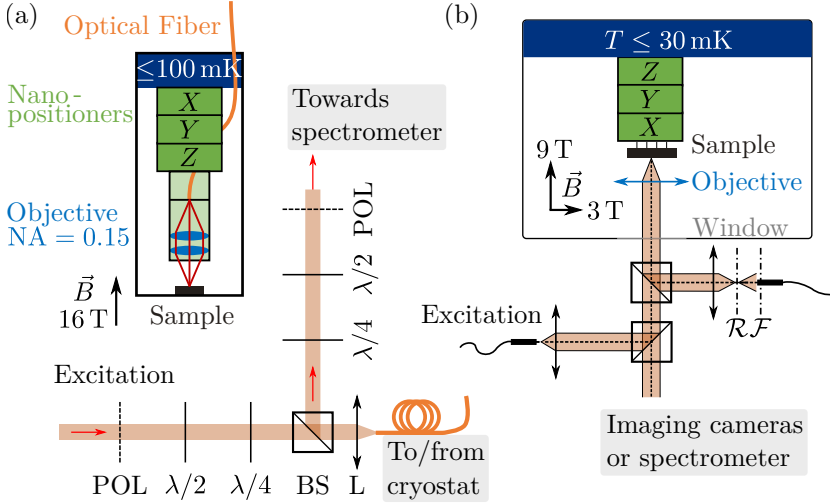


Figure 2.7: Cryogenic optical setups. (a) Fiber-based confocal microscope for optical measurements. Reflected photons are separated from incident light on a beam splitter (BS) and analyzed in a spectrometer. Excitation and detection arms are equipped with quarter ($\lambda/4$) and half ($\lambda/2$) waveplates and polarizers (POL) for polarization-resolved spectroscopy. (b) Free-space optical access through a thermal radiation blocking window port. This configuration allows for more freedom in the design of optical experiments. In particular, it enables angle resolved spectroscopy.

the spectrum is plotted, with the energy of photons along the y -axis. Two resonances are visible as dark blue minima on a brighter background, their energy separation is a measure of the electron spin configuration. Following the energy splitting between the two resonances, first signs of an increase appear at 100 mK (1000 s). Later after 1600 s, this energy splitting drastically increases at about 200 mK. The temperature readings are taken from a calibrated resistive ruthenium oxide probe that is mounted in the copper block that holds the sample. This measurement establishes an upper bound on the sample temperature of 100 mK.

The second setup (depicted in Fig. 2.7(b)) is based on a pulse tube and dilution refrigerator system⁶ with a 9-3 T vector magnet. Its base temperature

⁶BlueFors LD250 with American Magnetics Inc. 9 T + 3 T vector magnet.

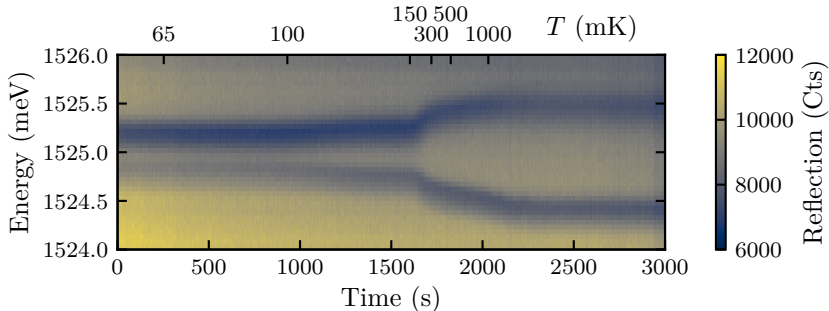


Figure 2.8: Electron temperature estimation. Tracking the optical signature of the $\nu = 2/5$ state during the warm-up procedure of the cryostat in the fiber-based setup. First changes appear after 100 mK, drastic changes follow above 150 mK. Cts, counts.

is about 20 mK. The sample is optically accessible via windows through the thermal stages of the cryostat, which allows for more sophisticated optical setups. The main disadvantage is an increased susceptibility to mechanical vibrations compared to the compact fiber based setup. Vibrations are induced by the pulse tube and the pumps used to circulate the ^3He mixture and transferred to the optical setup. Here, the sample is mounted on *xyz*-positioners⁷ that allow translations with respect to the objective lens, which is fixed in place.

It is interesting to note that the energy of individual photons we will use as a probe is orders of magnitudes higher than $k_B T$ for all sample temperatures T . If all this energy was dissipated to the sample and its electrons, this would severely limit the applicability of optical spectroscopy at cryogenic temperatures. However, this type of energy dissipation need not occur, as long as the photons are re-emitted with the same energy. This is why we will most often resort to resonant optical spectroscopy experiments. Nevertheless, the incident photon flux is kept low such that the incident power is on the order of pW to nW, way below the cooling power of the dilution units in the μW range. In our experiments, heating of the sample is generally not an issue. Undesired changes to the charge environment through background absorption of photons by defect sites appear before heating effects become

⁷Attocube ANPx101/RES, ANPz102/RES.

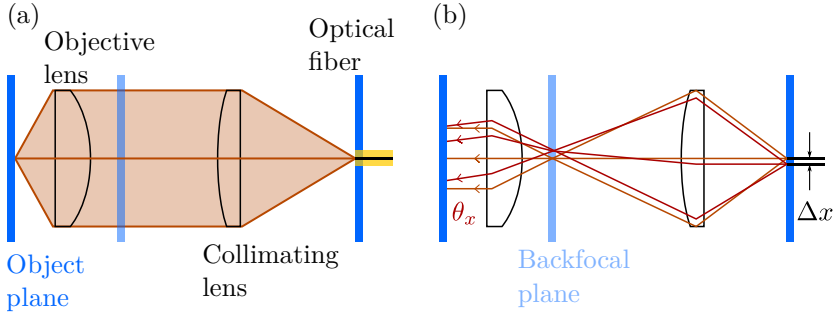


Figure 2.9: (a) Confocal configuration, with the core of an optical fiber acting as pinhole for spatial resolution. (b) Focusing the light emitted from an optical fiber to the back focal plane of the objective allows to excite with well-defined angle of incidence. Displacing the fiber Δx varies the angle of incidence θ_x .

prominent, which will be evidenced in Chapter 3.

2.3.2 Optical Measurement Setup

We give a general introduction to the optical experimental setups we used. This covers linear optical spectroscopy used throughout the thesis and in particular in Chapter 3. Specialized extensions are given later before the relevant experiments in Chapters 4 and 5. Our experiments were performed in reflection geometry with confocal microscopes. The setups can be divided into three parts. One constitutes the cold part inside the cryostat including the sample. The other two are dedicated to the excitation, sending light to the sample, and detection, to analyze light reflected or emitted from the sample.

In the first cryogenic system Fig. 2.7(a), light is delivered by an optical fiber glued into a ceramic ferrule and rigidly mounted in a lens holder. Therein is a pair of single aspheric lenses, NA-matched to the fiber. The first collimates the fiber output, the second acts as objective lens focusing the light to a spot on the sample. This arrangement realizes a confocal geometry, schematically shown in Fig. 2.9(a). The fiber core acts as a pinhole for spatial filtering. The single-mode optical fiber is coupled out to a free-space setup on a nearby optical table. It consists of a beam splitter (BS) that allows to both send

2. Cavity QED with Exciton-Polaritons and a 2D Electron System

and detect light through the fiber port, and optics to control the polarization of the beam.

An experimental challenge in the case of fiber-based access is polarization control. The polarization of light changes uncontrollably while propagating through the fiber which acts like a combination of unknown waveplates. Its properties depend sensitively on the geometry of the fiber path, strain and fluctuations therein and the temperature. A linear input polarization is typically converted into an arbitrary elliptical polarization once it arrives at the sample. Furthermore, the polarization is changed as a function of an applied magnetic field. This occurs due to the Faraday effect in the fiber and cold lenses, as well as residual mechanical movement induced by magnetic components inside the cryostat (which are avoided as much as possible). We went around this challenge by using the circular selection rules of our sample in a magnetic field and used the signal from the sample to select the polarization. The polarization optics was adjusted iteratively to maximize signal strength or signal contrast for a selected resonance. This effectively compensates the action of the fiber to realize circular polarization at the sample.

For resonant reflectivity measurements, we were using an attenuated superluminescent light emitting diode⁸ as a broadband source, with center wavelength equal to 822.4 nm and a 3 dB bandwidth of 25 nm. This excitation source is later referred to as white light (WL) source. For non-resonant, above band gap excitation a Helium-Neon laser⁹ at $\lambda = 632$ nm was used. At this wavelength, the top DBR does not act as mirror anymore. This allows for the non-resonant injection of electron-hole pairs. A wavelength-tunable, continuous wave (CW) external cavity diode laser¹⁰ was used for resonant spectroscopy.

On the detection side, a spectrometer¹¹ and CCD camera¹² was used to disperse the signal light spectrally and record the intensity as a function of wavelength. To obtain the reflectivity spectrum in the case of WL excitation, the background from the source has to be accounted for. This can be a diffi-

⁸Exalos EXS210036-01.

⁹Melles Griot 05-SRP-812.

¹⁰Sacher TEC500.

¹¹Princeton Instruments Acton SP2500.

¹²Roper Scientific back-illuminated liquid N₂ cooled CCD.

cult problem in general if there is no straightforward experiment available to measure the spectral shape of the source. In most cases, a two-dimensional data set could be used to reconstruct the reference spectrum quite accurately: If the signal from the sample varies in response to a tuning parameter (gate voltage, position on the sample, magnetic field), the constant reference spectrum can be reconstructed by stitching together spectral regions where the sample acts as a mirror. For this purpose, we treated each wavelength (pixel on the CCD camera) individually and estimated the background spectrum by taking the maximum values across the tuning parameter. We obtain the reflectivity spectrum $R(E) = s(E)/b(E)$ by normalizing the measured spectrum $s(E)$ by the reference spectrum $b(E)$ of our white light source. This only works if the sample has an absorptive line shape, in case interference effects lead to dispersive line shapes, taking the maximum value does not suffice. In this case, and when no external tuning parameters enabled two-dimensional data sets, we were using the fact that the spectral shape of the WL is Gaussian and smooth compared with the narrow, peaked resonances in our samples. We resorted to a low order polynomial fit to the background in spectral windows where there are no visible optical resonances to obtain an estimate of $b(E)$.

The second cryogenic system Fig. 2.7(b) allows for separate configurations of the excitation and detection paths as well as free space imaging. A single cold aspheric lens is placed by its focal distance from the sample surface. This allows for a confocal configuration as before but the field of view of this lens can be imaged onto a camera¹³. Furthermore, the back focal plane of the objective lens (see configuration sketched in Fig. 2.9(b)) can be imaged onto a camera to obtain the Fourier space representation. Again an optical fiber tip was used as a pinhole but here to filter spatial frequencies, allowing for collecting light at different emission angles. Finally, this arrangement can be used in the reversed direction to inject light at particular spatial frequencies. This creates polaritons with well defined in-plane momentum, if the laser energy matches the polariton dispersion relation. A wave packet is launched and propagates with a group velocity $v_g = \partial\omega_{LP}/\partial k_{\parallel}$. This arrangement works like a $4f$ optical setup, however our system was not fully conjugated due to the large distance between the sample and the cryostat window. The

¹³FLIR CM3-U3-13S2M-CS.

distance between the back focal plane of the cold objective and the next lens (relay lens) is larger than the focal length of the relay lens.

In principle, transmission experiments in addition to reflection are highly desirable because the microcavity also acts as a filter. Only light accepted into the cavity mode is transmitted, rejecting any remaining excitation light. Implementing this would be possible in the future but requires two modifications. First, the sample has to be optically transparent—currently the thick GaAs substrate absorbs light in the wavelength range of interest preventing transmission. This could be achieved by performing epitaxial lift-off where the microcavity is removed from the substrate and bonded to another transparent substrate. Second, another optical port has to be build into the cryogenic setups to access the transmission signal, including the necessary degrees of freedom to align both the reflected and transmitted beams.

2.4 Sample Design and Characterization

Our samples were grown by molecular beam epitaxy (MBE) on (001) GaAs substrates. MBE growth for all projects of this thesis was performed by Dr. Stefan Fält in the group of Prof. Werner Wegscheider at ETH Zurich. The measurements in the following chapters refer to the sample structures summarized in Fig. 2.10. The material compositions of the structures is drawn schematically, MBE growth is starting from buffer layer on top of the substrate. The labels A, B, B*, and C refer to entire wafers grown in one run each. Apart from the substrate and grown buffer layer, which are larger than depicted, the layer thicknesses are drawn to scale in the growth direction (upwards). Due to the geometry of the MBE source cells and the substrate rotation during growth, the wafers are thickest in the center and become (parabolically) thinner towards the edge. For all experiments, chips sized around $5 \times 5 \text{ mm}^2$ were cleaved from the wafers for further processing. They were taken at the radial position where the cavity thickness is such that the polaron resonances anticross within the area of the chip. The labels of the individual chips were omitted throughout this thesis as we found no indication of differences between their properties relevant for our experiments. The electrical properties of the samples were characterized at the temperature $T = 1.6 \text{ K}$ by performing magneto-transport measurements of

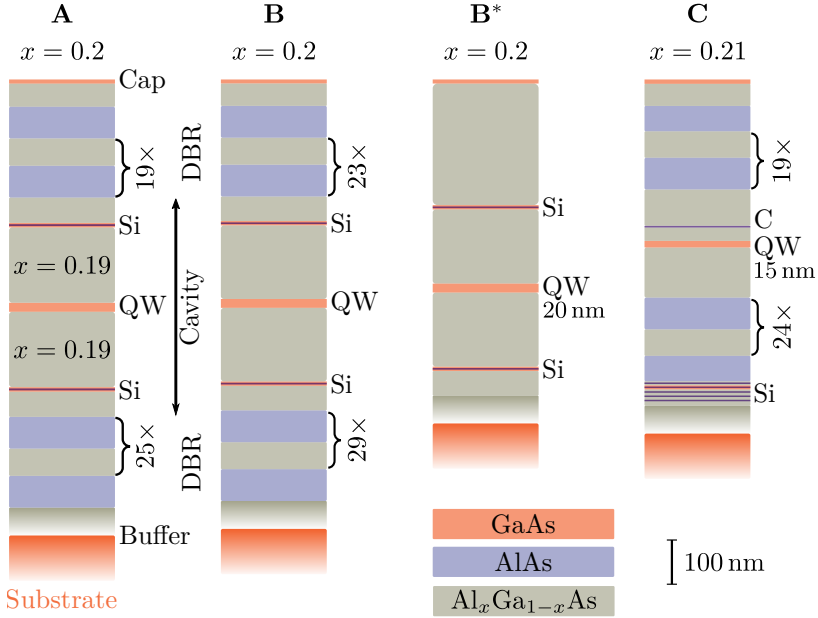


Figure 2.10: Sample heterostructures A, B, B* and C along the growth, z -direction upwards. Samples A and B feature a 2DEG embedded in an optical microcavity. Sample B* is structurally similar to B, but grown without optical cavity. Sample C contains a 2DHG and a Silicon back gate to control the hole density. Buffer and substrate layers not drawn to scale.

the longitudinal and transverse resistivities. Indium contacts in van der Pauw geometry were used in this characterization. In this geometry, contacts are placed along the circumference of a rectangular chip without further processing. Otherwise the necessary sample processing steps have been performed in a cleanroom environment¹⁴.

2.4.1 Sample A – Low Density 2DEG

The structure A consists of a 2DES in a 20 nm modulation doped GaAs QW. The QW is embedded at the center of a length 2λ microcavity made

¹⁴FIRST Center for Micro- and Nanoscience at ETH Zurich.

2. Cavity QED with Exciton-Polaritons and a 2D Electron System

from $\text{Al}_{0.19}\text{Ga}_{0.81}\text{As}$. It is placed at the antinode of the electric field. The front (top surface, higher z -position) distributed Bragg reflector (DBR) is composed of 19 pairs of AlAs / $\text{Al}_{0.20}\text{Ga}_{0.80}\text{As}$ layers plus one additional pair including the GaAs capping layer at the surface. There are 25.5 DBR pairs on the back side. This imbalance in the number of pairs is chosen to compensate the refractive index mismatch between vacuum above the top surface and buffer/substrate below the bottom DBR. The measured quality factor of the microcavity is $Q \simeq (5.5 \pm 0.1) \times 10^3$. The QW features a double-sided silicon δ -doping with a set-back distance of $3\lambda/4$ ($\simeq 184$ nm) above and below the center of the cavity.

Earlier studies on the optics of 2DES have shown extreme sensitivity of the electron density n_e to optical power [19, 93–95]. Increasing the optical power not only changes n_e , but also causes qualitative changes in the reflectivity spectrum [96], which is detrimental to the study of fragile QH states. The light-sensitivity of n_e is attributed to photo-excitation of DX centers in Si-doped $\text{Al}_x\text{Ga}_{1-x}\text{As}$ with $x > 0.2$ [40, 97]. To minimize the photoexcitation of DX centers, we keep a low Aluminium content $x \leq 0.2$ in the material surrounding the doping regions: we place the dopants in GaAs doping quantum wells (DQW) and we use $\text{Al}_{0.19}\text{Ga}_{0.81}\text{As}$ in the rest of the cavity spacer. We further protect the dopants by placing the DQWs in nodes of the electric field inside the cavity, where the intracavity electric field is minimal (as demonstrated in the diagram Fig. 2.3(b)). The thickness of the DQWs is chosen to be 10 nm to increase their confinement energy. This ensures significant blue-detuning of their optical transitions compared to the main 20 nm QW which allows probing optically the 2DES independently of the DQWs.

From magneto-transport measurements, we estimate the 2DES electron density $n_e = 3.3 \times 10^{10} \text{ cm}^{-2}$ and the mobility $\mu = 1.6 \times 10^6 \text{ cm}^2 \text{ V}^{-1} \text{ s}^{-1}$. We deliberately choose a relatively low n_e to access the physics of the lowest Landau level in the range of magnetic fields available at that time in our experimental setup ($|B| \leq 8$ T, later extended to 16 T). The relatively high μ ensures that we can still probe FQH physics.

The conduction band diagram of sample A is shown in Fig. 2.11. It is based on solving the Schrödinger-Poisson equations to find the charge distribution and band edge for a given material composition. We used the Matlab AQUILA package [98] for this calculation. It displays the energy

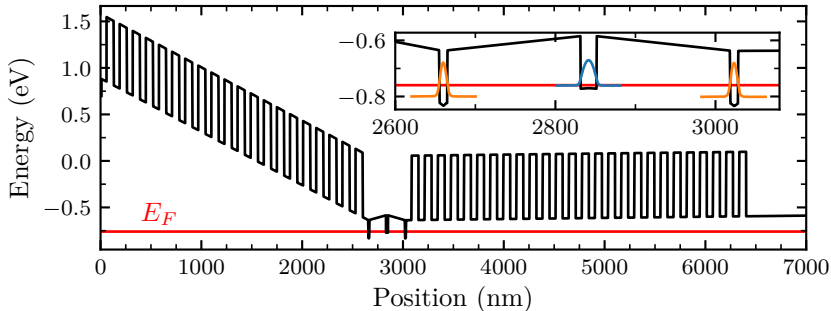


Figure 2.11: Conduction band diagram for sample A. The conduction band edge is shown in black (sample surface on the left). The inset displays an enlarged view of the DQWs and 2DEG, together with the lowest energy wave function confined to the respective quantum well. Fermi energy indicated in red.

of the conduction band edge on the y -axis against position, the growth direction pointing to the right. The magnitude of the wavefunctions of the lowest energy confined states in the different quantum wells are shown in the inset. The Fermi energy is displayed as red line. Most importantly, the charge carriers originating from the DQWs populate the center QW to form a 2DEG. Furthermore, in equilibrium there should be no carriers penetrating into mirrors as these states are located at much higher energies.

2.4.2 Sample B – High Density 2DEG

Structure B is very similar to A above, with two main differences: Increased number of DBR pairs with the goal to increase the Q -factor and increased electron density suitable for studies in magnetic fields up to 16 T. We used 24 and 29.5 pairs for the top and bottom DBR layers, respectively. The 2DEG is buried quite far below the surface in our structures due to the thickness of the DBR layers. It is often desirable to have direct access to the 2DEG for electrical contacting and optical experiments without polariton formation. We employed a binary wet-etching scheme to remove all but a few DBR layers. Two to four pairs were kept to avoid exposing the doping layer too close to the sample surface. Surface states can pin the Fermi level and lead to depletion of the 2DEG [40]. To remove a certain number of pairs, the

2. Cavity QED with Exciton-Polaritons and a 2D Electron System

Purpose	Solution	Composition	Time
Etch Al _x Ga _{1-x} As	Citric acid (50 %) / H ₂ O ₂	4:1	20 s
Stop etch, dry	H ₂ O, N ₂		
Etch AlAs	H ₃ PO ₄ / H ₂ O ₂ / H ₂ O	3:1:50	10 s
Stop etch, dry	H ₂ O, N ₂		

Table 2.1: Wet etching procedure to remove a single pair of DBR layers. Solutions kept at room temperature.

process listed in Table 2.1 was repeated the desired number of times.

The quality factor realized in this microcavity is only $Q = 4500$ despite the increased number of DBR pairs. It could be that the higher mirror reflectivity was compensated by increased background absorption in the DBR layers. The thickness gradient in this sample is very steep at the radial position of interest. The cavity resonance shifts by about 10 nm across a lateral distance of 1 mm. However, taking a measurement in the center, flat region of the wafer did not show an improved Q -factor. This hints at an MBE growth problem, which we were not able to identify yet. It could be due to a drift in growth rates within the run. Alternatively, an increased accumulation of strain in the thicker lower DBR could deteriorate the quality of the top layers. We also observe a reduced absolute contrast of 35 % in the reflection signal from this sample which is most likely related to this growth imperfection. Magneto-transport measurements characterize the 2DEG at $n_e = 1.9 \times 10^{11} \text{ cm}^{-2}$ and $\mu = 1.4 \times 10^6 \text{ cm}^2 \text{ V}^{-1} \text{ s}^{-1}$.

Structure B* is a copy of B without microcavity. To keep the layout comparable, the top DBR has been replaced by Al_{0.20}Ga_{0.80}As. Most importantly, this replicates the electrostatic environment by maintaining the distances between surface, doping layers and 2DEG. Magneto-transport measurements yielded $n_e = 1.0 \times 10^{11} \text{ cm}^{-2}$ and $\mu = 5.0 \times 10^6 \text{ cm}^2 \text{ V}^{-1} \text{ s}^{-1}$, values quite distinct from sample B. This again hints at potential growth issues for sample B, although we typically observe higher quality 2DEGs without a bottom DBR on which the 2DEG is grown.

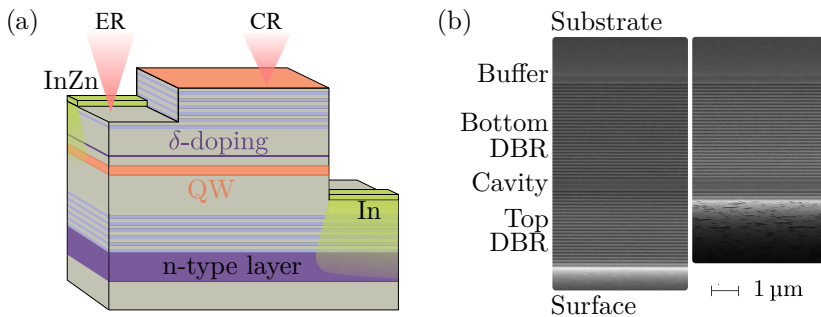


Figure 2.12: Chip processing and contacting example. (a) Schematic of sample C patterned into an etched region (ER) and a cavity region (CR). (b) Scanning electron microscope side-view of a typical microcavity sample. The left (right) image shows the same chip before (and after) performing the wet etching steps to remove the top DBR.

2.4.3 Sample C – Tunable Hole Gas

Sample C features a 15 nm QW. It is modulation doped on one side with carbon and embedded in a single λ microcavity¹⁵. The cavity is surrounded by 20 (24.5) pairs of DBR mirrors with resulting Q -factor of 5×10^3 . The sample was processed to achieve two goals: Contacting the two-dimensional hole gas (2DHG) in the QW separately from the n -type back gate and creating an etched region that allows accessing the 2DHG without microcavity. This was realized with two wet-chemical etching steps, resulting in a structure schematically drawn in Fig. 2.12(a). The 2DHG was contacted with $\text{In}_{0.96}\text{Zn}_{0.04}$ and the n layer with In. Another chip was patterned into a Hall bar geometry to characterize the 2DHG at $T = 250$ mK. A mobility $\mu = 1.1 \times 10^6 \text{ cm}^2 \text{ V}^{-1} \text{ s}^{-1}$ was found at a density of $n_h = 1.9 \times 10^{11} \text{ cm}^{-2}$. A diode-like structure is formed between the n -layer and the 2DHG which allows reducing the hole density (approximately linearly) by applying a negative bias voltage. At a density of $n_h = 0.6 \times 10^{11} \text{ cm}^{-2}$, the mobility is reduced to $\mu = 0.3 \times 10^6 \text{ cm}^2 \text{ V}^{-1} \text{ s}^{-1}$.

Figure 2.12(b) shows a side-view of a typical microcavity structure ac-

¹⁵All device fabrication related to sample C was performed by Dr. Mirko Lupatini. Detailed processing steps may be found in [99] or the thesis [100].

Sample (ID)	Density (10^{11} cm^{-2})	Mobility ($10^6 \text{ cm}^2 \text{ V}^{-1} \text{ s}^{-1}$)	Q -factor (10^3)
A (D160411A)	0.3	1.6	5.5
B (D170308A)	1.9	1.4	4.5
B* (D170508A)	1.0	5.0	-
C (D170807B)	0 to 1.9	0.3 to 1.1	5.0

Table 2.2: Summary of the electrical and optical sample characterization. For sample C, the mobility varies between the stated numbers from $n_h = 0.9 \times 10^{11} \text{ cm}^{-2}$ to $1.9 \times 10^{11} \text{ cm}^{-2}$.

quired using a scanning electron microscope (SEM). The layers with different aluminum fractions x appear contrasted in brightness in this image. The two panels show the same structure before (left) and after (right) performing the binary wet etching procedure described above to remove a certain number of layers. The parameters extracted from the sample characterizations discussed in this section are summarized in Table 2.2.

2.5 Polaron-Polariton Spectroscopy

Here, we combine all of the concepts explored so far and turn to experiments. Embedding a 2DEG inside an optical cavity allows studying the strong light-matter coupling regime with polarons instead of bare excitons. This leads to the emergence of new quasiparticles that we call polaron-polaritons. We carry out cavity spectroscopy of a 2DEG, presented in Fig. 2.13(a). Here, there is no external magnetic field applied, in particular there will be no QH effect. Such experiments will follow in the next chapter. In the diagram, normalized white-light reflectivity spectra are displayed along the y -axis, taken at different positions (x -axis) on a contacted but otherwise unprocessed chip of sample A. Due to the cavity wedge, this allows tuning of the cavity energy (diagonal dotted line labeled E_{cav}). The diagram shows the experimental realization of the anticrossing between material and cavity resonances introduced in Fig. 2.4(a). However, instead of a single excitonic mode [101], sev-

eral resonances appear in the doped QW under study. For the lowest energy anticrossing, we measure a normal mode splitting of $2\Omega_R \simeq 2.00 \pm 0.01$ meV. Since Ω_R is larger than the bare-cavity linewidth $\gamma_{\text{cav}} \simeq 280 \pm 10$ μeV , the system is in the strong coupling regime of cavity-QED and the elementary excitations should be characterized as cavity-polaritons.

Since the cavity-exciton coupling in this system is comparable to energy level splittings of the three exciton-like resonances, the polariton modes observed in the reflection spectrum can only be described as a superposition of all underlying resonances. A schematic of the relevant energy levels is provided in Fig. 2.13(b). We identify the lowest energy exciton-like resonance observed as the heavy hole attractive polaron (X_{attr})—a heavy hole exciton dressed by Fermi sea electron-hole pair excitations [21]. Since the attractive polaron resonance is associated with the bound-molecular singlet trion channel, it is also referred to as trion mode [59, 102]. We assign the middle-energy excitonic resonance to the heavy hole repulsive polaron (X_{rep}) [21, 84]. The energies of these two resonances are indicated by white dotted lines and labeled E_{attr} and E_{rep} , respectively. Finally, we tentatively identify the highest energy excitonic mode to the light-hole exciton. The absence of attractive and repulsive polaron branches associated with the light-hole exciton may stem from the absence of a bound light-hole trion, or from the lower oscillator strength and the larger broadening of these resonances.

It is evident from the experimental data that the simple Hamiltonian description of the polariton problem is not fully adequate. The upper polaritons in Fig. 2.13(a) are much broader than the lowest polariton mode. The fact that there is no symmetry between the different modes suggests that there are more dissipation channels than just cavity decay γ_{cav} . Indeed, this is already the case for exciton-polaritons in the absence of a 2DES. This is shown in Fig. 2.14(a) by depleting the charge carriers from sample C using a large negative gate voltage of $V_g = -9$ V. This measurement shows the cavity mode anticrossing with two resonances of the depleted quantum well: heavy hole exciton (E_{hh}) and light hole exciton (E_{lh}). Due to spatially inhomogeneous fluctuations of the QW width on the order of one to few atomic monolayers [103, 104], the exciton energies in our samples are distributed across several 100 μeV . On larger length-scales on the order of 10 μm to 100 μm , we observe line defects on the surface that may originate from strain accumulated from the finite lattice mismatch inside the thick DBR stacks. Finally, there could

2. Cavity QED with Exciton-Polaritons and a 2D Electron System

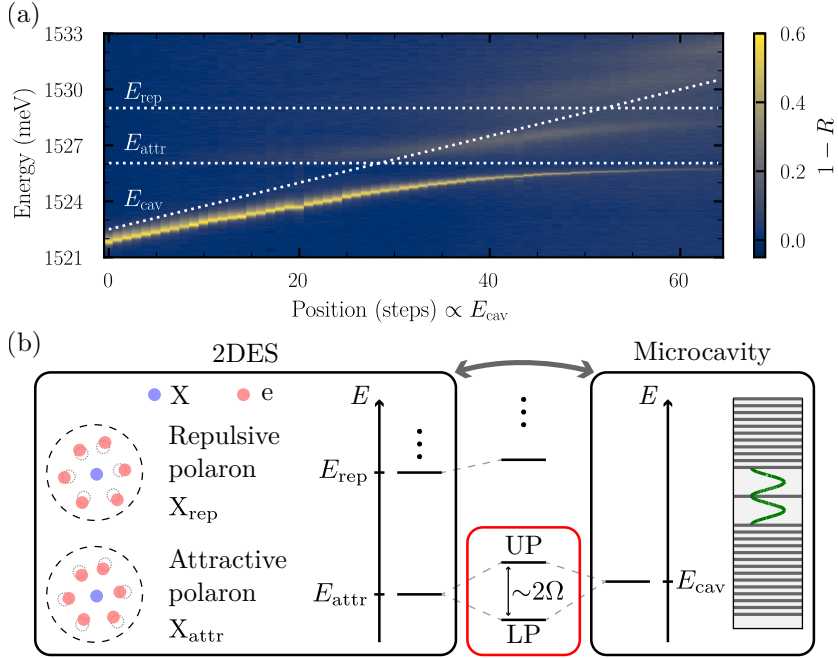


Figure 2.13: Polaron-polariton formation in a GaAs QW. (a) White light reflectivity spectrum of the system as we tune the cavity frequency. (b) Instead of bare heavy-hole excitons, the attractive and repulsive polaron branches of the 2DES couple to the optical mode of the microcavity. In the strong coupling regime, the lowest energy eigenstates of the coupled system are the lower polariton (LP) and the upper polariton (UP).

be a finite nonradiative decay rate for excitons. The upper polariton states are not perfect eigenstates and can decay into lower polaritons or optically dark excitons. The polariton linewidths are further increased in the presence of a 2DEG. The continuum of excitations supported by the electrons leads to further polariton scattering and therefore line broadening.

We turn to the dependence of polaron-polariton formation on the carrier (hole) density in Fig. 2.14. The low density case, where the polaron model is most adequate, is shown in Fig. 2.14(b). Comparing to the depleted case, a new anticrossing appears as the heavy hole exciton splits into attractive and repulse polaron branches (marked with E_{attr} and E_{rep}). Again, here the position on the sample (x -axis) is used to tune the cavity energy, which is approximately linearly increasing towards the right. This is a prototypical example for the regime we will be using throughout this thesis in terms of carrier density. The scaling of the attractive polaron (or collective trion) normal mode splitting has been found to increase with the square root of the density [64, 65]—akin to collective enhancement effects in cavity QED when coupling a single cavity mode to N atoms or emitters. In contrast, at more elevated densities (see third panel Fig. 2.14(c)), the repulsive polaron branch disappears and a description in terms of free electron hole pairs is more adequate [70, 71]. Line-cuts featuring a single background subtracted WL spectrum are shown in the lower panels Figs. 2.14(d) to 2.14(f). They have been taken across the lowest energy anticrossings, as indicated by the dotted lines in the upper panels.

It is insightful to look back at Fig. 2.6, which displays the underlying resonances that are now embedded in the cavity. We could infer the susceptibility of the quantum well as function of density and predict the resulting polariton modes. The complicated, non-Lorentzian structure of the polaron resonances can account for the broadening of upper polaritons in this picture [105]. Whenever the polariton branches overlap with a spectral region where the medium is lossy (imaginary refractive index), the resulting polariton mode is broadened. This perspective highlights the protection of the lower polariton mode from broadening that we make use of throughout this thesis. Thanks to the normal mode splitting Eq. (2.11), the lowest polariton mode is red-detuned from the onset of absorption in the medium and therefore protected from the dissipation that the bare resonances and upper polaritons experience. This requires the strong coupling condition to be satisfied

2. Cavity QED with Exciton-Polaritons and a 2D Electron System

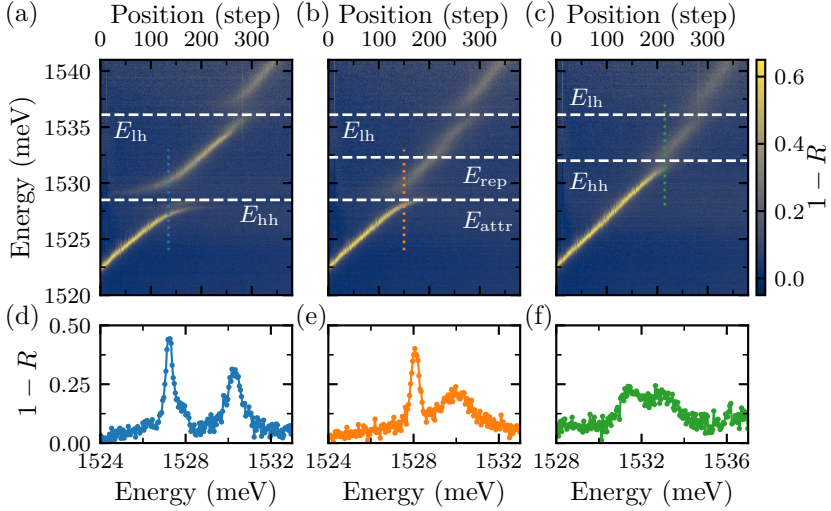


Figure 2.14: The anticrossing between cavity mode and polaron branches in a 2DHG for different hole densities n_h visible in white light spectroscopy. The matter resonances are marked with white dashed lines. (a) Depleted hole gas $n_h = 0$, $V_g = -9$ V. (b) Low hole density $n_h = 2 \times 10^{10}$ cm $^{-2}$, $V_g = -7$ V. (c) Higher hole density $n_h = 1.1 \times 10^{11}$ cm $^{-2}$, $V_g = -2$ V. (d-f) Line-cuts into the panels above, showing a single spectrum each, taken along the dotted lines in (a-c).

and the matter content $|X|^2$ low enough to prevent the lower polariton line from overlapping with the (potentially inhomogeneous) attractive polaron distribution.

Polaron-Polaritons in Integer and Fractional Quantum Hall States

Elementary quasiparticles in a two-dimensional electron system can be described as exciton polarons where electron-exciton interactions lead to dressing of excitons by Fermi-sea electron-hole pair excitations. A relevant open question is the modification of this description when the electrons occupy flat bands and electron-electron interactions become prominent. In this chapter¹, we perform cavity spectroscopy of a two-dimensional electron system in the strong coupling regime, where polariton resonances carry signatures of strongly correlated quantum Hall phases. We demonstrate the modification of polaron dressing under an external magnetic field that we associate with filling factor dependent electron-exciton interactions. The light-matter coupling strength is used to infer the electronic spin polarization and study magnetic ordering as well as skyrmion formation in the lowest Landau level. Discontinuities due to jumps in the Fermi energy and due to electronic incompressibility are identified in the optical spectra.

¹This chapter is based mainly on the work in article [106] and was done in collaboration with Dr. Sylvain Ravets. The hole spin polarization experiments were published in [99, 107] and performed together with Dr. Mirko Lupatini.

3. Polaron-Polaritons in Integer and Fractional Quantum Hall States

Two-dimensional electron systems (2DES) evolving in large magnetic fields are a fertile ground for many-body physics due to prominence of electron-electron interactions [108]. Formation of skyrmion excitations in the vicinity of filling factor $\nu = 1$ is a consequence of such interactions [109]. More spectacularly, electron correlations lead to the formation of fractional quantum Hall (FQH) states where the ground state exhibits topological order [110, 111]. Moreover, it has been proposed that a sub-class of FQH states exhibit non-abelian quasi-particles which can be used to implement topological quantum computation [22, 33].

It has recently been demonstrated that embedding a 2DES inside a microcavity realizes an alternate method for probing quantum Hall states [19]. In the strong coupling regime, polariton excitations are sensitive to elementary properties of the many-body ground state, such as spin-polarization and incompressibility due to their part-exciton character. In contrast to bare excitons though, polaritons are immune to decoherence processes such as phonon or impurity scattering due to their ultra-light mass, ensuring that they are delocalized. Consequently, the energy resolution achievable in polariton-based spectroscopy is only limited by the polariton decay rate due to mirror losses, which can be on the order of 20 mK in state-of-the-art microcavities [112]. The merits of the proposed sample design (Section 2.4) will be demonstrated. The design involves adjusting the separation distance between the 2DES and the doping layers to substantially reduce unwanted light-induced variations of the 2DES electron density n_e . This constitutes a major step forward for leveraging optical spectroscopy as a tool to study integer and fractional quantum Hall physics.

Using cavity spectroscopy is one of a diverse set of approaches to investigate quantum Hall physics. Electronic transport measurements are the most prominent experimental tool to investigate the celebrated quantized Hall conductance [40, 108]. But these measurements are macroscopic in nature, and many efforts are made to extract complementary information—in particular, local observables about the electronic wave function, chemical potential and compressibility. A non-exhaustive list of examples includes optical techniques [113, 114], quantum point contacts [115], coupling to Terahertz radiation [116], microwave impedance microscopy [117], scanning probe techniques [118], and many other local or near-field approaches.

This chapter starts with a brief review of experiments and theory regarding optical excitations of 2DEGs, extending our previous discussion to the case of an externally applied magnetic field. We revisit previous work by exploring Landau level spectroscopy in the quantum Hall regime in the absence of strong-light matter coupling, characterizing the polaron or collective trion-like resonances that will be hybridized with the optical cavity. We present the phenomenology of polaron-polariton modes coupled to integer quantum Hall (IQH) states before moving to a more quantitative analysis of the electronic spin polarization of the quantum Hall ferromagnet (QHF) at unity filling in the lowest Landau level. Investigating the QHF depolarization upon adding charged excitations, we find signatures of skyrmions in line with previous reports and study the special case of vanishing effective g -factor. We conclude with the coupling of polaron-polariton modes to fractional quantum Hall states and a discussion of perturbations to the 2DEG induced by light illumination.

3.1 Optical Excitations in Magnetic Fields

A magnetic field modifies the appropriate description of the optical response of a 2D electron system and also leads to the emergence of new transitions visible in experiments. We consider excitons in a magnetic field as a model system for the understanding of polarons. There are two important limits in terms of magnetic field strengths. For low magnetic fields, the states are perturbed and experience diamagnetic and Zeeman shifts [119]. In large magnetic fields ($l_B < a_B$), particles are restricted to a single Landau level. As the magnetic field tends to localize particles in the 2D plane, binding energies tend to increase with B . Above a few Tesla, the triplet trion becomes bound in GaAs and will appear in the emission spectrum [120]. The Zeeman shift splits the states linearly in B according to their angular momentum projection along the field axis. The diamagnetic term leads to a quadratic increase of the exciton energy with magnetic field. In the high magnetic field limit, excitons behave as free non-interacting particles [121].

On the experimental side, early magneto-optical studies found excitonic absorption into Landau levels [122]. Trions and excitons and their properties in magnetic fields were determined [59]. Various works explored modifica-

tions of optical spectra in the presence of integer [123–126] and fractional [95, 127–132] quantum Hall states. We will pursue cavity spectroscopy [19], which is sensitive to optical transitions that are bright, i.e. visible in resonant optical spectroscopy. This reduces the number of states that are accessible and simplifies the composition of polaritons as opposed to the numerous dark transitions observed in photoluminescence (emission) studies. In particular, isolated localized emitters are not efficiently coupled to the cavity and thereby avoided, which sidesteps some effects induced by disorder. On the other hand, this avoidance of optically dark states can be a disadvantage because also the (nominally) dark transitions can be a very useful spectroscopic tool, as has been shown for the triplet trions [113, 131].

Landau level quantization leads to flat electronic dispersion while excitons retain a finite effective mass [121, 133, 134]. This alleviates a limitation of the polaron model for the $B = 0$ case in GaAs, namely the large heavy hole mass compared to the electron effective mass. However, there has been less research dedicated to the description of Fermi polarons in a magnetic field. A step forward has recently been made [84], while progress towards a more detailed understanding in the presence of electron interactions is ongoing [135].

3.2 Landau Quantization and Integer Quantum Hall States

We study the optical response in the presence of a magnetic field perpendicular to the 2DES. Heavy hole valence band and the conduction band split into Landau levels LLn_{hh} and LLn_{cb} . The LL spectrum as a function of magnetic field is shown schematically in Fig. 3.1(a). Red (blue) mark allowed optical transitions $n_{\text{cb}} = n_{\text{hh}}$ for left-hand (right-hand) circularly polarized light. We use a fiber-based dilution refrigerator setup for the following experiments. A pair of aspheric lenses of numerical aperture $NA = 0.15$ arranged in confocal configuration focuses the incident light down to a $3.5\ \mu\text{m}$ diameter ($1/e^2$) spot, and collects the light reflected off the sample. We refer back to Section 2.3 for experimental details. For some experiments, the objective was slightly defocused—away from the confocal configuration—to reduce the effective NA and thereby the range of k_{\parallel} that the measurement integrates

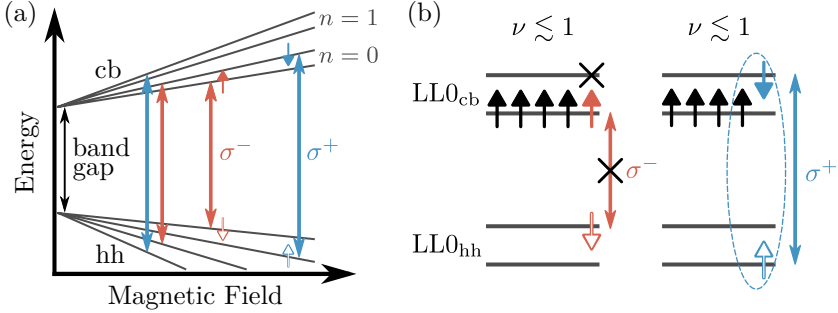


Figure 3.1: Optical transitions in a magnetic field perpendicular to the 2DEG plane. (a) Fan of Landau levels spaced by the cyclotron energy. Spin z states are split by the Zeeman energy and support circularly polarized dipole transitions across the band gap. (b) Optical absorption processes into a filled lowest Landau level ($\nu \lesssim 1$). Left: σ^- transition suppressed, right: σ^+ transition possible.

over. We remark that the magnetic field is the control variable in our experiments and not the LL filling factor. This is because samples A, B and B* do not allow for gate control of the electron density.

We start out by introducing Landau level spectroscopy of the bare 2DES as a function of magnetic field without optical cavity (top mirror removed, sample B) in Fig. 3.2. This allows to inspect the material resonances that will hybridize with the optical cavity mode to form polaritons. Figure 3.2(a) shows optical absorption into the Landau level fan, measured by white light reflectivity. The graph displays the measured spectra (with lamp spectrum normalized out) along the y -axis, repeated for different magnetic fields (x -axis). The colormap displays the reflectivity contrast: multiple resonances appear as yellow peaks which are the spectral regions where the 2DES absorbs light. The resonance energies are roughly linearly increasing in energy and correspond to different orders of LL to LL transitions, as expected from the picture presented in Fig. 3.1. The electron density is fixed, meaning the Fermi energy is only tuned via the magnetic field increasing the LL degeneracy. Starting from low magnetic fields, high energy LL indices n_{hh} , n_{cb} appear at first, because the lower lying LLs are completely filled with electrons. This forbids absorption of a photon, as there is no available density of final states to accommodate the excited electron. This observation implies

3. Polaron-Polaritons in Integer and Fractional Quantum Hall States

that we can estimate the fillings factor by detecting the onset of absorption into lower and lower energy LLs as B is increased. At some point, the available states per unit area in the Landau levels surpass the electron density and the lowest energy transitions are reached. This occurs below 3 T in the experiment shown in Fig. 3.2(a), with fillings $\nu = 2$ and $\nu = 1$ marked with white lines. The filling factor is counted with spin degeneracy broken, i.e. $\nu = 2$ already means that the transitions reach LL0. Therefore, $\nu = 1$ corresponds to the case where the number of electrons equals the available states in one spin subband only.

Various signatures of coupling to quantum Hall states arise, beyond the single particle expectation Fig. 3.1 based on the Landau level fan. Filling factors $\nu = 1$ and $\nu = 2$ are marked and accompanied by sharp discontinuities in the spectra. They appear as vertical stripes across the colormap, breaking the otherwise smoothly connected resonances as function of magnetic field. Further discontinuities are observed in the spectra towards lower magnetic fields which are higher $\nu = 3, 4, 5, 6, \dots$ integer states. There are a multitude of transitions, and the optical polarization degree of freedom is not yet resolved—the detected light is approximately linearly polarized so that both circular transitions have a finite projection into the detection basis. In the following sections, some of the deviations from the single particle Landau fan will be analyzed in more detail and linked to coupling of the optical excitations to the electrons experiencing the quantum Hall effect.

Figure 3.2(b) shows the optical emission spectrum (PL) for the same conditions, i.e. the same position of the optical spot on the sample and the same magnetic fields. Also, the optical detection setup is kept identically, just the excitations source is replaced by a red He-Ne laser at 632 nm (1960 meV), with excitation power on the order of 10nW. However, due to chromatic aberrations of the aspheric lenses, the excitation laser spot and detection area cannot simultaneously be confocal, so that a larger area of the sample is illuminated during PL experiments. The graph again plots the measured spectra along the y -axis, with different magnetic fields concatenated along the x -axis. The colormap displays the collected PL counts per second on a logarithmic scale, to highlight weaker features. In contrast to the resonant reflectivity measurements above, where background subtraction yields an absolute measure of the reflectivity contrast, the absolute count rate is not straightforward to interpret here. It does not solely depend on the tran-

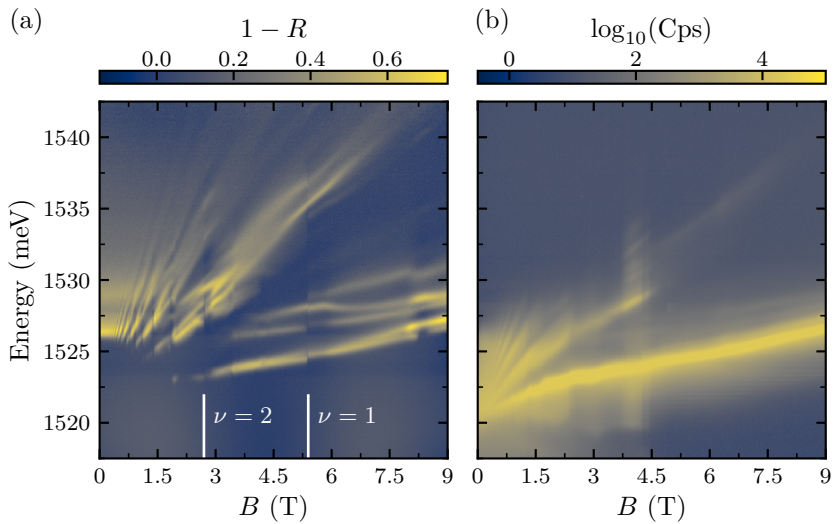


Figure 3.2: Landau level spectroscopy and coupling to QH states in sample B. Comparison between absorption and emission in a region without optical cavity. (a) White light reflectivity detected in approximately linear polarization, so that both circular branches are visible. (b) Photoluminescence for above band gap CW illumination, spectra in logarithmic scale.

3. Polaron-Polaritons in Integer and Fractional Quantum Hall States

sition oscillator strength but also on the populations of electron-hole pairs across different energies and momenta that follow multiple relaxation processes as well as exciton formation and carrier diffusion. However, for our purposes it suffices to track the emission lines in energy, while we leave out the analysis of emission intensity. First of all, it is striking how the emission lines are at lower energy overall compared to the absorption (the two panels use the same energy scale). For emission, the lowest energy recombining electron-hole pair is located at the bottom of the conduction band at zero momentum. In contrast, the absorption edge is shifted up in energy, also termed Moss-Burstein effect. This is due the lowest energy conduction band states being occupied by the 2DEG electrons, preventing absorption into the bottom of the band. This discrepancy between absorption and emission diminishes for $\nu < 1$, when all electrons and the optical excitation reside in the same LL. Furthermore, there are broad emission features below the lowest LL recombination (the brightest yellow line extending from 0 to 9 T) which correspond to processes where energy is left behind in the Fermi sea after emission. They correspond to shakeup processes [136–138], for example, an electron-hole pair recombines and an electron is promoted from LL n_{cb} to $n_{cb} + 1$. Next, one is tempted to compare the x -axes of the absorption and emission panels. However, a redistribution of emission in energy just below 4.5 T appears to mark filling factor 1, which is shifted to lower magnetic field compared to Fig. 3.2(a). This is somewhat expected as above band gap illumination causes significantly stronger light sensitivity (perturbation of the 2DEG by illumination, most prominently affecting the density n_e) and in this case leads to a reduction in electron density. We have not explored this effect systematically but the effect appears to depend on the energy of incoming photons and the detailed design of the heterostructure (other 2DEG samples show an increase in electron density with illumination). We also point out the decrease of emission strength towards higher photon energies, which is a consequence of carrier thermalization towards the lowest energy states at the band edges—but the population of electron-hole pairs is far from equilibrium before radiative recombination sets in because the bandwidth of emission energies observed is much larger than $k_B T \approx 10 \mu\text{eV}$.

3.2.1 Cavity Spectroscopy in the IQH Regime

We proceed with a side-by-side comparison of LL spectroscopy in the quantum Hall regime with and without optical cavity to illustrate the consequences of strong light-matter coupling. We use two separate regions on one chip of the hole gas sample C² for this purpose, one without cavity, realized by removing the top mirror (results from this area are shown in Figs. 3.3(a) and 3.3(b)) and one with cavity (Figs. 3.3(c) and 3.3(d)). Since the top gate controlling the hole density n_h has finite electrical resistance, there is no position-independent relation between gate voltage V_g and n_h . We chose the panels to match approximately in density but a small difference remains. All four panels constitute normalized white light reflectivity measurements.

The detection is performed polarization resolved. The left column shows light detected in left-circular, σ^- polarization coupling to the lower lying spin state. The right column corresponds to right-circular, σ^+ polarization which couples to the higher lying spin state. Since the optical transitions X_{attr} have spin-singlet character and couple to opposite spins for the circular polarizations, the optical response depends strongly on the electronic spin configuration. We focus on the most prominent feature at $B = 2.5$ T in the vicinity of unity filling $\nu = 1$. Figure 3.3(a) displays a dark blue interruption in the lowest LL absorption line while the resonance with the third LL brightens at $E = 1531$ meV (white mark). Due to the formation of a quantum Hall ferromagnet, all hole states are occupied in the lowest LL Fig. 3.1(b) or equivalently, no electrons are available to be excited across the band gap. The oscillator strength is transferred to the transition into the next higher energy LL. The behavior is opposite for the other polarization Fig. 3.3(b). Here, the increased spin polarization due to the ferromagnetic state removes holes $|\uparrow\rangle$ and the transition connecting $n_{\text{hh}} = 0$ and $n_{\text{cb}} = 0$ brightens up.

We can understand the polariton spectra in the lower panels by translating the observed features in the region without cavity. As the oscillator strength is the only variable determining the light-matter coupling strength in Eq. (2.9) at fixed energy of the resonance, the observed contrast in the

²At this level, the hole and electron gas samples are interchangeable in the sense that qualitative understanding is based on equivalent arguments after exchanging the electron population with a hole population in the valence band in Fig. 3.1(b).

3. Polaron-Polaritons in Integer and Fractional Quantum Hall States

upper panels translates to normal mode splitting between lower and upper polaritons for the cavity region. The normal mode splitting collapses in Fig. 3.3(c) and the polariton branches touch at $\nu = 1$. On the contrary, the two branches separate further in Fig. 3.3(d) (white mark). We make simplifying assumptions in this description, most importantly: only two modes are relevant, namely the cavity and one attractive polaron in the lowest LL. Second, that the detuning in Eq. (2.11) is zero, as such an energy difference between the cavity mode and the material resonance leads to an additional separation between lower and upper polaritons. The detuning is set by the position on the sample which controls the cavity energy and its choice is verified by the fact that the polariton splitting vanishes in Fig. 3.3(c). The first assumption is not strictly correct as we clearly see multiple resonances in the upper panels. However, their importance diminishes roughly with $(\Omega_R/\Delta E)^2$ for an energy detuning ΔE from the cavity. Another way to interpret coupling to other material transitions is factoring it into an effective cavity mode that already contains a small but finite matter content and an energy shift due to these couplings. Now if the couplings and detunings vary slowly across the parameter space of interest, they will not alter the simplified two-mode picture significantly.

We conclude with an exploration of the IQHE in the low electron density and high mobility sample A. To explore the interplay between quantum Hall states and polaritonic excitations, we again tune E_{cav} to ensure that the dressed photonic mode resulting from non-perturbative coupling between the bare cavity mode and the higher energy excitonic states is resonant with X_{attr} at unity filling. We estimate the energy of the bare cavity mode to be $E_{\text{cav}} \approx 1526.6$ meV. In Fig. 3.4, a feature qualitatively similar to sample C is observed at $\nu = 1$. The spin state of the optically generated electron is again determined by the photon polarization: left-hand circularly polarized light σ^- probes transitions to the lower electron Zeeman spin subband $|\uparrow\rangle$, displayed in Fig. 3.4(a) and right-hand circularly polarized light σ^+ probes transitions to the upper electron Zeeman spin subband $|\downarrow\rangle$, Fig. 3.4(b). Now the schematic in Fig. 3.1(b) applies for the case for carriers in the conduction band and the observed spectral signatures are strongly dependent on how the electrons are arranged in the LLs i.e. on the spin-polarization of the different ground states of the 2DES [94, 95]. Coupling to integer QH states with $\nu \geq 2$ is also visible in Fig. 3.4. Albeit less and less pronounced than for $\nu = 1$, a

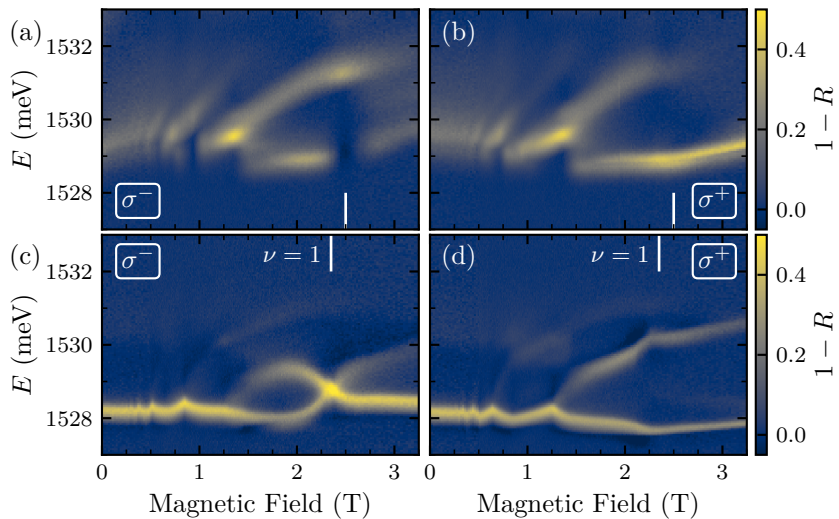


Figure 3.3: Polarization resolved Landau level spectroscopy on the hole gas sample C. Comparison of white light reflectivity spectra without (a-b) and with (c-d) optical cavity in the IQH regime. Left column detected in σ^- , right column in σ^+ polarization. All panels display similar hole gas densities with $n_h = 0.6 \times 10^{11} \text{ cm}^{-2}$ ($V_G = -5.5 \text{ V}$) in the top row and $n_h = 0.56 \times 10^{11} \text{ cm}^{-2}$ ($V_G = -5 \text{ V}$) in the bottom row resulting in $\nu = 1$ around $B = 2.5 \text{ T}$.

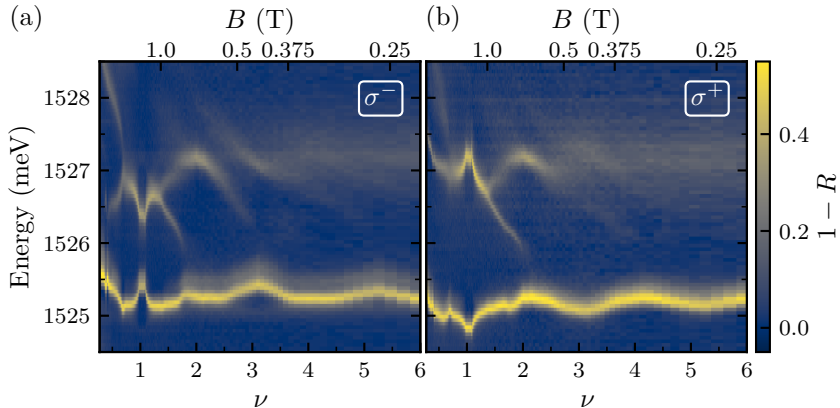


Figure 3.4: Cavity spectroscopy of sample A in the IQH regime, as we tune B for fixed cavity energy $E_{\text{cav}} \approx 1526.6$ meV. White light reflectivity measurements performed with (a) σ^- and (b) σ^+ circularly polarized light.

similar spectral feature repeats at every odd integer $\nu = 1, 3, 5, \dots$ filling: a polariton gap closes in σ^- polarization but not in σ^+ . In particular, the σ^- lower polariton energy shifts upwards at odd integer fillings, while the σ^+ branch shifts down in energy.

3.2.2 Electronic Spin Polarization and Skyrmion Formation

By probing $|\uparrow\rangle$ and $|\downarrow\rangle$ electronic spin states independently using σ^- and σ^+ polarized light, we can evaluate the spin polarization of the underlying 2DES. This makes the analysis of the previous section quantitative, by measuring the normal mode splittings Ω_{σ^-} and Ω_{σ^+} which allows calculating the normalized ratio P :

$$P = \frac{\Omega_{\sigma^+}^2 - \Omega_{\sigma^-}^2}{\Omega_{\sigma^+}^2 + \Omega_{\sigma^-}^2}, \quad (3.1)$$

where $\Omega_{\sigma^\pm}^2$ is directly proportional to the oscillator strength of the associated optical transitions. This assumes the cavity energy E_{cav} has been tuned into resonance, as for the case with two polariton modes Eqs. (2.9) and (2.11). The values $\Omega_{\sigma^\pm}^2$ are extracted by fitting Lorentzian line shapes to the upper and lower polaritons to extract the resonance energies. It has

been demonstrated that there is a direct correspondence between the the oscillator strength ratios in the two circular polarizations and electronic spin polarization S_z of the underlying 2DEG [95, 124, 125, 139, 140]. We translate this to cavity spectroscopy, where the oscillator strength manifests as normal mode splittings [19], so that P provides an estimate for S_z :

$$S_z = \frac{N_{\uparrow} - N_{\downarrow}}{N_{\uparrow} + N_{\downarrow}} \simeq P, \quad (3.2)$$

with $N_{\downarrow(\uparrow)}$ the number of spin-down (spin-up) electrons in LL0. In particular, for $\nu \leq 1$, P and S_z were claimed to coincide exactly [95, 124] for optical absorption if two assumptions are met. The intensity of the singlet trions $I_{\sigma^+(\sigma^-)} \propto f_{\downarrow(\uparrow)} N_{\downarrow(\uparrow)}$ scales with the number of spin up (down) electrons $N_{\uparrow(\downarrow)}$ and the fraction of unpaired spins available for singlet formation $f_{\uparrow(\downarrow)}$ is unity for $\nu \leq 1$. To simplify the analysis, we make a further assumption that leads to Eq. (3.2) holding only approximately: we disregard the additional cavity detuning introduced when oscillator strength is transferred from LL transition n to $n+1$. For optical absorption, the corresponding condition is to integrate $I_{\sigma^+(\sigma^-)}$ over all LL transitions n , which is also challenging to implement in the presence of other resonances. We briefly compare the two procedures based on absorption and cavity spectroscopy to determine the spin polarization. Absorption spectroscopy requires the determination of the transition oscillator strengths, accurately resolved in circular polarizations σ^+ and σ^- . This information can be inferred from intensity measurements. Cavity spectroscopy provides a more robust technique by relaxing this condition: The transitions strength is converted to an energy difference between polariton modes which can very accurately be determined via spectroscopy. Furthermore, imperfect polarization control leads to the appearance of two families of polariton modes in one shot, but without changing the extracted polariton energies and therefore without affecting the extracted value S_z . These benefits are traded against the new requirement to either set the detuning between cavity mode and polaron to zero or to measure it independently and to take it into account. The absorption measurement allows for a local measurement on micrometer scales given by the diffraction limit, while the cavity modes being planar in nature tend to be delocalized over larger areas. The reduction of spatial resolution is a disadvantage but comes with corresponding

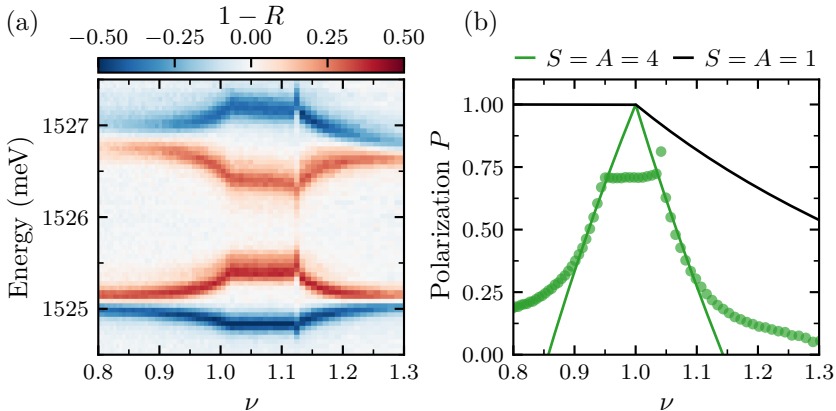


Figure 3.5: Electronic spin polarization in sample A around $\nu = 1$ and evidence for skyrmions. (a) Difference between the spectra in σ^- and σ^+ polarization shown in Fig. 3.4 close to the $\nu = 1$ plateau. (b) Polariton polarization P (green circles) extracted from the polariton energies in (a). Inferred spin polarization $S_z = P$ of the 2DEG with expected depolarization due to Skyrmions with size 1 (single-particle case, black) and size 4 (green).

benefits, such as the possibility to reduce the undesired consequences of light illumination on the sample, as detailed in Sections 2.4 and 3.3.4. Finally, the polariton resonance line widths are mostly determined by the cavity quality factor and are, for our systems, much narrower than the underlying polaron transitions which presents a technical advantage. A side-by-side comparison between both methods can be found in the thesis [100, Chapter 5] for sample C, with an exemplary case where cavity spectroscopy was advantageous.

We perform an analysis of S_z in the vicinity of $\nu = 1$ for sample A. Figure 3.5(a) shows the normalized white light reflection spectrum as a function of the filling factor ν , varied by scanning B . Here, we tuned E_{cav} close to resonance with the $|\uparrow\rangle$ -transition of the lowest Landau level LL0 at $\nu = 1$. The difference between σ^- (red) and σ^+ (blue) spectra is shown to directly compare both pairs of lower (LP) and upper polariton (UP) branches. The extracted polarization and estimate for the spin polarization is presented in Fig. 3.5(b) (green circles). We obtain $S_z \simeq 70\%$, suggesting that full polarization is not achieved at $\nu = 1$, contrary to what is expected for a perfect quantum Hall ferromagnet. In our low n_e sample, incomplete polarization

may arise due to disorder and reduced screening of impurity potentials [139, 141]. Furthermore the cyclotron frequency is comparable to the exciton binding energy, ensuring that exciton formation has a sizable contribution from higher LLs which might affect the relationship between P and S_z . Also, contribution of higher energy levels to polariton formation, via off-resonant coupling, could lead to a non-vanishing Ω_{σ^-} at exactly $\nu = 1$, so that P only gives a lower-bound to the actual value of S_z . We return to these points and the sharp feature visible at the right edge ($\nu = 1.125$) of the plateau in Section 3.3.4. However, we also want to point out that there is no inherent limitation in the cavity spectroscopy approach that would limit the maximum resolvable spin polarization. As we will see throughout this chapter, fillings $\nu = 2/5$ and $1/3$, as well as $\nu = 1$ in sample C can indeed yield an extracted spin polarization close to 100%.

Tuning the filling factor away from $\nu = 1$ leads to a rich structure in the reflectivity spectrum presented in Fig. 3.5 that relates to the way the electrons arrange in the different LLs as we detune B . We first observe a rapid, symmetric depolarization on both sides of $\nu = 1$ which is compatible with formation of many-body spin excitations in the ground state. The depolarization was interpreted in terms of skyrmions and anti-skyrmions [124–126, 139, 140, 142]. They were proposed as lowest energy charged excitations of the QHF [143, 144] resulting from a competition between Coulomb and Zeeman energies, with first evidence from nuclear magnetic resonance experiments [145, 146] and magneto-transport [147]. Exchange interactions favor locally parallel spins [148] so that a spin texture arises where spins are slowly canted from one spin at the origin to the opposite spin far outside in a vortex-like pattern. They have an energy cost of about 30 K and are therefore frozen out at $\nu = 1$. But moving slightly off $\nu = 1$, they constitute the lowest energy configuration to accommodate the additional charge [148].

The solid lines in Fig. 3.5(b) show a model for the evolution of S_z based on skyrmions [125, 145], where the modification of available density of states due to skyrmion formation is parameterized by A ($\nu \leq 1$) and S ($\nu > 1$) which characterize the size of the spin texture in terms of number of spin

flips per charge excitation:

$$S_z = \begin{cases} S \left(\frac{2-\nu}{\nu} \right) - (S - 1), & \nu > 1, \\ \frac{1}{\nu} - (2A - 1) \left(\frac{1-\nu}{\nu} \right), & \nu \leq 1. \end{cases} \quad (3.3)$$

We obtain $S = A \approx 4$ (green curve), in agreement with previously reported values for samples of similar electron densities [124, 125, 139]. Note the striking difference between the experimental data and the case $S = A = 1$ (black line), which constitutes the single-particle picture. Summarized in other words, the rapid depolarization away from $\nu = 1$ implies that for each electron added to the system, three additional spins from the QHF are reversed to arrive at $S = 4$ instead of $S = 1$.

3.2.3 Skyrmions at a Landau Level Crossing

We return our attention to Skyrmions once more, for the case of a 2D hole gas [149, 150]. This system will allow us to tune the energy ratio $\tilde{g} = E_Z/E_C$ between effective Zeeman energy and Coulomb energy scales which determines the energy and optimal size of skyrmions [109]. Strong Coulomb interactions $E_C \sim \frac{e^2}{4\pi\epsilon_0\epsilon l_B}$ favor distributing the charge excitation over a large area while a large Zeeman energy tends to limit the excitation to single spin flips. Tuning the effective Zeeman energy to zero at a Landau level crossing [151–157] should enhance the Skyrmion size [158, 159]. Other studies used hydro-static pressure [158] or a particular Aluminum concentration (Al_{0.13}Ga_{0.87}As/GaAs) [159] to tune the g factor close to zero. Using cavity spectroscopy, we are able to extract the hole spin polarization to map out the order of the QHF in the vicinity of vanishing g factor. This is achieved in proximity to a crossing between two valence band Landau levels.

We demonstrate the occurrence of a LL crossing in Figs. 3.6(a) to 3.6(c). They depict cavity spectroscopy performed for increasing hole gas densities of 2.9, 3.6 and $4.2 \times 10^{10} \text{ cm}^{-2}$, with the difference between σ^- and σ^+ polarizations color-coded from red to blue in the colormap. Within each panel, the magnetic field is then varied (x -axis) to tune the filling factor. As the hole density is increased, the critical magnetic field B_{cr} of the LL crossing turns out to change and can be tuned across $\nu = 1$. This is manifest in

the polarization resolved white light reflectivity by a change in roles between the σ^+ and σ^- transitions and thereby the σ^\pm polariton branches. Figure 3.6(b) highlights the change in roles at $B = 1.46$ T. The diagrams in Figs. 3.6(a) and 3.6(c) look qualitatively the same, but with red and blue colors swapped, as expected for the LL crossing occurring between those hole densities. The experimental observation of the LL crossing is supported by a 8x8 Kane model simulation [160] for $n_h = 4 \times 10^{10} \text{ cm}^{-2}$ in a 15 nm GaAs/Al_{0.21}Ga_{0.79}As quantum well. While the conduction band LLs scale linearly with magnetic field, the behavior in the valence band is more complex. Due to mixing between heavy hole and light hole bands, they disperse nonlinearly as function of magnetic field and may cross. The two lowest levels ($m_z = \pm 3/2$ at $B = 0$) are expected to cross around $B_{\text{cr}} = 1.6$ T. This prediction, the intersection of the blue and red-dashed valence band Landau levels in Fig. 3.6(d), agrees well with the observed spin flip. The blue line corresponds to a pure heavy-hole state with $m_z = 3/2$, while the red-dashed level starts out as $m_z = -3/2$ but acquires a light-hole character $m_z = 1/2$ of 10% at $B = 5$ T (not displayed).

White light reflectivity measurements have been obtained as a function of both magnetic field and hole density and the polarization extracted according to Eqs. (3.1) and (3.2). The results are condensed in Fig. 3.6(e), where the white region (absence of spin polarization) marks the spin flip or level crossing. This region separates the spin polarized \uparrow blue and \downarrow red regions in the phase diagram. A fast re-polarization of the QHF is observed along the y -axis on both sides of the crossing at $\nu = 1$. There is no mirror symmetry around the $\nu = 1$ axis due to the effects of the LL crossing. This asymmetry is also captured by the simulation Fig. 3.6(d). The energy difference between the two spin subbands (i.e. the distance between blue and red-dashed lines) is much smaller for $B < B_{\text{cr}}$ than it is for $B > B_{\text{cr}}$. Therefore, the lack of symmetry need not imply a violation of particle-hole symmetry. Further considering the evolution along the x -axis, the spin polarization drops very abruptly towards the LL crossing from both spin polarized states. The depolarization slopes suggest skyrmion sizes increasing up to $S, A \approx 15$ [99] towards the LL crossing.

³The simulations of the LL fan diagram and crossing were kindly provided by Prof. Roland Winkler.

3. Polaron-Polaritons in Integer and Fractional Quantum Hall States

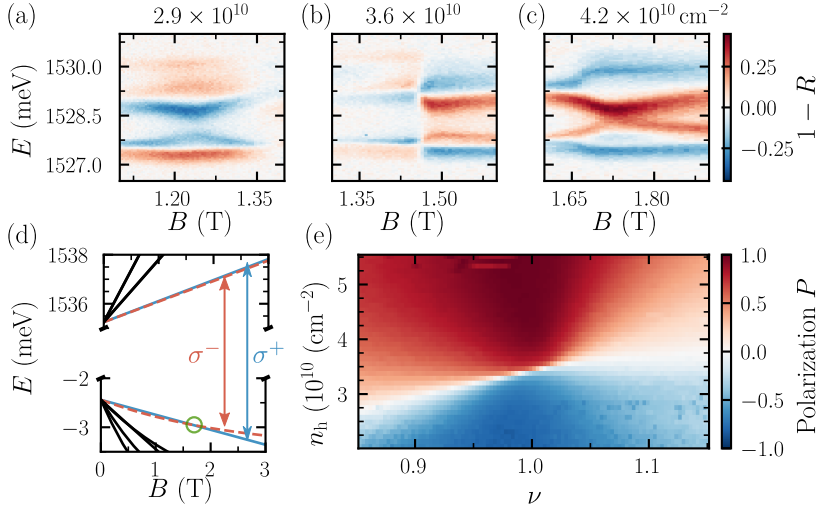


Figure 3.6: Landau level crossing and associated hole spin flip of the ground state in sample C. The depolarization of the QH ferromagnet as a function of ν varies strongly with hole density which could be due to proliferation of skyrmions at low effective Zeeman splittings. (a-c) Difference of polarization resolved white light reflectivity spectra around $\nu = 1$. From (a) to (c), the LL crossing is tuned (via hole density) across this magnetic field range, as evidenced by σ^+ and σ^- polarizations switching roles. (d) Numerical simulation confirming the LL crossing in the valence band³. (e) Map of S_z inferred by polariton polarization P .

An alternative explanation to skyrmions for the depolarization dependence, especially the broadening of the white transition region in Fig. 3.6(e) could be provided by a nematic phases [161–167]. So far, we have not found clear discriminating evidence between these alternatives from our experiments.

3.3 Fractional Quantum Hall States

We continue our investigation with fractional quantum Hall states in the lowest Landau level. They can be detected via the electronic spin polarization as is the case for the integer fillings studied before. Furthermore, we explore effects that can be attributed to incompressibility of the electron gas. We conclude with FQH features in the second Landau level and an investigation of the polariton response at high magnetic fields.

We investigate coupling to FQH states in sample A by scanning the magnetic field to up to 5 T for an increased value of $E_{\text{cav}} \approx 1527.8$ meV. The experiment is displayed in Fig. 3.7. Normalized white light reflectivity spectra are shown as function of magnetic field, tuning the filling factor at fixed n_e . Increasing B reduces ν , thus leading to absorption in a partially filled lowest LL [131, 168, 169]. Cavity coupling to several FQH states is observed as a ν -dependent normal mode splitting in both polarizations (Fig. 3.7(c)). The behavior is reminiscent of the ν -dependence in the integer QH regime shown in Figs. 3.3 and 3.4, in that the polariton branches merge for even ν and split for odd ν , shown up to $\nu = 7$. Remarkably, these signatures are also present in the fractional QH regime, where we observe features at filling factors $\nu = 1/3, 2/5, 3/7, 2/3$ and $5/3$ (not shown). Such spectral signatures are particularly striking when ν reaches the fractional values $\nu = 1/3, 2/5$, and $2/3$. We observe that Ω_{σ^-} and Ω_{σ^+} differ significantly at $\nu = 1/3, 2/5$, which shows that these fractional QH states carry a sizable spin-polarization. On the contrary, $\Omega_{\sigma^-} \approx \Omega_{\sigma^+}$ and the merging of the two lower polaritons lines at $\nu = 2/3$ shows that this state is not polarized, as expected for samples with n_e in the range of the one studied here. Increasing n_e should allow us to probe the phase transition from an unpolarized to a polarized $2/3$ -state [19, 170] as we will show in sample B below.

We now focus on filling factor $\nu = 2/5$, an enlarged version of the σ^-

3. Polaron-Polaritons in Integer and Fractional Quantum Hall States

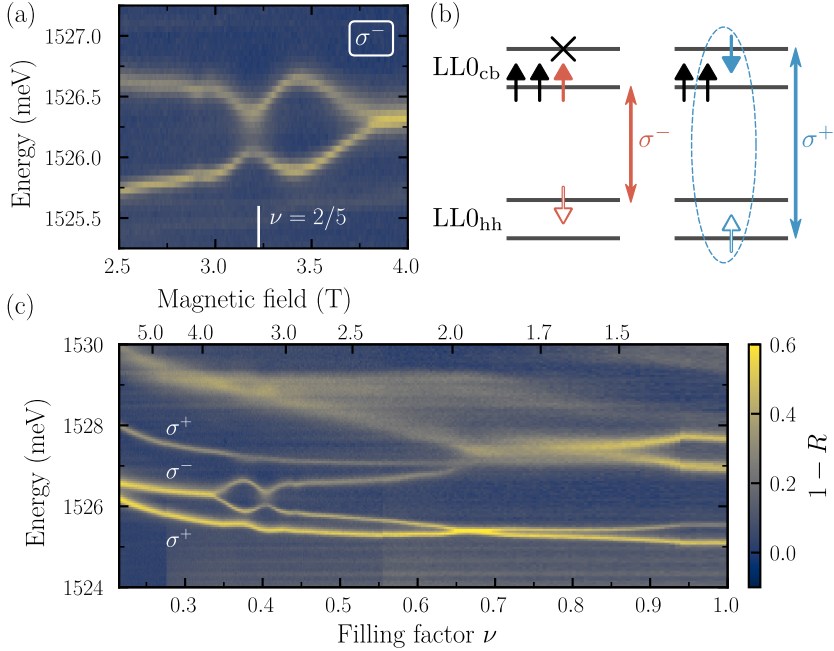


Figure 3.7: Cavity spectroscopy (sample A) in the fractional quantum Hall regime, as we tune B for fixed $E_{cav} \approx 1527.8$ meV. (a) Highlight of the optical signature at the spin-polarized fractional state $\nu = 2/5$ in σ^- polarization. (b) Relevant energy levels and optical transitions around $\nu = 2/5$. In contrast to $\nu = 1$, phase space filling is blocking neither of the circular polarizations. Formation of a singlet polaron at $\nu = 2/5$ is nevertheless prevented in σ^- polarization, due to the absence of screening electrons of opposite spin. (c) Sum of σ^- and σ^+ spectra against filling factor (magnetic field).

experiments is shown in Fig. 3.7(a). For $\nu = 2/5$, we observe a high degree of the polarization $S_z \geq 92\%$. In stark contrast with the integer QH states, both $|\uparrow\rangle$ and $|\downarrow\rangle$ states are available and phase-space filling can only play a marginal role here. An energy level drawing is depicted in Fig. 3.7(b). One striking feature is that the collapse of Ω_{σ^-} around $\nu = 2/5$ is not accompanied with an appreciable increase in Ω_{σ^+} , contrary to what was observed for $\nu = 1$. Because the LLs are partially filled, the mechanism leading to modification of the polariton splitting is indeed modified. We argue that the decrease Ω_{σ^-} for a spin-polarized state is due to the polaron nature of optical excitations that are accessible when promoting an electron into the $|\uparrow\rangle$ state with σ^- -polarized light. For a fully polarized state, all electrons are in the same $|\uparrow\rangle$ state and there are no electrons in the $|\downarrow\rangle$ state. Since the oscillator strength of the σ^- singlet X_{attr} is proportional to the density of $|\downarrow\rangle$ electrons, perfect spin polarization would lead to vanishing cavity coupling. In contrast, promotion of an electron in the $|\downarrow\rangle$ state with σ^+ -polarized light always leads to formation of a singlet polaron excitation with electrons available in the $|\uparrow\rangle$ state, and the polariton splitting is only marginally modified.

In Fig. 3.8, we study the coupling to FQH states at higher electron density and magnetic fields in sample B in a region with optical cavity. The overall signal to noise ratio is reduced compared to sample A, solely due to a less optimized optical cavity which manifests itself in a reduced reflectivity contrast. We plot white light spectroscopy data in Fig. 3.8(a) in roughly linear polarization, which is the cavity counterpart to Fig. 3.2 in the IQH regime. The features already described in the previous sections are reproduced in this sample. The lowest polariton modes split at odd integers and merge at even integers, heralding the modulation of spin polarization with ν . At $B = 3.5$ T, a new branch appears due to the lowest LL transition becoming available below $\nu = 2$. Faintly visible resonances between 0 and 3 T, increasing linearly in energy with magnetic field are reminiscent of the Landau level fan. The LL fan is visible almost unperturbed by cavity coupling due to the low cavity content of those polariton branches. Fractional states are visible in Figs. 3.8(b) and 3.8(c). The panels are labeled with σ^\pm polarizations but only imperfect polarization resolution was achieved in this measurement, leading to a finite contamination by branches of the opposite polarization. The $\nu = 2/3$ state underwent a phase transition to a spin polarized state

[170, 171] and features a signature between 8 and 9 T that resembles the spin polarized $\nu = 2/5$ in sample A.

Finally, we compare WL and PL measurements at $B = 8.7$ T, close to $\nu = 2/3$, as a function of positions across the sample. This connects to Section 2.5 where we showed such data in the absence of a magnetic field. Figure 3.8(d) demonstrates the strong coupling and formation of well resolved polariton branches at this elevated electron density $n_e \approx 1.9 \times 10^{11} \text{ cm}^{-2}$. The polariton mode starts out purely photonic ($|C|^2 \approx 1$) in the bottom right hand corner and hybridizes with material excitations towards smaller positions. A diagonal line from the top left corner to the bottom right corner of this panel provides a good first estimate to the bare cavity energy. Figure 3.8(e) shows emission following above band gap excitation for the exact same positions. Efficient relaxation to the lowest energy excited state ensures that the emission originates predominantly from the lowest polariton branch.

Throughout this section, the cavity detuning has been chosen to probe the IQH and FQH effects with the lowest polariton which is the narrowest and therefore easiest to resolve. However, the upper polaritons also display complex features. These remain to be studied in the future. The cavity detuning was adjusted to split the cavity weight about equally between the lowest two branches, which would correspond to $\Delta = 0$ if there were no higher energy resonances contributing. During magnetic field sweeps, we keep E_{cav} constant, which substantially simplifies WL background subtraction and avoids artifacts from spatial inhomogeneity accrued when moving across the sample. This procedure has the disadvantage that Δ is not constant but slowly varying with magnetic field, mainly due to diamagnetic shifts.

3.3.1 Composite Fermions and Incompressibility

We briefly abandon cavity spectroscopy and investigate sample B* without optical cavity in search for features of electronic incompressibility in the emission spectrum. We study the PL emission from 0 to 16 T in Fig. 3.9(a). The logarithm of the acquired spectra is displayed with emission energy along the y -axis. At low fields 0 T to 3 T, the LL fan emission is visible, similarly to Fig. 3.2(b). The jumps in chemical potential as integer fillings are crossed by the magnetic field are especially well resolved. They are marked

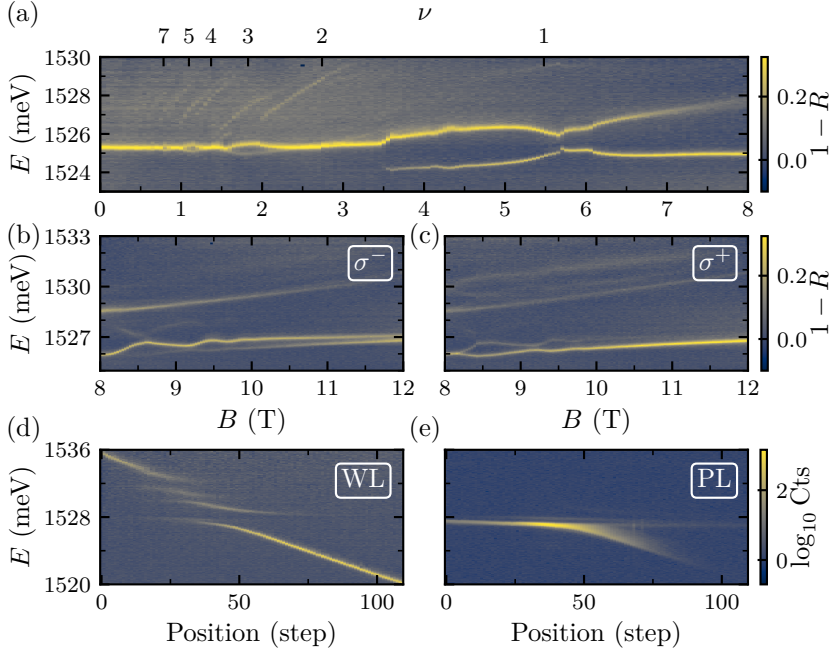


Figure 3.8: Cavity spectroscopy in the QH regime for sample B. (a) Overview from 0 to 8 T with estimated integer fillings indicated on top. (b) FQH regime in σ^- and (c) σ^+ polarization. (d) Spectra taken at $B = 8.7$ T along a line of different positions on the sample, tuning the cavity energy. Color scale as in (a-c). (e) Exactly the same positions as in (d) but detecting PL emission following above band gap excitation.

with white marks in the top left corner, starting with $\nu = 1$ to 2, 3 and 4. We reproduce the experimental features observed in [169] where internal structure in the emission line and a jump in energy just above $\nu = 1/3$ were attributed to fractional quasiparticles coupling to the exciton and electronic incompressibility. The authors speculate that the two resonances at fillings $\nu \leq 1/3$ correspond to an exciton (high energy resonance) and a exciton dressed by magnetorotons (lower energy resonance). At the end of the Hall plateau indicated by σ_{xy} towards lower field $\nu \geq 1/3$, a new lower energy resonance occurs which is attributed to a exciton dressed by fractionally charged quasi-particles. They argue that a process akin to trion formation takes place lowering the emission energy, once quasiparticles become mobile in a metallic phase outside the Hall plateau [169]. We focus on the discontinuity in the region marked by the gray box. The white mark in Fig. 3.9(a) marks $\nu = 1/3$ extrapolated from the discontinuities at integer fillings at lower fields to $B = 9.6$ T. Consistent with the analysis in the work [169], the largest jump in energy occurs at field below $\nu = 1/3$, here at 9.2 T. An enlarged colormap of spectra versus magnetic field is plotted in the two circular polarizations in Figs. 3.9(b) and 3.9(c) on a linear scale⁴. Similar fine structure of the emission lines around $\nu = 1/3$ have been reported [132, 172]. We mention another work where a blue-shifted optical signature around $\nu = 1/3$ was tentatively attributed to the Coulomb gap of an incompressible Laughlin liquid [173]. While the interpretation of these experiments around $\nu = 1/3$ remains speculative, the experimental signatures are both striking and reproducible. We believe this situation warrants further work.

3.3.2 Effective Polaron-Polariton Mass

We address the question of the modification of the polaron-polariton effective mass in the vicinity of $\nu = 2/5$ using a setup with free space access. We use a NA = 0.68 lens to excite a broad range of in-plane momenta k_{\parallel} using the same broadband light emitting diode as before. A lower NA lens couples the reflected light into a fiber, which enables angle selective measurements, as discussed in Section 2.3.2. The energy-momentum dispersion relation in Fig. 3.10(a) at $\nu = 2/5$ clearly shows the anticrossings of the cavity mode

⁴The few isolated bright spots are artifacts induced by cosmic rays exciting pixels the CCD camera.

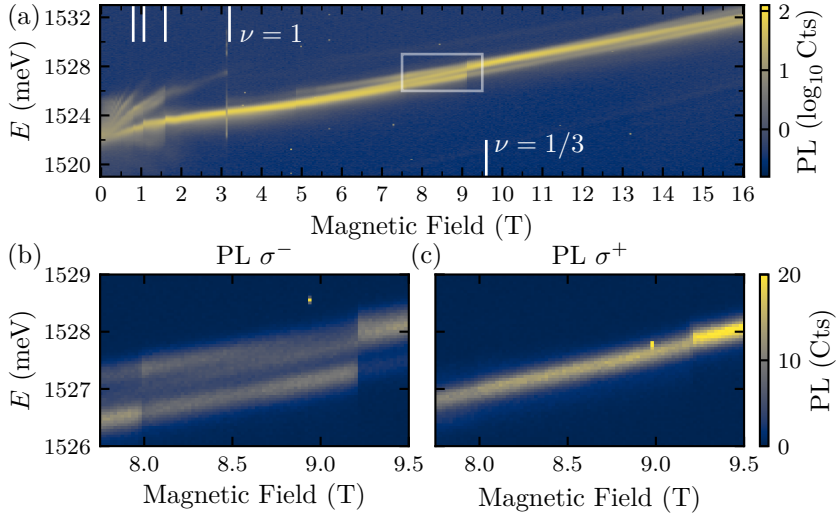


Figure 3.9: Emission from sample B* without cavity in the FQH regime and feature of electronic incompressibility. (a) Overview of PL emission from 0 to 16 T, showing the Landau level fan at low fields and a discontinuity just above 9 T before entering $\nu = 1/3$ (white mark). (b,c) Zoom into the gray box in (a), featuring the discontinuity for (b) σ^- and (c) σ^+ polarized detection.

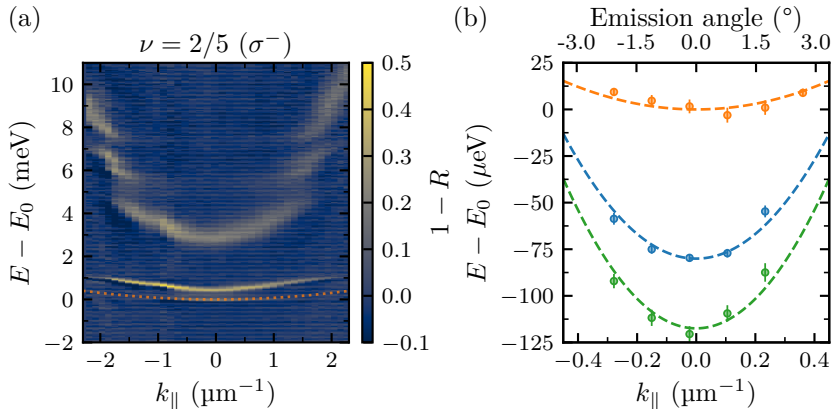


Figure 3.10: Polaron-polariton energy-momentum dispersion around $\nu = 2/5$. (a) Cavity spectroscopy at $\nu = 0.4$ for different in-plane momenta k_{\parallel} (σ^- polarization). The energies are plotted relative to E_0 , the energy of the $k = 0 \mu\text{m}^{-1}$ lowest polariton at $\nu = 2/5$. The flat reflection signal observable between the lower and upper polaritons around $k = 0 \mu\text{m}^{-1}$ is an experimental artifact, stemming from an etalon effect in the detection path. (b) Fitted energy of the lower polaron-polariton for small k_{\parallel} at filling factor $\nu = 0.42$ (green), $\nu = 0.4$ (orange) and $\nu = 0.37$ (blue). The error bars are statistical errors from Lorentzian fits of the lower polariton line. Dashed lines show parabolic fits to the lower polariton energies.

with the heavy hole polarons X_{attr} and X_{rep} . But in contrast to Fig. 2.13(a), the cavity energy is tuned through its parabolic dispersion instead of the cavity length being varied as previously.

We extract the peaks of the (faintly visible) lower polariton dispersion at $\nu = 2/5$ from the measured spectra and plot their energies in Fig. 3.10(b). We fit a parabola (dashed orange line) to the LP energies and compare it to the energy-momentum dispersions at filling factors slightly above (green) and below (blue) $\nu = 2/5$ extracted by the same procedure. Here, the energy is referenced to the bottom of the orange parabola, while the x -axis shows a smaller range of in-plane momenta compared to the left panel. Strikingly, we find an increase of the effective mass m^* at $\nu = 2/5$ (orange) by a factor of 4 ± 2 compared to $\nu = 0.42$ (green) and $\nu = 0.37$ (blue). A precise estimation of the lower polariton mass at $\nu = 2/5$ is rendered difficult due to the low curvature of the parabola, its absolute value extracted from the fit is

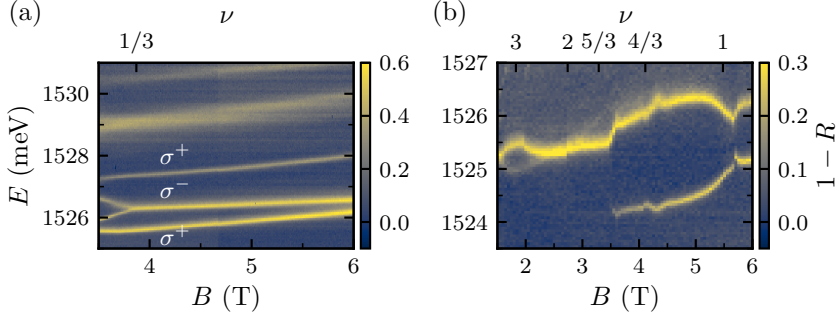


Figure 3.11: FQH regime below $\nu = 1/3$ and beyond $\nu = 1$. White light cavity spectroscopy. (a) Small fillings $\nu \leq 1/3$ in sample A and (b) fractional states in the second LL $\nu > 1$ for sample B.

$m^* = 5 \times 10^{-4} m_e$. This observation further illustrates the strong reduction in oscillator strength of the attractive-polaron resonance which reduces the cavity-character and enhances m^* .

3.3.3 High Field and Density Limits

We trace the evolution of the polariton response at very small fillings in Fig. 3.11(a) for sample A, a continuation of Fig. 3.7(c). At and below $\nu = 1/3$, we observe full spin-polarization of the 2DES when all electrons occupy the same spin state and the polariton gap completely vanishes in σ^- polarization. Therefore, the singlet-polaron resonance in this polarization loses its oscillator strength. The σ^- mode below $\nu = 1/3$ is still a polariton albeit mostly photon-like. It shows strong but detuned coupling to higher-energy polaron excitations. Unfortunately, no further structure is visible at fractions below $\nu = 1/3$ in this measurement neither are signatures of Wigner crystallization [174–177] visible, which might occur at very small fillings [178]. They do display optical signatures, at least for the case of transition metal dichalcogenide monolayers [179].

Figure 3.11(b) displays FQH states in the second Landau level, namely spectral features in WL close to fillings $\nu = 4/3$ and $\nu = 5/3$. While we have not yet studied these states in detail, it is interesting to note that they are indeed optically accessible. In a next generation of experiments, more

exotic FQH states could be addressed with cavity spectroscopy, for example the $\nu = 5/2$ state [180–183].

3.3.4 Optical Power Dependent Effects

Optical studies of 2DES generally require the use of low optical power ≤ 1 pW due to the sensitivity of the electron density n_e to illumination. When increasing the optical power, significant changes in the position and shape of the spectral features associated with the quantum Hall effect have been observed [96]. This is a major limitation for applications that require precise knowledge of the filling factor, or equivalently of the electron density. Furthermore, when studying ground state properties of the 2DES, care must be taken not to perturb the system under study away from this ground state with the experimental probe. These considerations motivate our sample design presented in Section 2.4. In this section, we demonstrate the robustness of our device (sample A) to optical power, which constitutes a major improvement over previous devices. Furthermore, we highlight remaining challenges presented by slowly varying changes in n_e and incoherent emission and how they were avoided in our experiments. We base this analysis mostly on the $\nu = 1$ state and continue to discuss those measurements of the spin polarization that are still affected by illumination even for an optimized sample.

We test the robustness of n_e against applied optical power by measuring reflectivity spectra around $\nu = 1$ for total incident optical powers ranging from a few pW to a few hundred nW. We use CW white light, where the total power is spectrally distributed across approx. 45 meV. We chose to work with $\nu = 1$ because it provides a clear optical signature that can be used to track the filling factor. Figure 3.12 shows these spectra obtained using σ^- -polarized light, with the panels arranged in increasing incident optical power. We observe that the position of the main spectral signature, namely the symmetric decrease of the polariton splitting on both sides of $\nu = 1$ leading to an extended plateau with reduced splitting around $\nu = 1$, remains very stable as we increase the optical power. Specifically, the variation of magnetic field where the plateau occurs suggest relative variations in n_e below 1%—while previous devices exhibit variations by tens of percent. We refer to the Supplementary material in [106] and previous works [19, 96]

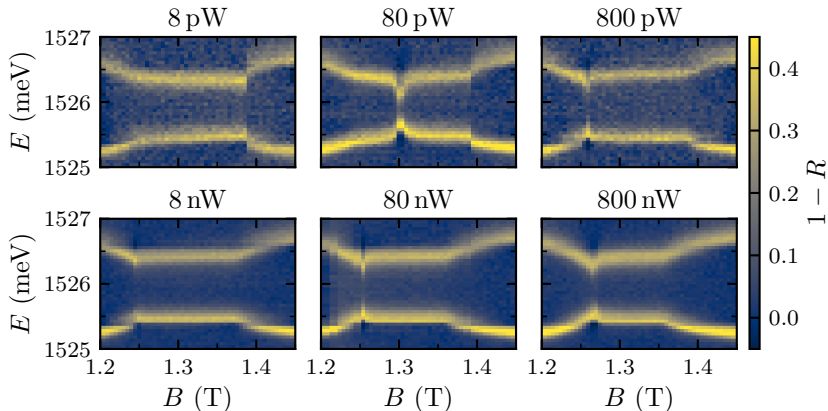


Figure 3.12: Light sensitivity of sample A, investigated at the $\nu = 1$ plateau. The panels show white light reflectivity spectra recorded for increasing values of the optical power. We used, in this case, σ^- -polarized light and we varied the magnetic field from 1.2 T to 1.45 T i.e. around filling factor $\nu = 1$.

for further comparisons. We remark that the changes in n_e observed in Fig. 3.12 occur over the timescale of seconds after starting CW illumination and display hysteretic behavior as function of optical power. Depending on the sample, the strength of this effect varies. Occasionally, we encountered a small magnetic field dependence of light sensitivity by noticing that the magnetic field to filling factor conversion is not perfectly described by $B \propto 1/\nu$.

We observe, in Fig. 3.12, the presence of a sharp spectral feature particularly prominent for an optical power of 80 pW where the polariton branches almost touch. This feature of unknown origin, shows residual light sensitivity as it moves from one edge to the other edge of the $\nu = 1$ plateau when increasing the optical power. This observation has been reproducible at different positions on the sample and for multiple cool-down cycles. A similar feature has been reported previously and identified as an indication of the presence of large scale skyrmions around a sharp region of full polarization at exactly $\nu = 1$, accompanied with fast depolarization on both sides [124]. Nonetheless, no mention of its power-dependence was made. To rule out the possibility of a power-dependence of n_e associated with this sharp feature,

3. Polaron-Polaritons in Integer and Fractional Quantum Hall States

we repeated the power-dependent measurements around $\nu = 2/5$. In that case, no sharp feature was identified and the optical feature associated with $\nu = 2/5$ in reflectivity spectra showed the same robustness of n_e against optical power (not shown). Therefore, based on our analysis, we conclude that the origin of the light-sensitivity of the sharp feature observed around $\nu = 1$ is distinct from an overall modification of n_e . Strong sensitivity of this feature to temperature was found [124], in agreement with inelastic light scattering experiments [184]. In the latter, it was argued that the ferromagnetic order persists but breaks down into domains above $T_Z = \mu_B g B / k_B$. More recent resistive nuclear magnetic resonance experiments [185] support the hypothesis that disorder stabilizes the QH Ferromagnet to some degree by limiting Skyrmion sizes. This is in line with our observation, hinting at a fragile QHF surrounded by a glassy phase of Skyrmions, limiting spin polarization. Note also that the hole gas sample C with lower mobility and stronger disorder displays perfect spin polarization over a larger parameter space. However, in our experiments in sample A, the electron density and thereby the magnetic field $B \approx 1.3$ T is lower than in most other studies. This reduces both Zeeman and cyclotron energy scales, which should lead to an increased susceptibility to temperature.

We conclude this chapter by pointing out another effect that may occur at any magnetic field and depends on the illumination conditions. We show an energy-momentum dispersion of sample A in Fig. 3.13(a) which, in contrast to most other measurements in this chapter, was acquired using a free space optical setup to allow further resolution of k_{\parallel} . The vertical stripes (brightness oscillations) are interference fringes due to the imaging system. Red dashed circles highlight an anomalous emission present even for resonant white light excitation. A similar feature was observed in sample C, visible as bright yellow feature in Fig. 3.13(b). The anomalous emission line is pinned in energy below the attractive polaron asymptote but does not follow its blueshift due to phase space filling. Since the feature is present at 0 T, we attribute it to localized trion-like emission, most likely bound to ionized Si⁺ donor sites or possibly other impurity states.

For the experiments presented in this and other chapters, we tried to circumvent these power and illumination dependent effects. The incoherent emission is prevented by restricting the excitation source in either power, energy or in-plane momentum (or a combination thereof). We found that

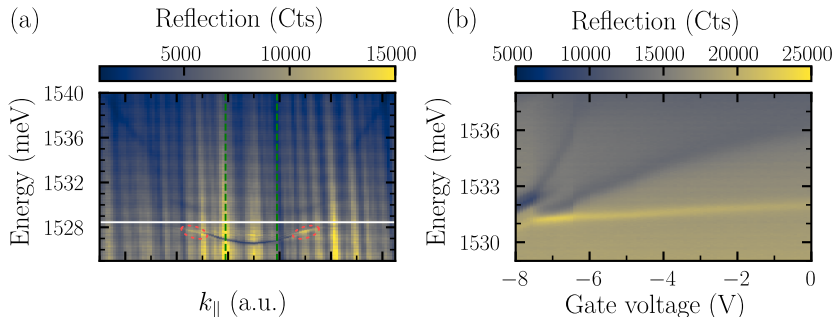


Figure 3.13: Features of incoherent emission due to excitation with higher power ($\sim 10 \mu\text{W}$) and high energy (NA) white light. (a) Dispersion measurement on sample A with emission features encircled in red at the outermost edge of the LP branch. The white line marks the attractive polaron asymptote. (b) Gate scan on sample C, as in Fig. 2.6 (without optical cavity). Note the emission line visible in bright yellow, starting at 1531 meV.

restricting the NA to within the green-dashed lines or blocking all excitation energies above the white line in Fig. 3.13(a) removes this artifact. This condition is satisfied for all experiments in the fiber-based setup, due to the lower NA. From this we can conclude that population in the upper polaritons (the upper branches are slightly visible in dark blue in the dispersion Fig. 3.13(a)) feeds the emission line via incoherent relaxation processes. The remaining sensitivity of n_e is mitigated by working at constant and minimal optical powers. In Chapter 5, we use a time-resolved spectroscopy technique to probe the system at timescales much faster than the observed variations in n_e .

The filling factors indicated in our diagrams are designating regions rather than precise positions on the magnetic field axis. They are our best estimates based on the identification of LL absorption edges and spectral discontinuities. The macroscopic transport characterization of the electron densities of our devices are the starting point for these estimates but are often not accurate enough to convert B to ν for local optical experiments. The problem is exacerbated by local modifications of the electron density due to light illumination, which was discussed in detail in this section. While this problem has been mitigated by special sample design for resonant excitation, it remains

relevant for above band gap illumination. Finally, there is no a priori reason why optical signatures due to incompressibility of the 2DEG should always occur at center of Hall plateaus found in magneto-transport. In the work [169] for example, a discontinuity in emission was found aligned with the edge of a Hall plateau.

3.4 Conclusion and Perspectives

We demonstrate that cavity spectroscopy is a viable platform to probe integer and fractional quantum Hall states, extending the work by Smolka et al. [19]. Electron-exciton interactions lead to optical signatures of the electronic ground states. Polarization resolved spectroscopy allowed us extract electronic spin polarization. We applied this technique to study ferromagnetic order [109, 148] in the vicinity of the $\nu = 1$ state and to optically detect various integer and fractional quantum Hall states. Signatures for electronic incompressibility appear as discontinuities in the reflectivity and emission spectra.

We emphasize that theory of exciton-polarons has been previously developed for excitons interacting with a 2DES in the limit $B = 0$ [21, 72]. A quantitative modeling of our experiment requires extending prior theoretical work to the case of screening of excitons by electrons occupying a single LL: a significant advance in this direction was the recent development of the theory of exciton-polarons in the limit of strong magnetic fields but without taking into account electron-electron interactions leading to FQH states [84]. Our work focused on the singlet channel which plays a prominent role in the limit of moderate magnetic fields ($B \leq 3.5$ T) used in our experiments. A more challenging problem is exciton-electron interactions in the vicinity of FQH states: polaron-polariton formation in this limit may be described using polariton dressing by fractionally charged quasi-particle-hole pairs [23]. The latter problem is related to identification of signatures of incompressibility of the many-body ground state in the polariton excitation spectrum.

Our experiments focused on the lowest energy polariton. The upper polaritons show a more complex structure that we attribute to coupling to higher available LLs as we tune B , see for example Figs. 3.4 and 3.7(c). Although subject to additional line broadening due to its spectral overlap

with material resonances, the UP contains richer structures that have not been analyzed yet. On the same note, it could be interesting to move E_{cav} into resonance with LLs $n \geq 1$ to study how their optical excitations are modified by coupling to quantum Hall states and whether the triplet trion channel plays a role in the polariton spectrum in high magnetic fields. On the technical side, increasing the quality factor of the cavity could further enhance the sensitivity of our measurements. Steps in this direction have been taken in similar MBE-grown exciton-polariton structures [112] by optimizing the growth conditions for the DBR mirrors. An alternative route consists of replacing the DBR mirrors with higher quality dielectric mirror coatings.

We note that injecting σ^- polaritons may introduce (optically excited) electrons into the partially filled LL0 and thereby increases ν . Given that the polariton splitting depends on ν , this observation suggests that the system will exhibit a novel form of optical nonlinearity that depends strongly on ν . This constitutes a motivation for our nonlinear optical experiments in Chapter 5. An inspiring long-term goal is to enable optical manipulation of anyon quasi-particles associated with strongly-correlated phases [22]. Many challenges remain, in particular the short length scales and coherence lengths associated with these quasiparticles. Recent breakthroughs in the detection of quasi-particle braiding statistics lend optimism [186, 187].

Transport of Polaritons with External Electric and Magnetic Fields

Photons cannot be directly manipulated with electric and magnetic fields because they do not carry charge. Hybridization of photons with electronic polarization to form exciton-polaritons allows exploiting the excitonic response to external fields. However, the neutral bosonic nature of these quasi-particles still limits their response to external gauge fields. In this chapter¹, we demonstrate polariton acceleration by external electric and magnetic fields in the presence of non-perturbative coupling between polaritons and itinerant electrons. We identify the generation of electron density gradients by the applied fields to be primarily responsible for inducing a gradient in polariton energy, which in turn leads to acceleration along a direction determined by the applied fields. Additionally, we observe different circular polarization components of the polaritons being accelerated in opposite directions when the electrons are close to the $\nu = 1$ integer quantum Hall state.

¹The experiments that constitute this chapter were published in the article [188], with corresponding experimental data available in the ETH Research Collection [189]. This work was carried out together with Dr. Thibault Chervy. We both contributed equally.

4. Transport of Polaritons with External Electric and Magnetic Fields

Controlling photons with external electric or magnetic fields is an outstanding goal. On the one hand, coupling photons to artificial gauge fields holds promises for the realization of topological and strongly correlated phases of light [9, 28, 190, 191]. On the other hand, effecting forces on photons constitutes both a problem of fundamental interest in electromagnetism and an important step in view of technological applications [17, 18, 192, 193]. One promising avenue towards this goal is to hybridize photons with material excitations that are genuinely sensitive to gauge fields [194]. In this non-perturbative regime, exciton-polariton states are formed, ensuring that the forces acting on the material excitations are directly imprinted onto the photon. However, the neutral bosonic nature of polaritons has so far severely limited their response to gauge fields [195–198].

A particularly appealing approach to circumvent this limitation is to leverage on the interaction between excitons and free charge carriers. Indeed, early reports on the drift of trions in an electric field [199, 200], as well as on the Coulomb drag effect in bilayer systems [201–204] indicated that it may be possible to manipulate neutral excitations using electric fields in a solid-state setting. Recently, experimental [205] and theoretical studies [206] reported the electrical control of the speed of a polariton superfluid, raising new questions and possibilities regarding the interplay between the normal and condensed fractions of the fluid in the presence of electron-exciton interactions.

Upon decreasing the electron density, the quasi-particle weight of the repulsive polaron branch, quantifying its excitonic character, increases. In the limit of vanishing electron density, the repulsive (attractive) polaron asymptotically becomes the bare exciton (molecular trion) state with strong (vanishing) coupling to the cavity mode [21]. The many-body polaronic states are expected to be charge neutral [21, 80], suggesting the absence of coupling to external fields. In a recent theoretical study however, it was shown that neutral polarons are sensitive to the average force on electrons, leading to a finite polaron trans-conductivity in the non-equilibrium limit—an effect that should be observable even when polarons hybridize with cavity photons [207].

In the following sections, we demonstrate experimentally that external electric and magnetic fields effect forces on polaron-polaritons. In contrast to

earlier proposals, we find that the observed polariton acceleration primarily originates from a source-drain voltage induced density gradient in the two-dimensional electron gas in which polaritons are immersed. We show that the direction of the resulting force can be changed by an externally applied magnetic field, since the induced Hall voltage creates transverse density gradients. Finally, we extend this approach to demonstrate spin-selective acceleration of polaritons when the 2DEG is in the integer quantum Hall regime.

4.1 Experimental Methods and Sample Characterization

4.1.1 Polariton Hall Bar

In the following, we describe our approach to design a device with the aim to study the interplay between electronic and polariton transport. In order to have a well-defined overlap between polariton and current density, we patterned a Hall bar with width on the order of $100\ \mu\text{m}$ suitable for optical experiments. Furthermore, we maintained the planar, 2D geometry of the cavity which preserves in-plane momentum conservation and allows to measure the in-plane motion of polaritons in response to external fields. Thereby, either a relative shift in polariton dispersion relation or an accumulation of in-plane momentum could be detected. Conversely, polaritons can be excited in particular directions inside the Hall bar with well-defined in-plane momentum and a change in electrical current could be measured.

Starting from the structure introduced in Section 2.4, samples were etched in the form of a Hall bar with annealed electrical contacts to the 2DEG, as depicted in Fig. 4.1. A recipe listing the essential fabrication steps, performed in a cleanroom environment, can be found in Table 4.1. To establish contacts that display close to ohmic behavior with low contact resistance, the top mirrors have been etched allowing to place the metal contacts closer to the 2DEG. Figure 4.1(a) shows a schematic side-view of the structure and contacting process. A few $\lambda/4$ layers of the top mirror were kept, to avoid exposing the quantum wells to the surface which can lead to loss of carriers. Next, the Hall bar geometry is defined by etching to below the QW layers outside the Hall bar region, leading the structure shown in Figs. 4.1(b)

4. Transport of Polaritons with External Electric and Magnetic Fields

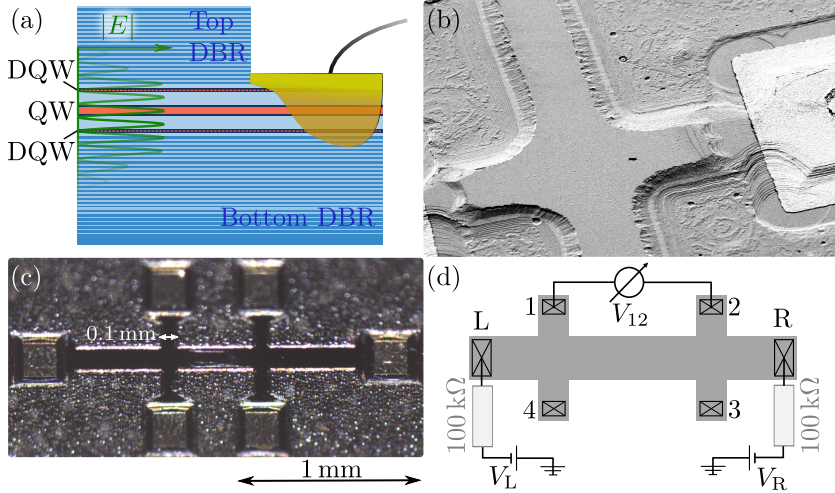


Figure 4.1: Polariton Hall bar device structure and electrical contacts. (a) Side-view. The top mirror has been removed by wet etching to contact the 2DEG located in the center QW. DQW, doping quantum well. (b) SEM image showing a junction of the Hall bar and the exposed layers of the Bragg reflector on the etched surface. (c) Photograph of a processed device. (d) Schematic corresponding to (c) indicating the electrical wiring and introducing labels for the contacts.

and 4.1(c). Finally, aluminum wire-bonds establish the electrical connections to the chip carrier. The device is mounted in a dilution refrigerator which is cooled to its base temperature of about 20 mK where the wires pass a second-order low-pass filter to the grounded mixing chamber plate for thermalization and noise rejection. The exact electron temperature is difficult to assess experimentally, but we can give an estimate based on a temperature measurement performed previously with a similar experimental setup in the same dilution refrigerator. It is based on measuring the thermal occupation of electrons in a quantum dot [208]. The temperature of the Fermionic reservoir was found to be about 100 mK.

²Gallium was used for mounting the wafer on the MBE sample holder and is removed to avoid contamination of other cleanroom equipment.

³Micro resist technology ma-N 1400.

⁴MicroChemicals HDMS.

Step	Parameters
Cleave sample to conveniently sized chip	4 mm to 8 mm
Clean and dehydration bake	120 s at 120 °C
Protect surface with photoresist (PR)	
Remove excess gallium ² from backside	HCl:H ₂ O 1:1 for 25 min
Remove PR and clean	Acetone
Coat PR, pattern contact geometry	
Binary etching of top DBR	Recipe Table 2.1
Remove PR and clean	Acetone for 30 min at 50 °C
Coat PR, pattern contact geometry	
Metal deposition Ge/Au/Ge/Au/Ni/Au	53/207/53/107/80/100 nm
Lift-off and clean	Acetone for 30 min at 50 °C
Annealing	30 s at 500 °C
Coat PR, pattern Hall bar geometry	
Hall bar etching in H ₂ SO ₄ /H ₂ O ₂ /H ₂ O	3:3:100 for 15 min ~7 μm
Remove PR and clean	
Mount in chip carrier, bond wires	

Table 4.1: List of process steps to pattern the polariton Hall bar device. A negative tone photoresist³ was used before applying an adhesion promoter⁴. Clean means placing sequentially in acetone, isopropanol, H₂O and blow drying with N₂, optionally oxygen plasma treatment.

4.1.2 Electrical Transport Properties

We characterize the electrical properties of the sample by a four-point current-voltage (I-V) measurement yielding the characteristic shown in Fig. 4.2(a). At low source-drain bias applied between terminals R (source) and L (drain), the I-V curve is linear with a 2DEG resistivity of $210 \Omega/\text{sq}$. Increasing the source-drain bias to about $\pm 1 \text{ V}$, the I-V curve becomes nonlinear, moving away from electrostatic equilibrium. In this regime, the externally applied electro-chemical potential (i.e. the voltage applied to the leads) creates a spatially varying chemical potential in the 2DEG. At even larger source-drain bias, the 2DEG is depleted and we recover a linear I-V characteristic with an increased resistivity of $1500 \Omega/\text{sq}$, corresponding to electrical conduction in parallel channels, the DQWs in particular. As sketched in Fig. 4.1(a) the annealing technique used to contact the 2DEG also contacts the lower mobility doping QWs. Our device thus corresponds to a field effect transistor where the gate potential, nominally defined by the donor impurities, can be modified by the source-drain bias leading to the pinch-off of the 2DEG [209], [210, Chapter 6].

We show, in Figs. 4.2(b) and 4.2(c), the longitudinal (measured via V_{12} , blue curve) and transverse (measured via V_{23} , orange curve) resistivities as a function of magnetic field in z -direction, perpendicular to the 2DEG. They were recorded using two lock-in amplifiers⁵ with excitation current of 1 nA at a modulation frequency of 13.8 Hz . The excitation current was derived using a large resistance in series between the source contact and the oscillating source voltage from signal generator in the lock-in. We clearly identify Shubnikov–De Haas oscillations in the longitudinal resistivity and the onset of Hall plateaus in the transverse resistivity. Expected 2DEG filling factors are marked and match the minima of the longitudinal resistance oscillations. The existence of parallel conduction channels results in an overall trend in the resistivity curves that deviates from standard quantum Hall transport. This effect, well known in 2DEG transport [211–214], explains the lack of quantization in the transverse conductance and the rise observed in the longitudinal resistance minima as opposed to the expected behavior of minima extending to zero (compare to Fig. 2.5). The parallel conductance is a consequence of a trade-off in our device geometry between optimizing the optical

⁵Signal Recovery 7265 DSP Lock-in Amplifier.

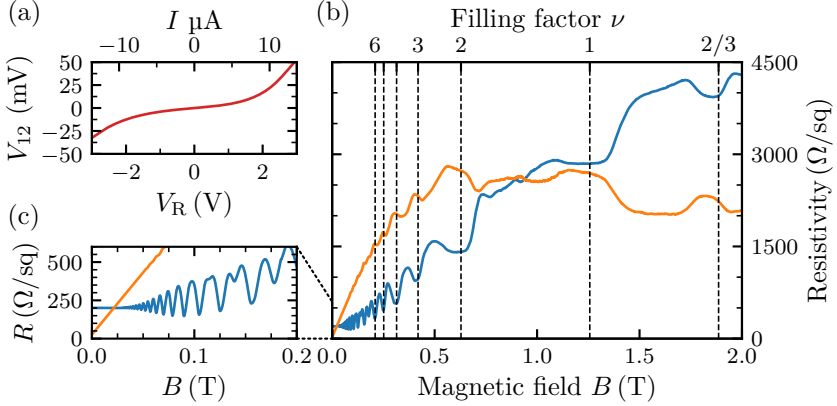


Figure 4.2: Electrical transport characteristics of the Hall bar device used in the following experiments. (a) IV-characteristic of the Hall bar device at zero magnetic field. (b) Magneto-transport measurement, showing the longitudinal (blue) and transverse (orange) resistivity versus magnetic field and Landau level filling factor. (c) Zoom into panel (b), focusing on the onset of Shubnikov–De Haas oscillations in the low magnetic field regime.

properties and retaining good transport characteristics. Another contributing factor to the overall increase of resistivity with magnetic field could be a lack of optimization of the contact geometry [215, Chapter 8], i.e. too little linear cross-sectional overlap between the 2DEG and the contacts.

4.1.3 Optical Imaging Setup

The following experiments were performed with a dilution refrigerator that allows for free space optical access to the sample surface through optical windows, in contrast to the optical fiber based system (we refer back to Section 2.3 for an overview). This optical access enables simultaneous position and momentum resolved microscopy. Figure 4.3(a) shows a more detailed schematic of the optical setup used in this study. The free space optics used for excitation, collection and imaging are mounted in a cage assembly that is attached to the bottom of the dilution refrigerator. Optical windows through the different shields of the cryostat offer optical access to the sample which is thermally anchored on the mixing chamber at a base temperature of 20 mK.

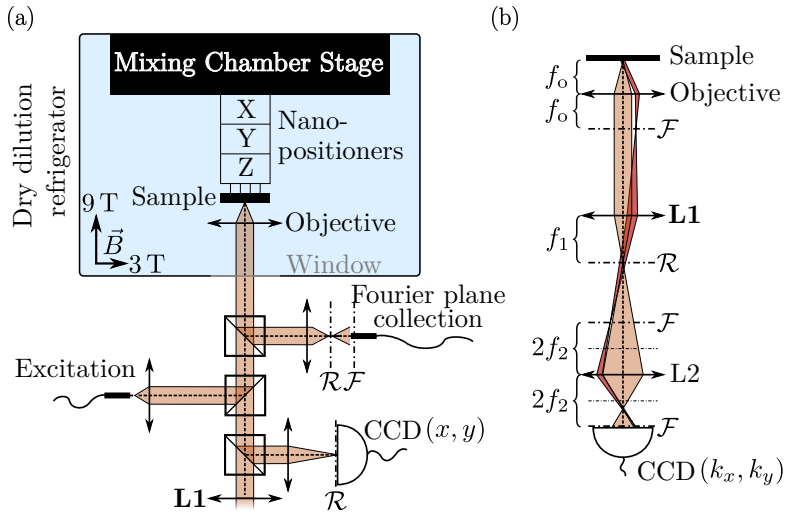


Figure 4.3: Schematic of the free space optical setup. (a) Upper part of the cage assembly showing the excitation and collection arms of the microscope attached to the dilution refrigerator and the real space imaging CCD camera. (b) Schematic ray tracing for Fourier space imaging. The intermediate real space image planes (\mathcal{R}) and Fourier space image planes (\mathcal{F}) are shown in black dashed lines.

A single cold, high numerical aperture $NA = 0.7$ objective lens⁶ allows for high resolution microscopy of the sample. The excitation light is delivered by a single mode optical fiber and is collimated and directed to the microscope objective lens. The light emitted or reflected by the sample is refracted by the same objective lens and is simultaneously imaged onto real space and Fourier space CCD cameras⁷ as well as on the facet of a single mode optical fiber conjugated with the back-focal plane of the microscope objective. This collection fiber is mounted on a motorized stage and can thereby be displaced in the back focal plane, i.e. along Δx in the schematic Fig. 2.9(b). This allows to collect light with angular resolution or well defined in-plane momentum k_{\parallel} . The light coupled into this fiber is brought to a spectrometer, allowing to record spectra at desired angles within the NA of the objective lens. Conversely, light can be sent via this collection fiber in order to excite polaritons with finite in-plane momentum. The motion of the polaritons in the xy -plane can then be tracked on a real-space imaging camera, with light leaking from the top mirror along the polariton trajectory. Alternatively, a camera positioned at a Fourier plane can be used to record the (k_x, k_y) dependence in one shot (schematic ray tracing is depicted in Fig. 4.3(b)). The excitation, detection and imaging arms are all equipped with linear polarizers⁸ and quarter-wave plates⁹. They allow controlling the incident and detected polarizations, and in particular enable us to measure in resonance fluorescence configuration where detection and excitation polarizations are chosen orthogonal. It is possible to achieve a suppression of incident laser light to the signal on the order of 10^4 . Due to the long distance between the sample and the bottom of the dilution refrigerator (about 50 cm), the optical setup is not fully conjugated and relies instead on an image forming lens L1 and a 2f optical relay lens L2. The resulting Fourier space resolution (point-spread function of the collection fiber) is $0.15 \mu\text{m}^{-1}$ at the center of the Fourier plane, and degrades to $0.3 \mu\text{m}^{-1}$ at large momenta due to optical aberrations of the imaging setup. At the inflection point of the lower polariton branch, this finite momentum resolution yields an energy broadening of $300 \mu\text{eV}$ which is significantly larger than the polariton linewidth expected

⁶Thorlabs Aspheric Lens 354330-B.

⁷FLIR CM3-U3-13S2M-CS.

⁸Thorlabs LPVIS050.

⁹Thorlabs WPQ05M-808.

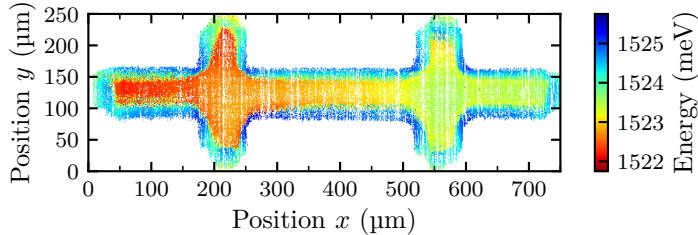


Figure 4.4: Map of the lower polariton PL emission energy measured close to normal incidence $k_{\parallel} = 0$ as function of position x, y . The gradient along the x -axis stems from the radial thickness gradient of the wafer. The experiments in this chapter are based on this Hall bar, fabricated on a chip of sample A.

from the finite cavity lifetime. At $k_{\parallel} = 0$, the polariton dispersion is flat and a conservative estimate for the energy resolution of our imaging setup based on the polariton group velocity at $\pm 0.15 \mu\text{m}^{-1}$ yields $30 \mu\text{eV}$, which is well below the $100 \mu\text{eV}$ resolution of our spectrometer. In order to account for the spectral shape of the white light source, the dispersion spectra throughout this chapter are corrected by the following procedure. First a numerical low-pass filter is applied to remove spectral etaloning fringes at high spatial frequency. The slowly varying spectral shape of the white light is then extracted using the fact that the polariton signal disperses as a function of some tuning parameter (position, momentum or magnetic field), while the lamp spectral shape remains relatively constant. By sorting the individual spectra along this tuning parameter axis we can extract the spectral shape of the source and use it to normalize the reflection spectra, as previously.

4.1.4 Cavity Wedge and Polarization Eigenbasis

A photo-luminescence (PL) scan map of the sample is shown in Fig. 4.4 outlining the shape of the Hall bar. It has been acquired by scanning the (x, y) positions of the sample and collecting with the Fourier space fiber tip moved close to $k_{\parallel} = 0$ (normal incidence). Emission spectra at each position were fitted to find the lower polariton peak energy. This peak energy is displayed in the colormap. The increase in emission energy of about 3 meV/mm from left to right is due to a wedge in the cavity length introduced during sample

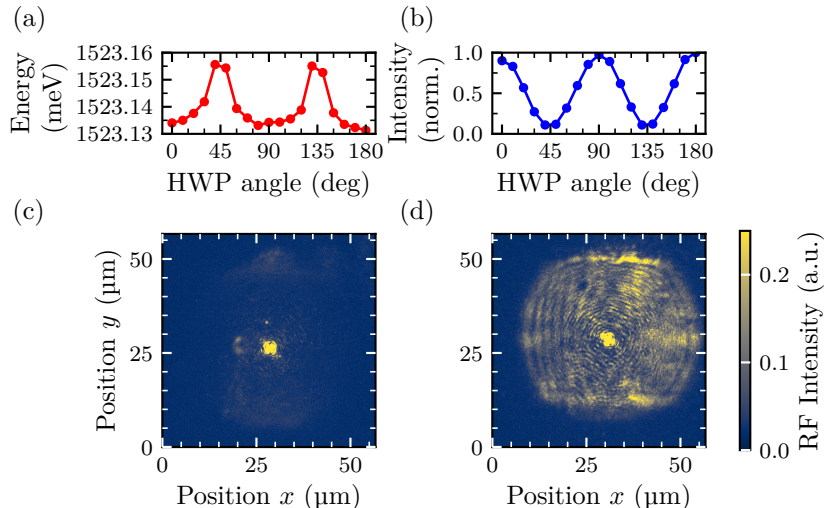


Figure 4.5: Linear polarization eigenbasis presumably defined by mechanical strain in the polariton Hall bar device. Lower polariton photoluminescence peak energy (a) and intensity (b) as function of linear polarization angle, controlled by a half-wave plate (HWP). (c,d) Real-space images measured in cross-linear polarization at (c) 0° and (d) 45° with respect to the Hall bar x -axis. These measurements were obtained in the absence of any source-drain bias and at $B = 0$.

growth.

In this paragraph, we discuss the optical polarization properties of our sample and how they were used to obtain measurements in resonance fluorescence (RF) configuration. In a first experiment, we excited the system non-resonantly at 632 nm and measured the $k_{\parallel} = 0$ lower polariton photoluminescence center energy (Fig. 4.5(a)) and intensity (Fig. 4.5(b)) as a function of polarization angle for a fixed position (x, y) . A half-wave plate (HWP) in front of a horizontal polarizer was used to rotate the detection angle, so that orthogonal polarizations are separated by 45° rotations of the HWP). We observe an energy splitting of $\Delta_{xy} = 20 \mu\text{eV}$ between the linear polarization eigenstates pointing along the crystalline axes of our sample. These axes also align with the long and short edges of the Hall bar and thereby the x - and y -axes used throughout this chapter. Excited carriers form exciton-polaritons and relax towards the LP $k_{\parallel} = 0$ state through scattering with

phonons, electrons and other polaritons. This explains the reduced intensity in the higher energy eigenstate. We did not resolve such an energy splitting in an unprocessed device, from which we deduce that it originates from the patterning by etching. A second experiment was performed in order to verify that this birefringence still dominates compared to the TE-TM mode splitting [216] at excitation angles relevant to our experiments. Resonant CW excitation was set to focus in real space to excite polaritons at finite $|k_{\parallel}|$. In Fig. 4.5(c), polaritons are excited with polarization along x and detected along y which should be compared to Fig. 4.5(d), where polaritons are excited at 45° and detected at -45° to the x -axis. Displayed are real space images with the recorded intensity color-coded, plotted as function of positions (x, y) . The excited polaritons are traveling radially outwards due to their initial in-plane momentum. The bright, saturated center spot marks the excitation and is due to a part of the reflected laser beam that penetrates the detection polarizer. The fact that the emission from the polariton cloud is still well suppressed in the field of view shown in Fig. 4.5(c) demonstrates that the eigenbasis is aligned with the x and y axes, at least up to relevant in-plane momenta of $|k_{\parallel}| \leq 2 \mu\text{m}^{-1}$.

4.2 Polariton Transport by Electric Fields

4.2.1 Electron Density Gradients

The different regimes of the 2DEG transport behavior discussed in Section 4.1.2 above have their counterpart in the optical response of the system which we will discuss here. The following measurements show the reflectivity contrast, resolved either in real or Fourier space using broadband, white-light excitation. The sample is wired according to the drawing in Fig. 4.1(d), with $100 \text{ k}\Omega$ series resistors on contacts L and R and while the remaining contacts are floating. For the remainder of this chapter, we denote with V_L a voltage applied to the left (L) side of the Hall bar against the right (R) contact kept grounded. Analogously, V_R denotes a voltage applied to the right (R) contact against the left (L) side kept at ground level. Figure 4.6(a) shows the energy-momentum dispersion relation of the polaron-polariton states at zero source-drain bias. It shows normalized white light reflectivity data, recorded using the scanning fiber tip in Fourier space. We identify four branches re-

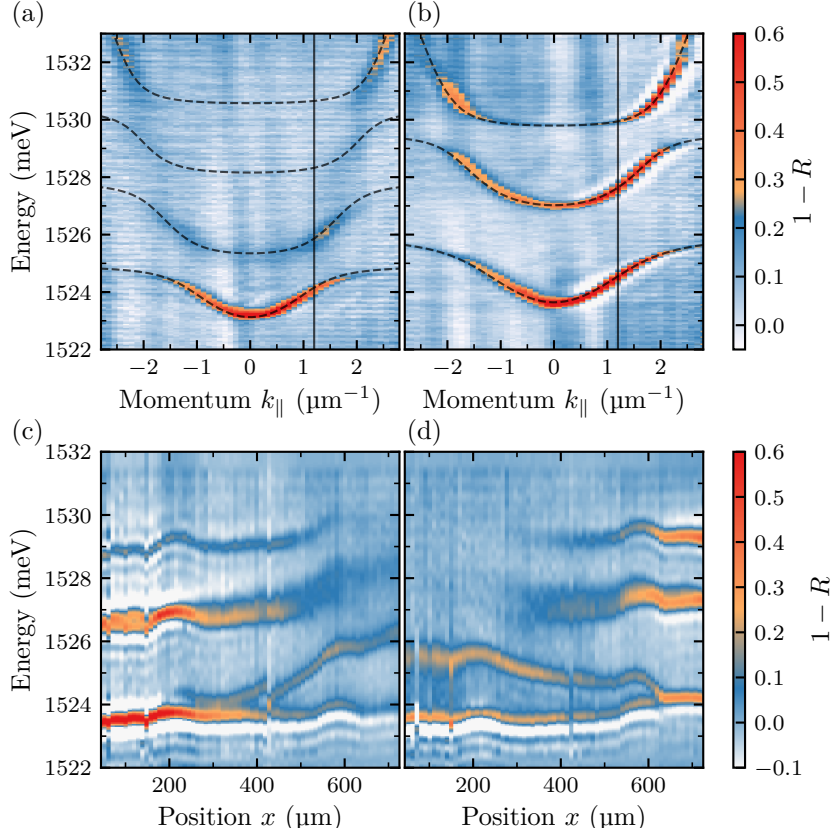


Figure 4.6: Electrically controlled polariton landscape via density gradients. (a) Normalized white-light reflectivity spectra showing the polaron-polariton energy-momentum dispersion at the nominal electron density. (b) Exciton-polariton dispersion in the depleted regime ($V_L = -6$ V). Dashed lines are coupled oscillator fits to the data. (c,d) Normalized white-light reflectivity spectra at $k_{\parallel} = 1.2 \mu\text{m}^{-1}$ (vertical line in (a,b)) as a function of position with a negative bias voltage applied to the left contact ($V_L = -2.4$ V) (c) and to the right contact ($V_R = -2.4$ V) (d).

4. Transport of Polaritons with External Electric and Magnetic Fields

sulting from the hybridization of the cavity photon with the attractive and repulsive heavy-hole polarons and with the light-hole resonance. The 2DES is at its nominal density. The opposite limiting case is displayed in Fig. 4.6(b), which shows the dispersion measurement performed while applying a very large bias of $V_L = -6$ V. There, we measure a typical exciton-polariton dispersion of an intrinsic QW with anticrossings about the heavy hole and light hole exciton energies, as expected from the 2DEG depletion already suggested by the I-V characteristic.

The polariton energy dispersions are well reproduced by coupled oscillator fits [8, 9] involving four states representing the cavity, attractive polaron, repulsive polaron and light hole exciton

$$H_{2\text{DEG}} = \begin{pmatrix} E_{\text{cav}} & \Omega_{\text{attr}} & \Omega_{\text{rep}} & \Omega_{\text{lh}} \\ \Omega_{\text{attr}} & E_{\text{attr}} & 0 & 0 \\ \Omega_{\text{rep}} & 0 & E_{\text{rep}} & 0 \\ \Omega_{\text{lh}} & 0 & 0 & E_{\text{lh}} \end{pmatrix} \quad (4.1)$$

with couplings Ω_j only between the cavity mode and each material resonance. In principle, we expect the light hole exciton to split into attractive and repulsive branches as well. But the measurements of Fig. 4.6 do not resolve this feature and therefore we did not introduce additional fit parameters for the light hole polarons. For the depleted 2DES, it suffices to take into account three states

$$H_{\text{QW}} = \begin{pmatrix} E_{\text{cav}} & \Omega_{\text{hh}} & \Omega_{\text{lh}} \\ \Omega_{\text{hh}} & E_{\text{hh}} & 0 \\ \Omega_{\text{lh}} & 0 & E_{\text{lh}} \end{pmatrix}, \quad (4.2)$$

cavity, heavy hole and light hole excitons. The cavity dispersion can be approximated by a parabola close to $k_{\parallel} = 0$ (Eq. (2.6)). The results are shown as dashed lines in Figs. 4.6(a) and 4.6(b) with the corresponding best least-squares fits listed in Table 4.2. The table summarizes the two cases of nominal density $H_{2\text{DEG}}$ (left panel Fig. 4.5(a)) and depleted H_{QW} (right panel Fig. 4.5(b)).

In between these two extremes of nominal electron density and full depletion, at intermediate bias voltages, the electron density shows smooth spatial gradients across the Hall bar as demonstrated in Fig. 4.6(c) for $V_L = -2.4$ V.

Parameter	Nominal density	Depleted QW
$E_{\text{cav}}(k_{\parallel} = 0)$	1524.04 meV	1524.96 meV
n_{cav}	3.21	3.32
E_{hh}	-	1525.96 meV
E_{attr}	1524.92 meV	-
E_{rep}	1527.86 meV	-
Ω_{hh}	-	1.63 meV
Ω_{attr}	0.94 meV	-
Ω_{rep}	1.13 meV	-
E_{lh}	1530.38 meV	1529.53 meV
Ω_{lh}	1.07 meV	1.04 meV

Table 4.2: Least-squares curve-fitting results of the coupled oscillator models Eqs. (4.1) and (4.2) to the polariton energy-momentum dispersions in Figs. 4.6(a) and 4.6(b) respectively.

Here, the polariton spectrum is recorded at positions across the long axis (x) of the Hall bar. The y position is kept centered and the collection angle is also fixed, corresponding to $k_{\parallel} = 1.2 \mu\text{m}^{-1}$. This particular choice for the in-plane momentum is not essential, but leads to a favorable cavity to attractive polaron detuning which highlights the two lowest polariton branches. On the left side, where the negative bias is applied, the sample is devoid of electrons and the spectrum resembles a vertical cut in the dispersion of Fig. 4.6(b) at $k_{\parallel} = 1.2 \mu\text{m}^{-1}$. Moving to the right, the electron density increases and we gradually recover polaron-polariton spectra corresponding to the dispersion of Fig. 4.6(a) as the oscillator strength is transferred from the excitonic to the polaronic resonances. Reversing the applied electric field ($V_{\text{R}} = -2.4 \text{ V}$) inverts this density gradient, as shown in Fig. 4.6(d). Such electron density gradients constitute electrically tunable potential landscapes for polaritons which we utilize in the following to transport neutral optical excitations. We note two imperfections where the polariton energies bend upwards at $220 \mu\text{m}$ and $570 \mu\text{m}$ which most likely originate from strain induced by the contact crossing regions. There is also an indication of this effect visible in a distortion of the LP emission energies, shown in the map Fig. 4.4. We find that

the polaritons experience an energy shift in this region also in the absence of source-drain bias but cannot rule out that a non-homogeneous current distribution adds to this effect at finite bias. Finally, we note a slight asymmetry in the dispersion between inflection $+k_{\parallel} \mapsto -k_{\parallel}$ which could have a contribution from finite misalignment of the optics, but note that the sample already breaks reflection symmetry because of the cavity thickness gradient.

We provide additional data from two other devices to further substantiate our ability to shape the polariton potential landscape with applied electric fields. In Fig. 4.7(a), white light reflectivity spectra (low $|k_{\parallel}|$) are shown as function of position along sample C. The gate voltage is kept fixed at -9.5 V but due to finite resistance of the gate, the electric field drops laterally and leads to a hole density gradient. This gradient manifests optically by splitting the lower polariton in two branches as an attractive polaron resonance occurs, moving towards the right. The feature is not as clearly resolved as in the measurements above due to higher sample temperature of about 300 mK during this experiment. White light reflection (not normalized, low $|k_{\parallel}|$) is shown in Fig. 4.7(b) for a Hall bar device fabricated from sample B. At fixed lateral position between two contacts, the source drain voltage is swept from -8 V to 8 V in steps of 1 V. The lower polariton resonance is continuously tuned by the source drain voltage. This demonstrates that shaping of the 2DEG density can be achieved reproducibly in these devices.

4.2.2 Polariton Acceleration

To demonstrate polariton transport, we resonantly excite a polariton cloud with a CW laser and image its expansion in two opposing electron density gradients. The excitation laser, at 1524.0 meV (813.54 nm), is linearly polarized and focused in the central region of the Hall bar ($x = 450$ μm), thus injecting a radially expanding cloud of polaritons with finite k_{\parallel} . The decaying polariton signal is recollected and separated from the scattered excitation beam by polarization filtering. A finite strain along the crystalline axes in the structure allows us to obtain this RF signal by polarizing the excitation beam at 45° with respect to the polarization eigenbasis (as evidenced in Section 4.1.4). Two real space images, I_{R} and I_{L} , of this RF signal are acquired under source-drain biases of $V_{\text{R}} = -2.4$ V and $V_{\text{L}} = -2.4$ V, respectively. These two voltages were chosen such that at the injection spot on the Hall

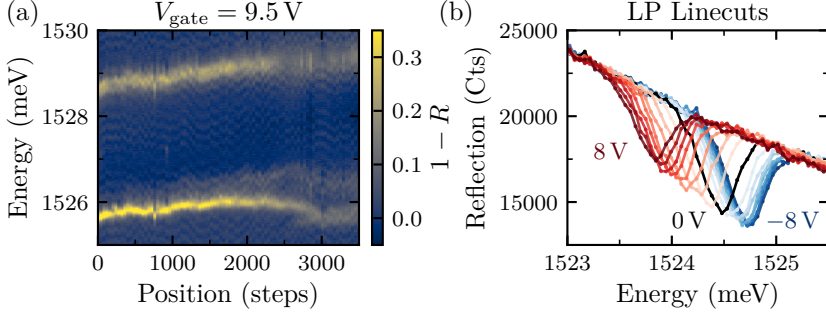


Figure 4.7: Additional evidence for voltage controlled polariton dispersion and electronic density gradients in other devices. (a) Normalized WL reflectivity as a function of position on a chip of sample C at fixed gate voltage. (b) Raw reflection signal from another Hall bar fabricated on sample B. Lower polariton signal as a function of source drain bias applied to two opposing Hall bar contacts.

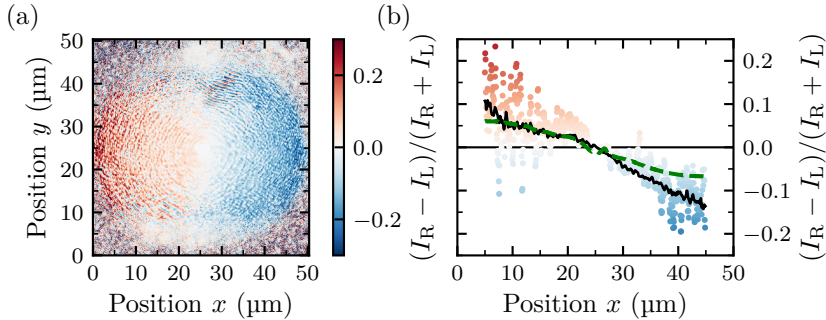


Figure 4.8: Polariton acceleration in density gradients on Hall bar device sample A. (a) Normalized difference between two RF images of polariton flow in opposing electron density gradients. (b) Comparison with a trajectory based model (dashed green line). The red-blue dots are a line-cut of panel (a) at $y = 25$ μm while the black line is an average of the experimental data between $y = 10$ and $y = 40$ μm .

bar, the electron densities are the same and the gradients are of opposite signs. This choice is not necessary but simplifies the observation of polariton acceleration as there is no trivial difference between dispersions and thereby group velocities between the two images to be compared. Such a difference in group velocities would result in additional differences between the emission intensities I_R and I_L . Tuning the experimental parameters into said regime removes the additional modeling and data processing steps necessary to deconvolve the trivial changes in group velocity from the desired left-right acceleration. Figure 4.8(a) shows the normalized difference $(I_R - I_L)/(I_R + I_L)$ of two such RF images, clearly demonstrating the ability to route polaritons by electrical means¹⁰. The polaritons are seeking the high electron density regions. Consider for example depletion on the right side (I_R) which traces to positive (red) values to the left of the excitation spot and negative (blue) values to the right of the excitation spot.

We chose to analyze the normalized difference of images because this quantity is independent of the excitation laser power. Taking just the difference of images without normalization leads to qualitatively the same features. Since the specular reflection of the laser beam is orders of magnitude stronger than the signal and the dynamic range of our detection is limited, a finite circular region of a few μm^2 in the center of the image $(x, y) = (25 \mu\text{m}, 25 \mu\text{m})$ remains saturated by the laser, which leads to a contrast of zero.

4.2.3 Coupled Oscillator Model

In order to understand the polariton acceleration effect, we characterize the local polariton dispersion. This will allow us to predict the changes in polariton group velocity and finally the expected shape of the polariton cloud subject to this dispersion. The goal is to calculate the emission intensity $I(x)$, for the two energy landscapes created by opposing density gradients. We proceed by measuring four dispersion relations, two at each side of the optical field of view at $x = 0$ and $x = 50 \mu\text{m}$ in Fig. 4.8(a) using the same voltage configurations as above $V_R = -2.4 \text{ V}$ and $V_L = -2.4 \text{ V}$. We repeat the coupled oscillator fits Eq. (4.1) for the four cases individually. Here, the

¹⁰We chose a new coordinate system (x, y) for a single field of view for this and the following images, instead of referring to the global coordinates as in Fig. 4.4.

electron density and therefore also the fit variables will take intermediate values between the limiting cases of nominal density and complete depletion.

We restrict ourselves to the one-dimensional case of propagation along the x -direction which should suffice for the experiments without magnetic field. We identify the cavity thickness variation and the electron density gradient as most important contributions to LP energy variations. By linearly interpolating across the optical field of view for each voltage configuration, we characterize the lower polariton energy landscape $E_{\text{LP}}(x, k_x)$, separately for the two density gradients used to measure I_{R} and I_{L} . Specifically, we suppose

$$\begin{pmatrix} E_{\text{cav}}(x, k_x) & \Omega_{\text{attr}}(x) & \Omega_{\text{rep}}(x) & \Omega_{\text{lh}}(x) \\ \Omega_{\text{attr}}(x) & E_{\text{attr}} & 0 & 0 \\ \Omega_{\text{rep}}(x) & 0 & E_{\text{rep}} & 0 \\ \Omega_{\text{lh}}(x) & 0 & 0 & E_{\text{lh}} \end{pmatrix} \quad (4.3)$$

where we keep the energies of the asymptotes fixed, namely the attractive polaron energy $E_{\text{attr}} = 1524.4 \text{ meV}$, the repulsive polaron energy $E_{\text{rep}} = 1525.9 \text{ meV}$ and the light hole exciton $E_{\text{lh}} = 1529.5 \text{ meV}$. This simplifies curve-fitting by reducing the number of free parameters and is justified by observing that the Rabi couplings Ω_j vary more strongly than the bare polaron energies as a function of electron density. Indeed, the coupling strength of the attractive polaron branch scales as the square root of the electron density, more precisely as $k_{\text{F}} a_{\text{T}}$ where k_{F} is the Fermi momentum and a_{T} is the trion Bohr radius [88]. The residual energy shift of the attractive polaron resonance is small due to a competition of the redshift from polaron formation and a blueshift from phase space filling. We accept a finite error from neglecting the repulsive polaron blueshift. In this approximation, the largest difference in acceleration induced by the electron density gradients to the polariton dispersion are expected to occur near the inflection point of the polariton dispersion, where the group velocity is most sensitive to variations in the Rabi coupling. Also entering the model is the bare cavity dispersion which we again approximate as a parabola $E_{\text{cav}}(x, k_x) = E_0(x) + \hbar^2 k_x^2 / (2m_{\text{cav}})$ with the effective mass of cavity photons $m_{\text{cav}} = E_0 n_{\text{cav}}^2 / c^2 \approx 3 \times 10^{-5} m_e$ measured independently. The cavity wedge in this region is 2.7 meV mm^{-1} and the cavity detuning Δ_{cav} is measured from $E_0 = 1524.2 \text{ meV}$ at $x = 0$. The results are displayed in Fig. 4.9(a) with full lines referring to bias applied

4. Transport of Polaritons with External Electric and Magnetic Fields

to the right and dashed lines to bias applied to the left contact. The Rabi couplings and cavity wedge have been interpolated linearly between the two measured points at $x = 0$ and $x = 50 \mu\text{m}$. The full and dashed lines cross at the center of the field of view. This confirms the choice of position and voltages to achieve the same electron density but gradients of opposite signs for the two configurations.

By diagonalizing Eq. (4.3), we extract the LP energy $E_{\text{LP}}(x, k_x)$ for right and left bias, which is color-coded in Figs. 4.9(b) and 4.9(c). Following the approach of previous work on polariton acceleration due to the cavity wedge alone [112], we write the classical Hamilton's equations of motion for the lower polariton

$$\frac{\partial x}{\partial t} = \frac{1}{\hbar} \frac{\partial E_{\text{LP}}}{\partial k_x} \quad \text{and} \quad \frac{\partial k_x}{\partial t} = -\frac{1}{\hbar} \frac{\partial E_{\text{LP}}}{\partial x}, \quad (4.4)$$

under which we propagate trajectories corresponding to the initial conditions of our experiment $x(t = 0) = 26 \mu\text{m}$ and $k_x(t = 0) = \pm 1.2 \mu\text{m}^{-1}$. These trajectories are shown as red lines for the two cases of bias voltages inside the lower polariton energy landscape. In order to predict the RF signal obtained in our experiment we consider two more ingredients. First, the polaritons decay while propagating with a lifetime of $\tau_{1/e} = \hbar/\Gamma_{\text{FWHM}} \approx 10 \text{ps}$. Second, to model the RF configuration we assume that the injected polarization state at 45° slowly rotates in accordance with the polarization splitting determined from Section 4.1.4 to $\Delta_{xy}/\hbar \approx 0.03 \text{ps}^{-1}$. Since we detect a real-space image, we create a histogram of the x -positions visited by the trajectories and weight them with the factor $w = \exp(-t/\tau_{1/e}) \cdot (1 - \cos(\Delta_{xy}t/\hbar))$ to obtain Fig. 4.9(d). It shows the expected intensity distributions as functions of position x , for the two opposing bias cases. As in the experiment, we calculate the normalized difference between the two cases and compare the result with the experiment in Fig. 4.8(b) (green dashed line). The red-blue colored points correspond to a line cut through Fig. 4.8(a) at $y = 25 \mu\text{m}$ and the black curve is an average over y between 10 and $40 \mu\text{m}$. Remarkably, this simple approach allows us to obtain reasonable quantitative agreement with our data. We verified that the result does not depend sensitively on the parameters $\tau_{1/e}$ and Δ_{xy} . We want to point out that for the interpretation of the real-space images, one has to take into account the effective mass of the polaritons, which might be negative at

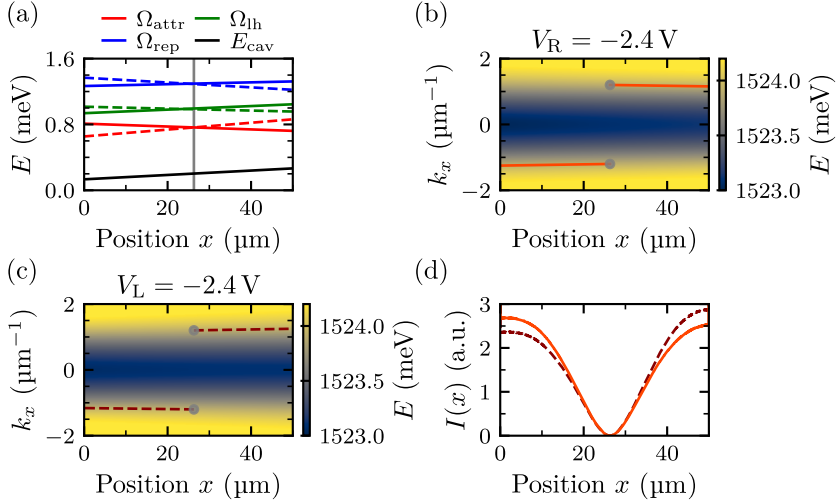


Figure 4.9: Coupled oscillator model to predict the polariton acceleration. (a) Local dispersion fit results. (b) Corresponding E_{LP} for depletion on the right and (c) depletion on the left side. Trajectories of lower polaritons are drawn with initial values marked by gray dots. (d) Expected emission from the trajectories shown in (b,c).

large $|k_x|$ due to the non-parabolic polariton dispersion relation. Consider the full line in Fig. 4.9(d), where polaritons are accelerated to the left. Due to the large in-plane momentum k_x , the acceleration actually reduces the group velocity during propagation. This leads to an excess of polaritons on the left side compared to acceleration in the opposite direction (dashed line). If we had access to a larger field of view, we would expect the normalized difference to change sign. In this model, the total number of polaritons remains constant when subjected to accelerating potentials but the position where they are re-emitted as photons is affected.

4. Transport of Polaritons with External Electric and Magnetic Fields

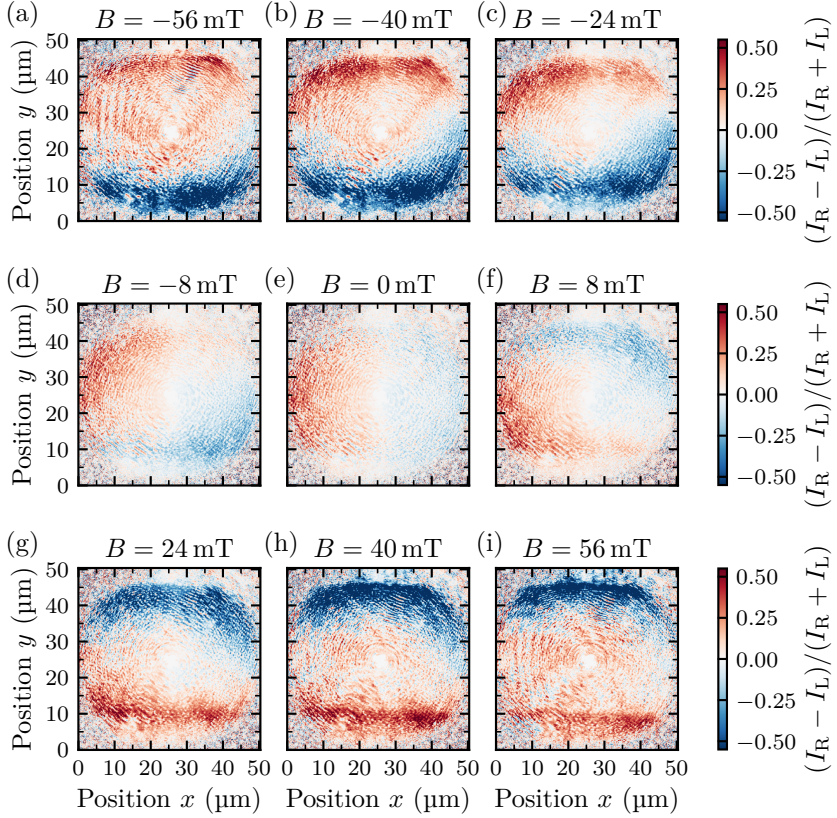


Figure 4.10: Polariton acceleration in external electric and magnetic fields. (a-i) Normalized difference between RF images $(I_R - I_L)/(I_R + I_L)$ acquired for a range of magnetic fields from -56 mT to 56 mT displayed above the images. All other parameters are kept identical for the different panels; performed with sample A.

4.3 Polariton Transport by Magnetic Fields

4.3.1 Acceleration by Hall Voltage

We can further control the polariton flow by applying a magnetic field perpendicular to the QW plane. In conjunction with a finite source-drain bias, this induces a Hall voltage transverse to the applied potential leading to charge redistribution in the y -direction [217, 218]. The combined electric and magnetic fields now shape the electron density gradient which can be tuned in angle and magnitude, as demonstrated in Fig. 4.10. All Figs. 4.10(a) to 4.10(i) correspond to alternating voltage biases of $V_R = -2.4\text{ V}$ and $V_L = -2.4\text{ V}$ and a fixed magnetic field indicated above each panel. Figures 4.10(b) and 4.10(f), at $\pm 8\text{ mT}$ show the possibility to orient the polariton flow in a diagonal direction. Further increasing the magnetic field to tens of mT leads to polariton transport in the up-down direction with an intensity contrast of roughly 50%. Moreover, flipping the sign of the applied magnetic field reverses the direction of polariton transport.

While these results demonstrate the possibility to transport dressed photons (i.e. polaritons) by electric and magnetic fields, it should be noted that we do not observe here a Lorentz force for photons. In particular, the force acting on polaritons does not appear to depend on the direction of their motion. As clearly shown, for example, by inspecting Fig. 4.10(h), both the polaritons propagating to the left and to the right are deflected in the same direction for a particular choice of bias voltage. The polariton acceleration is determined only by the electron density gradient which in turn is controlled by the combination of magnetic field and electrical bias. In other words, the non-perturbative coupling of polaritons to itinerant electrons allows for the control of photons by electromagnetic forces acting on the electronic sector.

4.3.2 Spin Density Gradients

We extend our work to higher magnetic fields, where the 2DES enters the quantum Hall regime. We aim to exploit spin-density gradients instead of unpolarized electron density gradients to further our control over polariton acceleration. In this section, we establish the presence of spin-density gradients. We start by briefly restating the underlying features of polaron-polaritons in the IQHE that were studied in detail in Chapter 3 and then

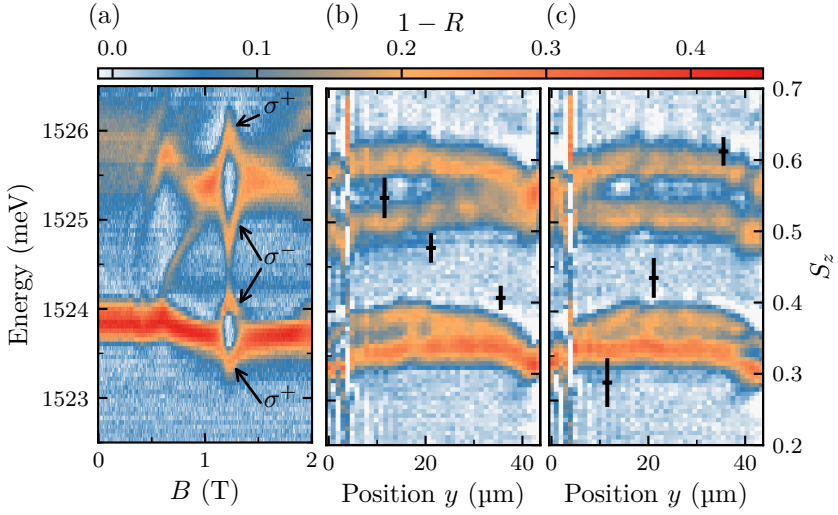


Figure 4.11: Spatial tuning of the polariton energy landscape by spin density gradients in the quantum Hall regime. (a) Normalized white light reflectivity spectra measured at $k_{\parallel} = 1.2 \mu\text{m}^{-1}$ as a function of magnetic field without bias voltage. (b) Normalized reflectivity spectra at $k_{\parallel} = 1.2 \mu\text{m}^{-1}$ and $B = 1.1 \text{ T}$ across the vertical y -direction on the Hall bar, with a source-drain bias $V_{\text{R}} = -0.17 \text{ V}$. Black points indicates the electron spin polarization S_z measured at three different positions. (c) Opposite spin density gradient to (b) with $V_{\text{L}} = -0.35 \text{ V}$. Error bars are extracted from the fit parameters; measurements performed with sample A.

extend the discussion to involve electron density gradients.

At low temperature and under a strong magnetic field, the optical excitation spectrum of a high mobility 2DEG exhibits energy gaps due to the quantization of cyclotron orbits. The corresponding Landau levels are further split in energy by a Zeeman field, forming a ladder of spin subbands for the electrons. As the occupancy of this ladder is varied (e.g. by tuning the magnetic field), the 2DEG undergoes phase transitions between electronic ground states of different spin polarization S_z . In particular, when the lower spin subband of the first Landau level is completely filled ($\nu = 1$), the electronic ground-state is an itinerant ferromagnet with strong spin polarization. The fact that polaron dressing occurs exclusively in the configuration where the optically excited electron and the electrons in the 2DEG dressing cloud have opposite spin, renders the polaron very sensitive to the spin polarization of the 2DEG. At $\nu = 1$, the polaron oscillator strength is maximum for right-hand circularly polarized light σ^+ since most of the 2DEG electrons are in the spin up state, thus allowing for efficient dressing. Conversely, the oscillator strength is reduced for left-hand circularly polarized light σ^- due to the absence of spin-down electrons. The ensuing variations of polaron oscillator strength have a direct counterpart in the Rabi splittings Ω_{σ^\pm} of the corresponding polaron-polariton branches, as shown in Fig. 4.11(a) for the polariton Hall bar sample. The optical polarization was set to linear, so that both circularly polarized polariton branches are visible. The degree of electron spin polarization can be inferred from the Rabi splittings by Eq. (3.2), leading to about $S_z \approx (\Omega_{\sigma^+}^2 - \Omega_{\sigma^-}^2)/(\Omega_{\sigma^+}^2 + \Omega_{\sigma^-}^2) \approx 70\%$ at $\nu = 1$ (1.26 T) as we found previously.

In this quantum Hall regime, the charge density gradients demonstrated above may translate into gradients of 2DEG spin polarization, resulting in optical spin-contrasted forces for polaritons. To this end, we detune the magnetic field slightly from $\nu = 1$ to 1.1 T so that the polaron branches are most sensitive to changes in electron density. Note that $\nu \propto 1/B$ makes it possible predict the effect of electron density gradients from the magnetic field dependence in Fig. 4.11(a). The spatial dependence in Fig. 4.11(b) shows the evolution of the polariton spectrum at $k_{\parallel} = 1.2 \mu\text{m}^{-1}$, recorded from the lower edge to the upper edge of the Hall bar (its y -direction) under

a voltage bias¹¹ of $V_R = -0.17\text{ V}$ and a magnetic field of 1.1 T . The in-plane momentum was chosen to optimize the cavity detuning. We observe four energy branches, as expected from a vertical cut in Fig. 4.11(a) near $\nu = 1$, where the two inner branches are the σ^- -polarized lower and upper polaritons and the two outer branches are the σ^+ -polarized lower and upper polaritons. To assess the degree of spin polarization S_z of the 2DEG, we measure polariton dispersions in σ^+ and σ^- polarizations at three different y -positions (not shown). From the dispersions, the Rabi splittings are extracted by a fit based on coupled oscillators Eq. (4.1). As can be seen in Fig. 4.11(b), the degree of electron spin polarization of the 2DEG (black markers, right axis) evolves across the Hall bar. The magnitude of the spin gradient is sizable across the optical field of view, ranging from about 30 to 60 % spin polarization. Furthermore, it can be controlled electrically as demonstrated in Fig. 4.11(c), where $V_L = -0.35\text{ V}$ reverses the gradient. The combination of voltages correspond to a balanced situation where the filling factors at $y = 25\text{ }\mu\text{m}$ are equal and the gradients opposite. Such variations in S_z constitute gradients of opposite signs for the σ^+ and σ^- polaron-polariton energy landscapes.

4.3.3 Polariton Spin Sorting

We demonstrate how this idea of spin-density gradients can be extended to realize transverse polariton spin currents reminiscent of an intrinsic spin-Hall effect when the 2DEG is close to the $\nu = 1$ integer quantum Hall state. To investigate the resulting spin-dependent polariton acceleration, we first perform momentum-resolved measurements by imaging the polariton RF emission. An excitation energy of 1523.8 meV (813.62 nm) is chosen to intercept both the σ^+ and σ^- lower polariton dispersions at finite k_{\parallel} . Figures 4.12(a) and 4.12(b) show the momentum-resolved polariton RF signal for $V_R = -0.17\text{ V}$ and $V_L = -0.35\text{ V}$ respectively. It has been acquired using a CCD camera in Fourier space, the excitation laser being filtered out by polarization suppression. As can be seen in the left panel Fig. 4.12(a), the inner σ^- -polarized branch is shifted up towards positive k_y while the outer σ^+ -polarized branch is shifted down towards negative k_y . This observation

¹¹Lower bias voltages are required to remain in the quantum Hall regime, as compared to the measurements performed without magnetic field.

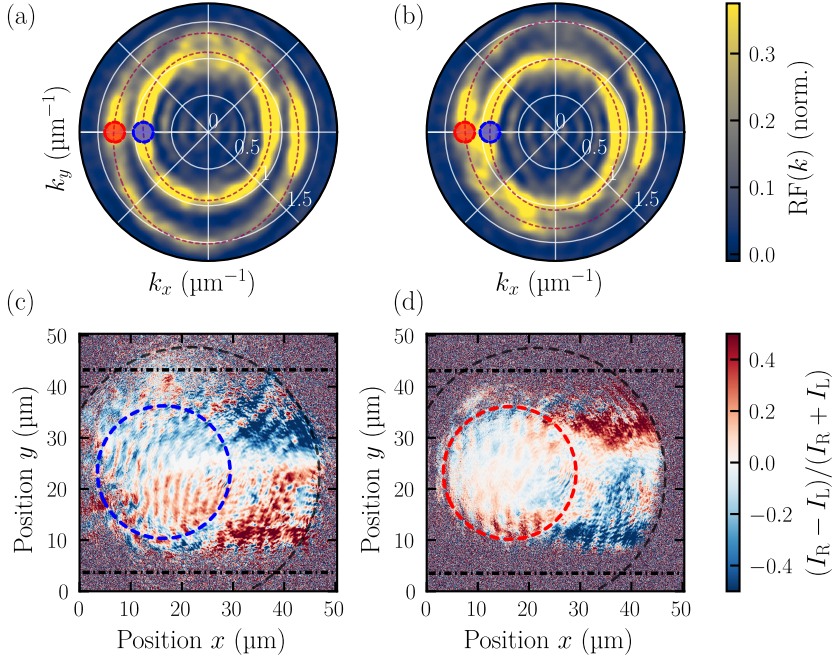


Figure 4.12: Spin-selective polariton acceleration. (a,b) Momentum-resolved polariton RF emission under cross-linear polarization at 1523.8 meV (813.62 nm) for (a) $V_R = -0.17\text{ V}$ and (b) $V_L = -0.35\text{ V}$. The dashed lines are guides to the eye highlighting the elliptical shape of the dispersion cuts. (c,d) Normalized difference between two RF images of right-propagating polaritons acquired with $V_R = -0.17\text{ V}$ and $V_L = -0.35\text{ V}$. (c) Excitation of σ^- polaritons at $k_x = -0.9\ \mu\text{m}^{-1}$, $k_y = 0$. (d) Excitation of σ^+ polaritons at $k_x = -1.3\ \mu\text{m}^{-1}$, $k_y = 0$. The horizontal dashed-dotted lines delimit the width of the Hall bar, the large circle is the field of view of the microscope. The red and blue rings in (a-d) show the excitation spots in real and momentum spaces for σ^+ and σ^- polaritons, respectively.

4. Transport of Polaritons with External Electric and Magnetic Fields

directly demonstrates an in-plane acceleration whose sign depends on the polaritons spin polarization S_z^{pol} in the given state, that is the component of the polariton pseudo-spin normal to the sample surface [219]. The effect is reversed in Fig. 4.12(b), where the external bias and thereby the gradient in electron spin polarization points in the opposite y -direction. The real-space counterpart of this acceleration allows for the generation of transverse optical spin currents, reminiscent of an intrinsic optical spin-Hall effect [220–226].

To demonstrate the generation of transverse polariton spin currents, we inject polariton wave packets of well defined momenta by focusing the excitation beam in the back-focal plane of the objective lens. Figures 4.12(c) and 4.12(d) correspond to excitation at $k_x = -0.9 \mu\text{m}^{-1}$, $k_y = 0$ and $k_x = -1.3 \mu\text{m}^{-1}$, $k_y = 0$, resulting in right propagating¹² polaritons with σ^- and σ^+ polarization, respectively. The normalized difference of the propagation images (RF, real space), acquired with the two different voltage biases, indeed reveals opposite acceleration of σ^- and σ^+ polaritons along the y -direction. The spin-dependent momentum shifts demonstrated here, although capable of generating transverse spin currents, remains fundamentally different from the usual Rashba type coupling at the origin of standard spin-Hall effects. Instead, the interaction reported here is analogous to a force for photons, where the spatially varying electron spin polarization (S_z) acts as an accelerating potential, sorting polaritons of different spin (S_z^{pol}) in different directions:

$$\vec{F}_{\text{Photon}} \sim S_z^{\text{pol}} \vec{\nabla} S_z. \quad (4.5)$$

It should be noted that the evolution of electron spin polarization around $\nu = 1$ quantum Hall plateau is widely believed to involve the proliferation of skyrmions in the quantum Hall ferromagnetic state due to the interplay between Zeeman and Coulomb energies [227]. The spin-singlet polaron-polariton dressing thus constitutes a new interface for coupling the optical spin of photons to the electronic spin excitations of 2DEGs. The behavior of such interactions in the fractional quantum Hall regime where excitons may be dressed by fractionally charged quasi-particles remain to be explored.

¹²The situation appears mirror-reflected since we reference the momentum as viewed in the direction of excitation.

4.4 Conclusion and Perspectives

In summary, we demonstrated novel ways of controlling photons with external electric and magnetic fields, which are enabled by their hybridization with polarization waves in a medium. While these results were obtained in the context of exciton-polaritons interacting with electrons, we highlight that the underlying mechanism is general and could allow for the electrical control of photons hybridized with other kinds of polarization waves such as phonons or plasmons, provided that the quanta of polarization concurrently interact with free electrons or holes.

A non-equilibrium electron density gradient is shown to act as an artificial electric field for polaron-polaritons which is tunable in strength and direction. We foresee that this effective electric field could be further controlled by tailoring the 2DEG density by using patterned electrodes. By mapping the energy landscape of the lower polariton, we reach quantitative agreement between a simple trajectory based model and the observed polariton acceleration. Our experiment constitutes an alternative to the already proposed polariton drag effect for exerting electro-magnetic forces on neutral optical excitations [203, 207]. We emphasize that the electron density gradients we exploit are generic for low density 2DEGs when large source-drain voltages are applied and therefore need to be considered in view of polariton drag experiments. In the integer quantum Hall regime, we demonstrated that electron spin depolarization, induced by the proliferation of skyrmions as the electron density gradient pushes the system away from $\nu = 1$ filling, constitutes a scalar potential for the optical spin of photons and results in spin-dependent acceleration.

The polariton spectrum probes the bulk properties of the 2DES, contrary to electrical transport measurements which are dominated by edge currents in the QH regime. For studying the interplay between edge currents and polaritons, our current approach is severely limited by degradation of the polariton linewidth some micrometers from the sample edge (see Fig. 4.1(b)). This is due to leakage of light from the cavity on the sides and probably amplified by the lack of a sharply defined sample edge due the wet etching technique we used. Another limitation is the low amount of electrical current density our device can sustain before it enters the nonlinear transport regime. Probably for this reason, we were unable to clearly demonstrate the predictions

in [203, 207] even using interferometric techniques [194]. For this purpose a device optimized for higher current density in the linear transport regime should be developed.

Recently, there has been exciting progress on the problem of detecting quasi-particle exchange statistics and towards anyon braiding [186, 228]. In the context of these works, screening quantum wells were employed above and below the 2DEG resulting in a qualitatively analogous structure to our DQW-QW-DQW layout (Fig. 4.1(a)). In this work, separate gates were deposited to selectively deplete the screening quantum wells. This allows to remove the parallel conductance to restore good electrical transport properties in the presence of screening quantum wells. The structure could be adapted to create Hall bar devices without the trade-off we faced between optical and electrical properties. This would create an ideal platform for studying the interplay between polariton and electronic transport. Furthermore, high-quality quantum Hall transport measurements could be performed in parallel to optical cavity spectroscopy. An easier alternative might be a reduction of the DQW thickness with the goal to quench the carrier mobility within these layers. However, this reduction of mobility would also remove the ability to act as screening layers against charge fluctuations, induced for example by light absorbed at defects in the cavity spacer or within the DBR layers.

Polariton Interactions in the Fractional Quantum Hall Regime

The linearity of Maxwell’s equations—which implies the superposition principle—excludes optical photons from interacting directly with each other. Hybridization of photons with material resonances, in particular exciton-polaritons, circumvent this limitation by using the interactions of quasiparticles in a medium. It is an ongoing challenge to create stronger optical nonlinearities that remain relevant in the single photon regime. We follow our approach of the previous chapters to hybridize photons with exciton-polarons but turn to the nonlinear response of the resulting polaritons¹. We find that their nonlinear response is enhanced at fractional filling factors $\nu = 2/5$ and $\nu = 2/3$, relative to neighboring fillings. In addition to prospects for polariton blockade, these measurements suggest that nonlinear spectroscopy could provide new insights into quantum Hall states not accessible in linear optical spectroscopy and motivate further study.

¹The experiments that constitute this chapter were published in the article [229], with corresponding experimental data available in the ETH Research Collection [230]. The work presented here was performed together with Dr. Sylvain Ravets, both of us contributing equally.

Engineering strong interactions between optical photons is a great challenge for quantum science. Envisioned applications range from the realization of photonic gates for quantum information processing [192] to synthesis of photonic quantum materials for investigation of strongly-correlated driven-dissipative systems [9]. Polaritonics, based on the strong coupling of photons to atomic or electronic excitations in an optical resonator, has emerged as a promising approach to implement those tasks [17]. They have recently attracted considerable interest, motivated by the fact that their interactions can be engineered through the tunability of their matter component. For example, strongly interacting Rydberg polaritons have been obtained using the nonlinear behavior of Rydberg excitations in an ensemble of atoms, which led to the demonstration of Rydberg polariton blockade [7] where the presence of a single polariton in a well-delimited region of space prevents the resonant injection of other polaritons. In parallel, efforts are being made to realize polariton blockade in condensed matter systems that hold great potential for realizing compact and integrated synthetic quantum materials [17]. Exciton polaritons in semiconductor materials are part light part matter particles that arise from the strong coupling of a quantum well exciton and a cavity photon [8]. These photonic particles inherit a nonlinear behavior from exciton-exciton interactions [8, 9] which lead to striking observations of optical bi-stability, Bose-Einstein condensation and superfluidity. For efficient polariton blockade to be obtained, the polariton interaction energy U_p needs to be greater than the inverse lifetime γ of the polaritons [30].

Recent state-of-the-art experiments based on photon correlation measurements in semi-integrated microcavities attained optimized values of the ratio $U_p/\gamma \simeq 0.1$ in a photonic dot with about $3\ \mu\text{m}^2$ area [31, 32]. These experiments represent the culmination of decade long technological developments aimed at increasing U_p/γ through reducing the photonic mode area [31, 32, 231] as well as increasing the lifetime [232]. They demonstrated the onset of quantum correlations in the exciton-polariton system [31, 32], showing that strong polariton blockade [30] could be achieved if interactions were one order of magnitude stronger. Recently, several possibilities have been explored for enhancing U_p through an increase of exciton-exciton interactions U_x , focusing either on bi-exciton Feshbach resonance [233] or on excitons with a permanent dipole moment [234–236]. The experiments we report here reveal a hitherto unexplored mechanism for optical nonlinearity emerging for

polaritonic excitations out of a two dimensional electron system in the fractional quantum Hall regime. Using time resolved four-wave mixing (FWM) experiments, we find that polaron-polaron interactions U are enhanced by more than an order of magnitude around the fractional state at filling factor $\nu = 2/5$ as compared to other neighboring compressible states. A comparison of interaction strengths for $\nu = 2/5$ shows a factor of 4.6 ± 0.9 enhancement with respect to U_x of an undoped QW. Our experiments indicate that strong correlations in the electronic ground state play key role due the observed dependence on filling factor. In addition, exciton-electron interactions leading to the formation of polaron polaritons [21, 82, 84, 106] and their residual Coulomb interactions could be contributing to the enhanced nonlinear optical response. Moreover, we find that the lower polariton linewidth γ in our sample is similar to the values reported in recent experiments demonstrating modest quantum correlations [31, 32], indicating that upon spatial confinement polariton blockade regime could be reached. Besides potential applications in realization of strongly interacting photonic systems, our findings suggest that nonlinear optical measurements could provide information about fractional quantum Hall states that is not accessible in linear optical or transport measurements.

This chapter is structured as follows. We begin by looking back at linear spectroscopy of the polariton resonances at filling factors $\nu = 1, 2/3$ and $2/5$ to establish the exact experimental conditions for the following experiments. We introduce the FWM setup employed and proceed with measurements of the nonlinear optical response as a function of filling factors to demonstrate the enhanced nonlinearity. We discuss our attempts to model the response and open questions that remain.

5.1 Experimental Methods and Polariton Spectroscopy

5.1.1 Setup and Linear Polariton Spectroscopy

The following experiments were performed with samples embedded in DBR microcavities. If not stated otherwise, the experiments involved sample A, containing a low density electron gas (details in Section 2.4.1). The sample was mounted inside a dilution refrigerator with fiber optical access, as shown

5. Polariton Interactions in the Fractional Quantum Hall Regime

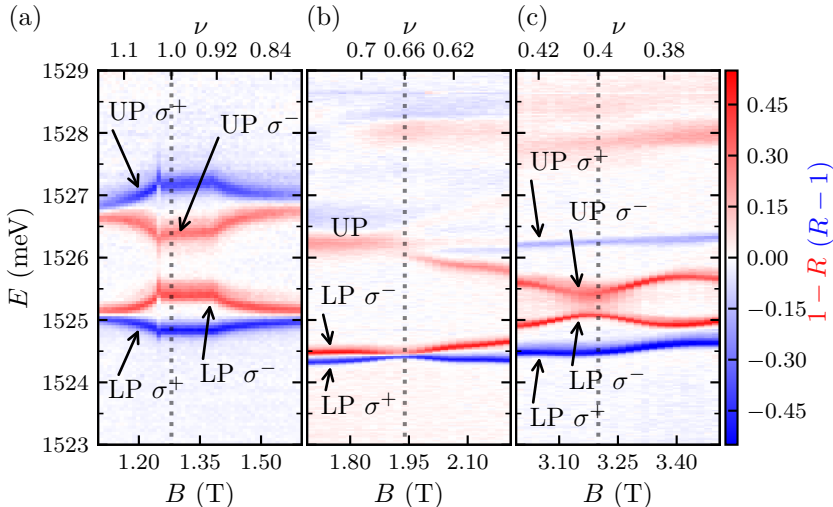


Figure 5.1: Quantum Hall polariton resonances—linear polarization resolved spectroscopy as function of filling factor. Normalized white light reflectivity spectra recorded around filling factors (a) $\nu = 1$, (b) $2/3$ and (c) $2/5$. The plots show the difference between two spectra obtained separately using σ^- (red) and σ^+ polarized light (blue).

in Fig. 2.7(a). The extension to the optical setup described in the next section concerns only the parts outside of the dilution unit.

We first characterize our sample using optical spectroscopy in the low-power (linear) regime. We record polarization-resolved white light reflectivity spectra for several values of ν by changing B using a few nanowatts of circularly-polarized light from a broadband light source. Figure 5.1 plots an overview of the polaron-polariton resonances for our system, obtained by calculating the difference between the spectra measured separately using σ^- (red) and σ^+ (blue) polarized light. We observe generic strong dispersion of the polariton energies with magnetic field around integer and fractional values of ν . This striking behavior of the linear optical spectrum stems from strong modification of electron-exciton interactions in and around gapped quantum Hall states, which in turn leads to a ν -dependent modification of the cavity-polaron coupling strength. We recall that the electron density is fixed for this sample, so that the filling factor ν is tuned via the magnetic field

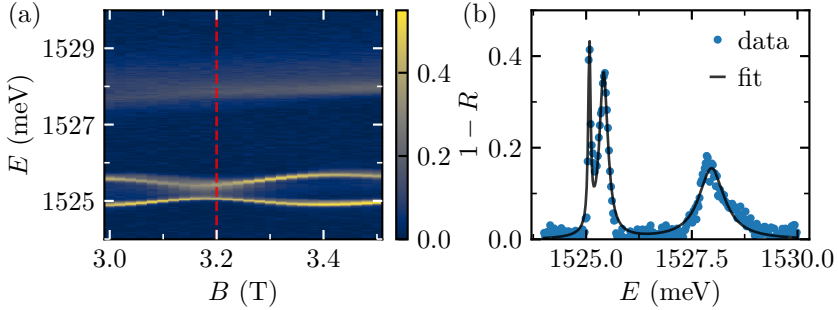


Figure 5.2: Polaron-polariton characterization at $\nu = 2/5$. (a) White light reflectivity spectra as a function of magnetic field. The red dashed line is indicating the line-cut (b), which shows the background-subtracted reflectivity (blue circles) at $B = 3.2$ T with a fit (black line) consisting of a sum of three Lorentzian resonances.

only. The panels are centered around the spin polarized integer state $\nu = 1$ (Fig. 5.1(a)), the spin unpolarized fractional state $\nu = 2/3$ (Fig. 5.1(b)) and the spin polarized fractional state $\nu = 2/5$ (Fig. 5.1(c)).

To evaluate the interaction strength from the nonlinear response, we will require a few input parameters from the linear spectra. We summarize, in Fig. 5.2, the fitting procedure for the $\nu = 2/5$ case. The spectra around $\nu = 2/5$ are replicated once more in Fig. 5.2(a). We fit the white light reflectivity spectrum obtained at $B = 3.2$ T (marked by the red dashed line) by a sum of three Lorentzian functions to extract the LP linewidth $\gamma = 67 \pm 5$ μeV , the LP cavity content $|C|^2 \approx 0.12$ and LP peak amplitude $\simeq 0.40$. We note that the LP linewidth is narrower than the bare cavity linewidth $\gamma_{\text{cav}} = 275$ μeV despite the large matter component of 88%: reduction of the cavity content has resulted in a reduction of the polariton linewidth as would be expected in a sample where excitons only decay through their coupling to the cavity. This indicates that the presence of the 2DES does not broaden the lower polariton linewidth. The line-cut together with the fit are plotted in Fig. 5.2(b).

5.1.2 Time-Resolved Four-Wave Mixing Setup

Figure 5.3 shows the principle of the time-resolved interferometer we developed, inspired by traditional FWM techniques, to characterize our sample in

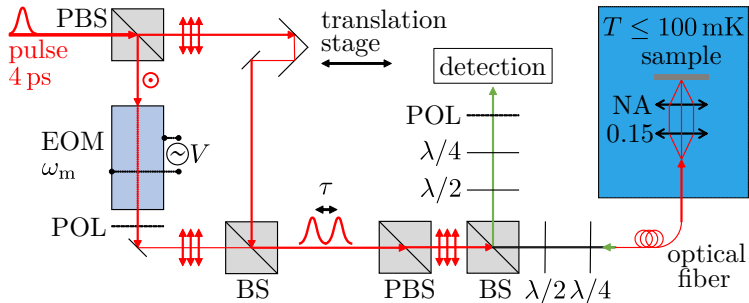


Figure 5.3: Optical setup for four-wave mixing experiments: schematic of the interferometer used for measuring the nonlinear response of the system. Two laser pulses separated by a variable delay τ generate an induced polarization in the sample, after the amplitude of one pulse was modulated with an electro-optical modulator (EOM). The emitted photons are sent onto an APD for detection where linear contributions are separated from nonlinear contributions by demodulating the harmonics of the modulation frequency. Polarizer (POL), half waveplate ($\lambda/2$), quarter waveplate ($\lambda/4$).

the nonlinear regime. We use a pulsed Ti:Sapphire laser² with a $T_{\text{pulse}} = 4$ ps pulse duration, a 76 MHz repetition rate and center frequency tuned to the σ^- polarization lower polariton resonance (LP_{σ^-}). We split the laser into two paths with the first polarizing beam splitter (PBS) and introduce a variable time delay τ between the two pulses using a motorized translation stage. For optical excitation, we recombine both beams onto another beam splitter (BS). After passing another PBS and BS, which is used to separate out the collected light later, the linearly-polarized light is coupled into an optical fiber routed to the sample. The excitation light is then focused onto the sample surface using a low NA = 0.15 objective. This implies that the two beams are co-propagating and collinear albeit with low but finite angular spread given by this NA. The total field incident on the sample is given by $E(t, \tau) = E_1(t) + E_2(t, \tau)$, where the average intensities of the two beams are chosen to be equal. For detection, we collect the generated resonance fluorescence using the same fiber as the one used for excitation, and we filter out the laser background light by detecting along the cross-polarized axis.

²Coherent Mira Optima 900-P.

The collected light is finally sent onto an avalanche photodiode (APD) for detection. Modeling our system as a third order nonlinear medium, we can expand the total intensity reaching the photodetector I_{det} as:

$$I_{\text{det}}(t, \tau) \propto \epsilon_0 \left| P_1^{(1)}(t) + P_2^{(1)}(t, \tau) + P^{(3)}(t, \tau) \right|^2. \quad (5.1)$$

The linear polarizations in response to the incoming fields E_1, E_2 are written as $P_{1,2}^{(1)}(t)$, understood as the inverse Fourier transforms of $P_{1,2}^{(1)}(\omega)$. The nonlinear polarization $P^{(3)}(t)$ is the inverse Fourier transform of $P^{(3)}(\omega)$. To isolate weaker nonlinear terms in this expansion $\propto P_i^{(1)*} P^{(3)}$ from the dominant linear contributions $\propto P_i^{(1)*} P_j^{(1)}$ ($i, j = 1, 2$), we modulate the field amplitude $E_1(t)$ sinusoidally at frequency ω_m . By calculating $\mathcal{I}(\omega, \tau)$, the Fourier transform of $I_{\text{det}}(t, \tau)$, we can separate different terms: the (mostly) linear term $\mathcal{I}(\omega_m, \tau)$ and the nonlinear term $\mathcal{I}(3\omega_m, \tau)$. In the following, we use these two terms to quantify the nonlinearity of the system.

One standard method for evaluating interactions between exciton-polaritons in 2D uses a resonant continuous wave excitation laser to monitor the blue-shift experienced by the lower polariton line due to the (Kerr-like) nonlinearity as the polariton population increases. In these experiments, however, one cannot differentiate between the contribution due to fast (~ 10 ps) polariton-polariton interactions, and other unwanted contributions due to the slow (> 100 ps) buildup of an excitonic reservoir [237]. This issue is critical in the context of quantum Hall polaritons since the 2DES electron density is particularly sensitive to optical power due to possible photo-ionization of DX centers when illuminating the sample: increasing the optical power density may lead to unwanted modifications of n_e and therefore to slow variations of the (ν -dependent) polariton energies, which in turn may prevent us from properly evaluating the interactions. In order to isolate pure polariton-polariton interactions, we use a carefully designed sample structure with reduced sensitivity of n_e to light, and perform time-resolved experiments in the pulsed-excitation regime in which the pulse duration (4 ps) is shorter than the polariton lifetime (≥ 12 ps). A traditional approach to isolate the nonlinear contribution in four-wave mixing experiments consists in introducing an angle between the two exciting beams in order to generate a background-free nonlinear response at

a different angle [238]. However, the requirement for ultra-low temperatures render standard FWM experiments technically challenging to implement in our experimental geometry that uses a fiber coupled scanning confocal microscope in a dilution refrigerator. Note that access to the sample is restricted to reflection in collinear configuration: to separate the resonance fluorescence emitted by the sample from the laser light that reflects off the surface, we use linearly polarized light in excitation and cross-polarized detection. In this way, we suppress the background laser light by 3-4 orders of magnitude, limited by the fiber. This leaves the resonance fluorescence as the dominant contribution to the detected signal. The RF configuration is enabled by the circular selection rules in a magnetic field. To distinguish the linear response from the (weaker) nonlinear response as explained above, we use an EOM placed between two crossed polarizers as an amplitude modulator in one arm of the interferometer (see Fig. 5.3). We apply a triangular voltage profile to the EOM to create an electric field amplitude with sine modulation at frequency of $\omega_m/2\pi = 8011$ Hz. We optimize the EOM input voltage profile and the EOM alignment to realize a clean sine modulation at this frequency, with less than a percent of higher order harmonic contributions at $2, 3, 4 \times \omega_m$. The modulated excitation field becomes $E(t, \tau) = E_1(t) \sin(\omega_m t) + E_2(t, \tau)$. We finally couple the reflected signal to a single-mode fiber and send it to an APD, making sure that the count rate is well in the linear regime of the APD ($\sim 80\,000\text{ s}^{-1}$). Due to the modulation, the power spectral density $\mathcal{I}(\omega, \tau)$ contains terms that oscillate at multiples of the modulation frequency ω_m . Expanding the first order terms in Eq. (5.1)

$$\begin{aligned} & \left| P_1^{(1)}(t) \sin(\omega_m t) \right|^2 + \left| P_2^{(1)}(t, \tau) \right|^2 \\ & + 2\Re\left(P_1^{(1)}(t)^* \sin(\omega_m t) P_2^{(1)}(t, \tau) \right), \end{aligned}$$

we find that a field autocorrelation term appears at frequency ω_m . The next order terms are the cross-products between linear and nonlinear polarizations with subscripts denoting fields originating from optical paths 1 and 2

$$\begin{aligned} & 2\Re\left((P_1^{(1)*} \sin(\omega_m t) + P_2^{(1)*}) \right. \\ & \left. \cdot (P_{111}^{(3)} \sin(\omega_m t)^3 + P_{112}^{(3)} \sin(\omega_m t)^2 + P_{122}^{(3\cdot)} \sin(\omega_m t) + P_{222}^{(3)}) \right). \end{aligned}$$

It turns out that $3\omega_m$ is the first frequency for which $P^{(3)}$ contributes to all terms with no background from $P^{(1)}$, so $\mathcal{I}(3\omega_m, \tau)$ is used to monitor the nonlinear response. Similar techniques have been used for four-wave mixing experiments in collinear geometry [239–244].

The measurement procedure goes as follows. For a chosen magnetic field, we first set the cavity energy which defines the polaron content for the LP_{σ^-} . We then tune the laser pulse central energy to the LP_{σ^-} resonance and suppress the reflected laser light. We note that when scanning B (typically by few 100 mT) around a given filling factor (e.g. $\nu = 2/5$) the singlet polaron resonance energy shift is small compared to the polariton normal mode splitting³: as a consequence, we can keep the cavity energy constant while studying a given filling factor. We also keep the average intensities of pump (1) and probe (2) equal, which was found to result in a good signal to noise ratio. For each time delay τ , we acquire photon counts for 1 s, with the exception of Fig. 5.4, where we used 10 s acquisition time. The APD sampling frequency is 1 MHz, but data binning then leads to an effective sampling frequency of $9\omega_m$. We then calculate the absolute value of the Fourier transform $I(t, \tau) \mapsto \mathcal{I}(\omega, \tau)$ for the recorded time traces, from which we extract frequency bins corresponding to the first multiples of ω_m . After background removal, we finally obtain $\mathcal{I}(\omega_m, \tau)$ and $\mathcal{I}(3\omega_m, \tau)$. The background is estimated by averaging $\mathcal{I}(\omega, \tau)$ in frequency bins in the vicinity of the frequency of interest, because the background noise was not completely white, i.e. showed some frequency dependence.

We perform two test experiments to verify the procedure (not displayed). First we red-detune the laser away from any polariton resonances. Our sample then acts as a simple mirror due to the high cavity reflectivity. We adjust the detection polarizers such that the ADP count rate matches the one used in the main experiment. By applying the same experimental procedure to the signal, we observe that $\mathcal{I}(\omega_m, \tau)$ corresponds to the laser pulse spectrum, whereas no signal is observed at the frequency $3\omega_m$. This excludes the possibility that the detector or any other optical elements in the setup contribute to the observed nonlinear signal. In another test experiment, we check the behavior of $\mathcal{I}(3\omega_m, \tau)$ in response to cavity-polaron detuning. We

³This does not imply a small energy shift for the polariton formed from this singlet polaron, as presented in Fig. 5.1.

observe that the nonlinear signal decreases when we red-detune the cavity with respect to the polaron energy: this is the expected behavior since the polaron content of the polaritons is decreased, and the polaritons are thus more photon-like and the interaction strength decreases.

5.2 Time-Resolved Interaction Measurements

5.2.1 Enhanced Nonlinear Response at Fractional Fillings

We focus on the LP_{σ^-} around $\nu = 2/5$ ($B = 3.15$ T). The signal extracted at the modulation frequency ω_m is plotted against time delay τ between the pulses in Fig. 5.4(a). We observe that $\mathcal{I}(\omega_m, \tau)$ features a fast oscillation modulated by an exponential envelope. This is the expected waveform since $\mathcal{I}(\omega_m, \tau)$ is, to lowest order, the autocorrelation signal of the resonance fluorescence emitted by the sample: the carrier frequency of the fast oscillation corresponds to the (under-sampled) optical frequency and the characteristic decay time of the envelope is the polariton coherence time $T_{LP} = 24 \pm 1$ ps (dashed black line). The nonlinear contribution $\mathcal{I}(3\omega_m, \tau)$, depicted in Fig. 5.4(b), also exhibits fast oscillations as function of time delay τ but its envelope has a more complex structure as a consequence of the interplay between several interfering nonlinear terms, with characteristic timescales T_{LP} and $T_{LP}/3$. The different contributions appear to compensate exactly at short delays ($\tau = 0$). Figure 5.4(c) shows a double-logarithmic plot of the integrals $\langle \mathcal{I}(\omega_m, \tau) \rangle_\tau = \int \mathcal{I}(\omega_m, \tau) d\tau$ and $\langle \mathcal{I}(3\omega_m, \tau) \rangle_\tau = \int \mathcal{I}(3\omega_m, \tau) d\tau$ as a function of the average incident power. We observe that the former exhibits a power law with exponent 1.3 ± 0.3 , which is consistent with the expected linear behavior. By contrast, $\langle \mathcal{I}(3\omega_m, \tau) \rangle_\tau$ shows a power law with exponent 2.2 ± 0.3 that is consistent with the anticipated dependence of third-order nonlinear response, validating that $\langle \mathcal{I}(3\omega_m, \tau) \rangle_\tau$ is indeed a good measure of the nonlinearity. The observed deviation of the power law exponents from the expected values 1.0 and 2.0 is most likely due to systematic errors on the input power calibration. We emphasize that the measured nonlinearity occurs on timescales that are comparable to the polariton lifetime, which demonstrates that our method allows us to access (fast) polariton-polariton interactions. We also note that the nonlinear response saturates at high optical powers (Fig. 5.4(c)). The saturation behavior of $\langle \mathcal{I}(3\omega_m, \tau) \rangle_\tau$ at high

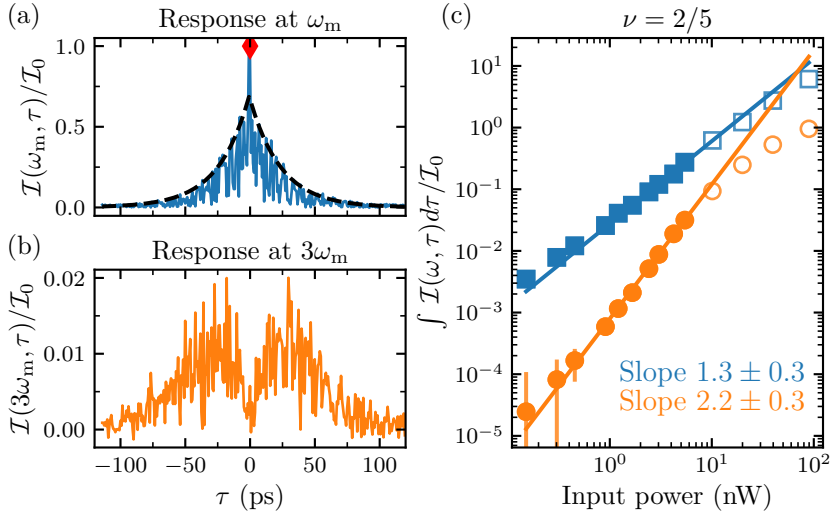


Figure 5.4: FWM traces and power dependence obtained for $\nu = 2/5$ ($B = 3.145$ T). (a) Autocorrelation signal at ω_m . (b) Nonlinear terms at $3\omega_m$. All data is normalized to the maximal value of the linear response (red diamond). The dashed black line in (a) shows a double-sided exponential decay fitted to the envelope of the linear response to obtain T_{LP} . The input average power was set to $I_2 = 2$ nW. (c) Evolution of the linear (blue squares) and nonlinear (orange circles) signal integral values as a function of the incident optical power (double logarithmic plot). The input power is given as the average power of the delayed pulse (i.e. I_2), and the error bars correspond to the statistical error on the counts only. We fit the data before saturation of the nonlinearity (full circles) by a power law (blue and orange lines). Errors on the power law exponents are dominated by systematic errors on the input power.

optical powers may be attributed to the saturation of the LP_{σ^-} red shift induced by a change in ν . Saturation could also be a consequence of (slow) light-induced modifications of n_e , which may start to play a role at the highest powers investigated.

We now analyze the evolution of $\langle \mathcal{I}(\omega_m, \tau) \rangle_\tau$ and $\langle \mathcal{I}(3\omega_m, \tau) \rangle_\tau$ as a function of ν by measuring $I(t, \tau)$ for different values of B . The data consists of three sets centered around filling factors 1, $2/3$, and $2/5$ that exhibit clear signatures of optical coupling to quantum Hall states, as demonstrated by the linear spectroscopy experiments in Fig. 5.1. For each data set, we tune B to access neighboring filling factors while keeping the cavity energy constant and adjusting the laser frequency to resonantly excite LP_{σ^-} . Our main result is the remarkable ν -dependence of the nonlinear signal $\mathcal{I}(3\omega_m, \tau)$ shown in Fig. 5.5(a). The three panels show this nonlinear signal extracted around filling factors $\nu = 1$, $2/3$ and $2/5$, shown in the colormap as function of magnetic field B and pulse delay τ . We observe a strong increase of the nonlinearity at fractional filling factors $\nu = 2/3$ ($B \simeq 1.95$ T) and $\nu = 2/5$ ($B \simeq 3.15$ T), as compared to neighboring filling factors. Away from these states, e.g. for $B = 3.5$ T, the nonlinearity becomes weaker and eventually comparable to the noise level of our apparatus. This gives clear evidence that polariton-polariton interactions are enhanced around the fractional quantum Hall states $\nu = 2/3$ and $\nu = 2/5$. In stark contrast, we observe that $\mathcal{I}(3\omega_m, \tau)$ is only marginally modified around the integer filling factor $\nu = 1$. We summarize our results in Fig. 5.5(c), where we provide values of the enhancement of polariton-polariton interactions close to fractional filling factors, obtained by calculating the ratio of the areas $R_a = \langle \mathcal{I}(3\omega_m, \tau) \rangle_\tau / \langle \mathcal{I}(\omega_m, \tau) \rangle_\tau$ and the ratio of the signal peak-to-peak values⁴ R_{pp} . At $\nu = 2/5$, both measures show a significant enhancement of the interaction, of the order of 10, as compared to neighboring filling factors.

We speculate that the enhanced optical nonlinearity we observe for polaritons generated by σ^- excitation is a consequence of the fragility of FQHE states against changes in ν . Due to the absence of electron-hole symmetry at low B fields, optical excitation of an electron to the spin-up LL0 modifies the effective filling factor by creating quasiparticles. The size of the incompressibility gap should determine the number of extra electrons that

⁴Def. $R_{pp} = (\max(\mathcal{I}(3\omega_m, \tau)) - \min(\mathcal{I}(3\omega_m, \tau))) / (\max(\mathcal{I}(\omega_m, \tau)) - \min(\mathcal{I}(\omega_m, \tau)))$.

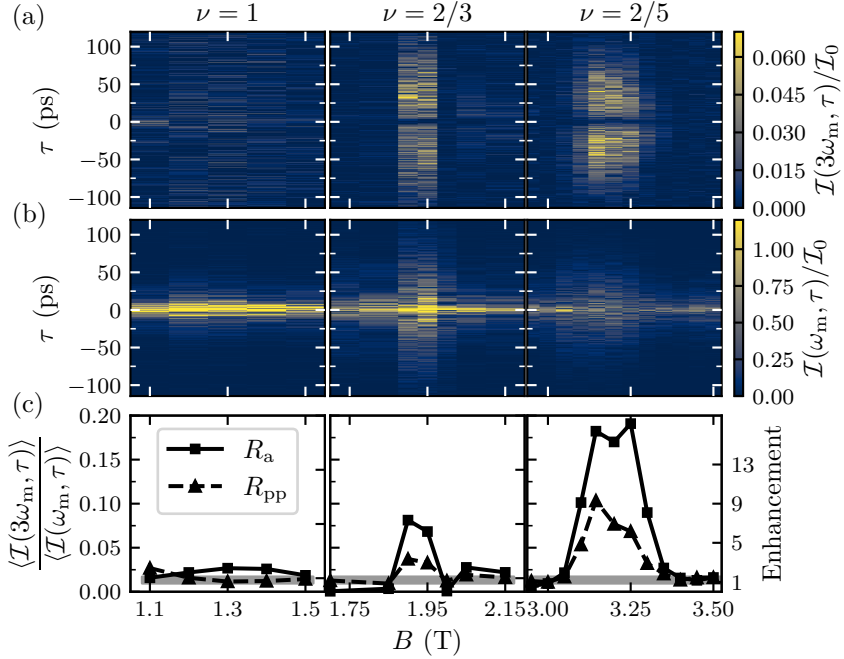


Figure 5.5: Enhancing interactions between quantum Hall polaritons at fractional filling factors. (a) Nonlinear response $\mathcal{I}(3\omega_m, \tau)/\mathcal{I}_0$ and (b) linear response $\mathcal{I}(\omega_m, \tau)/\mathcal{I}_0$ as a function of B , in vicinity of filling factors $\nu = 1, 2/3$ and $2/5$. All data is normalized by the same value \mathcal{I}_0 as in Fig. 5.4. (c) Enhancement of the nonlinearity, as revealed by the ratio of $3\omega_m$ and ω_m responses. Two different measures of the enhancement strength are plotted, the area R_a integrated over τ (squares) and the signal peak-to-peak R_{pp} (triangles). In order to obtain a lower bound for the enhancement of interactions, we compare the signal to the noise level. Taking the outermost points in each panel as reference points, the y -axis on the right hand side gives the relative enhancement of U . The gray shaded area is the standard deviation of the reference points. The excitation power for all measurements is $I = 20 \pm 3$ nW.

can be excited (by photons) before the electronic system becomes compressible. Optical modification of the electronic ground-state in turn modifies the ability of the electrons to dynamically screen the excitons, resulting in a conditional shift of the polaron-polariton resonance that underlies the nonlinear response. In contrast, for IQHE state $\nu = 1$, we do not observe a significant enhancement of interactions because the electronic state is robust against small deviations in the filling factor, which in turn leads to a small modification of the photonic resonances. One might wonder whether the nonlinearity is simply proportional to the derivative $dE_{\text{LP}}/d\nu$, induced for example by light-induced changes in n_e . The polariton energies do disperse with filling factor even for $\nu = 1$ Fig. 5.1(a). We therefore conclude that a simple light induced change in n_e (disregarding the relevance of the timescale at which this change occurs) cannot explain the observed magnetic field dependence of the nonlinearity.

Further experimental evidence supporting this tentative explanation is provided by exciting the LP_{σ^+} resonance at $\nu = 2/5$, where we did not observe any enhancement of the nonlinearity. Since σ^+ excitation generates an electron in the spin-down LL0, it does not lead to a direct modification of ν ; the absence of an enhancement of nonlinearity for σ^+ excitation is therefore consistent with our explanation. We repeated the experiment around the $\nu = 1/3$ state ($B = 3.9$ T), where we also did not observe an enhanced nonlinearity. We argue that this is due to the suppression of σ^- polarized polaron formation due to perfect spin polarization of the 2DES at $\nu \leq 1/3$, leaving the polariton mode mostly photonic (we refer back to Section 3.3.3). The large incompressibility gap of $\nu = 1/3$ may also contribute to the suppression of the nonlinearity.

Last but not least, we measured enhanced nonlinearity also on a second sample with higher electron density (sample B) for the $\nu = 2/3$ state at $B \simeq 8.6$ T. We plot, in Fig. 5.6(a), the white light reflectivity measurement recorded in (imperfect) σ^- polarization around filling factor $\nu = 2/3$ ($B \simeq 8.6$ T) at the detuning chosen for FWM measurements. Note that, contrary to the low electron density device presented in Fig. 5.1(b), the $\nu = 2/3$ state is spin-polarized at this magnetic field. This is observed in the reflection spectrum, that resembles the spectrum recorded for the (spin-polarized) state at $\nu = 2/5$ in sample A. There is a sharp reduction of normal mode splitting at $B = 8.65$ T. We note however that the coupling efficiency of incident light

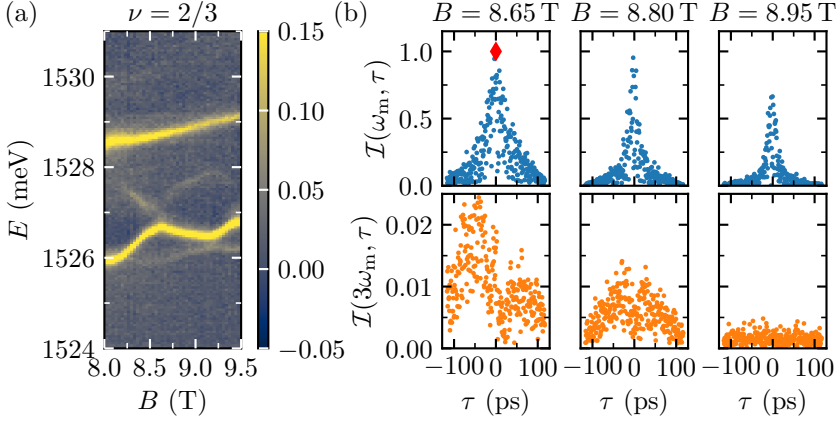


Figure 5.6: Additional FWM data from sample B. (a) Normalized white light reflectivity spectrum recorded using σ^- polarized light. At $B = 8.6$ T, the optical signature of $\nu = 2/3$ shows as a reduction of the polariton splitting around 1527 meV (note that the upper polariton is particularly faint). (b) FWM experiment around filling factor $\nu = 2/3$. The top row shows $\mathcal{I}(\omega_m, \tau)$ while the bottom row shows $\mathcal{I}(3\omega_m, \tau)$. All data has been normalized to the maximal value of $\mathcal{I}(\omega_m, \tau)$ at $B = 8.65$ T (red diamond). The integration time was chosen equal to 10 s and the input power was 35 ± 5 nW.

into the polariton modes was reduced in this high-density sample. We show, in Fig. 5.6(b), the results of our time-resolved four-wave mixing measurement around $\nu = 2/3$. We observe a clear nonlinear response $\mathcal{I}(3\omega_m, \tau)$ when ν is tuned to $2/3$ exactly. As we go away from $\nu = 2/3$, the nonlinearity decreases (bottom row). This behavior is very similar to the one presented above for the low-density sample, since we observe a strong dependence on the filling factor of the nonlinear response $\mathcal{I}(3\omega_m, \tau)$. The top row also shows the linear response $\mathcal{I}(\omega_m, \tau)$ for comparison. With this measurement, we demonstrate the repeatability of our measurement, using another sample with higher electron density. A quantitative comparison of the interaction strengths between the two samples, is however rendered difficult due to the different experimental conditions relevant for the two samples; in particular, due to the strong difference in coupling efficiency of incident light into the polariton modes in the two samples.

5.2.2 Interactions and Kerr Model for an Intrinsic QW

We have demonstrated that the nonlinear response of polaron polaritons increases as we tune the system to fractional quantum Hall filling factors. This enabled us to quantify the enhancement of polariton interactions at fractional filling factors as compared to more generic filling factors in the vicinity of these particular fractional quantum Hall states. This is a relative comparison and experimentally very robust because a change in magnetic field by a fraction of a Tesla is the only control variable. However, we would like to attempt a more quantitative estimation of the interactions strengths from the measured nonlinear response. For this purpose, we perform the same FWM experiment on sample C with a gate voltage applied in order to remove the 2D hole gas. It is a model system for an intrinsic, undoped QW but structurally more comparable to sample A. In this section, we will report aforementioned FWM experiments on the QW sample and develop a model based on the driven-dissipative Gross-Pitaevskii equation for polaritons [245, 246] to account for the nonlinear response. This will establish a direct link between the measured nonlinear response and the underlying polariton-polariton interaction strength. It also allows a comparison to known values of the exciton-exciton interaction strength. In the next section, we will extend this analysis to the experiments in the FQH regime.

In order to approximate the experimental conditions in the quantum Hall regime, we performed this measurement under a 10 T magnetic field⁵. This ensures that we are able to address a single exciton spin species by using linearly polarized excitation pulses. Furthermore, it allows for cross-polarization, i.e. orthogonal detection of resonance fluorescence from a σ^- polarized LP resonance. To quantify the interaction, we compare our measurements with solutions of a single mode Gross-Pitaevskii equation for the complex field $\psi(t)$, which requires that we estimate the polariton number $N = |\psi(t)|^2$ created by laser excitation in our experiment. Since we use pulsed resonant excitation with a low excitation duty cycle, we do not include in our model contributions from a dark exciton reservoir. We estimate the polariton occupation number N under pulsed picosecond laser excitation. The (Gaussian) laser pulse has a measured full width at half maximum (FWHM) that is equal to 460 μeV , while the LP resonance (Lorentzian) showed a FWHM of 300 μeV . From this, we estimate the spectral overlap

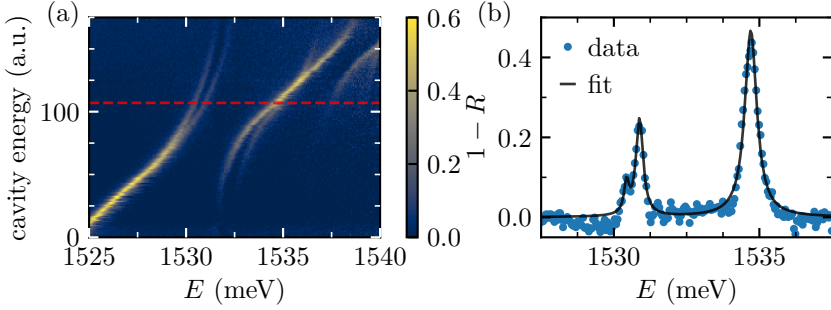


Figure 5.7: Polaron characterization for the depleted QW. (a) Evolution of the reflectivity spectra as we tune the cavity energy across the exciton resonance. The red line marks the cavity energy for the spectrum shown in the right panel. (b) Background subtracted spectrum (blue dots). The black line shows Lorentzian fits to the spectrum. From the peak areas, we determine the exciton content $|X|^2 = 0.7$. The lower polariton amplitude is $\eta_c = 0.24$.

between the laser pulse and the LP line $\eta_s = 0.57$. We show normalized white light reflectivity in Fig. 5.7 as function of cavity energy (position on the sample). The measurement was taken in linear polarization, so that two branches are visible for the lower polariton. In the line-cut, the upper polariton does not display a resolved polarization splitting due to its high cavity content. Based on this data, we also estimate the exciton content $|X|^2 = 0.7$ and the coupling efficiency into the LP mode $\eta_c = 0.24$, from Lorentzian fits in Fig. 5.7(b) to the relevant detuning marked by the red dashed line. Knowing the laser power impinging on the sample surface, we can estimate

$$N = \eta_s \eta_c n_{\text{ph}},$$

where $n_{\text{ph}} = p_{\text{cw}} / (\hbar \omega_L f_{\text{rep}})$ is the photon number per pulse, p_{cw} is the average input power, $f_{\text{rep}} = 76$ MHz is the pulse repetition rate and ω_L is the laser center frequency.

To model the time-resolved experiment described above, we use a single

⁵For $B = 10$ T, we do not expect the magnetic field to strongly influence the strength of exciton-exciton interactions since the exciton Bohr radius is still of the same order as the magnetic length.

5. Polariton Interactions in the Fractional Quantum Hall Regime

mode Gross-Pitaevskii equation for the lower polariton wave function:

$$\frac{d\psi(t)}{dt} = -\frac{\gamma}{2}\psi(t) - ig|\psi(t)|^2\psi(t) + F(t, \tau, t_{\text{mod}}), \quad (5.2)$$

where g is the nonlinearity and $\gamma = 0.1 \text{ ps}^{-1}$ is inherited from the cavity decay rate. The (modulated) drive term reads:

$$F(t, \tau, t_{\text{mod}}) = A_1(t_{\text{mod}})G(t) + A_2G(t - \tau)e^{i\omega_L\tau},$$

where $G(t)$ and $G(t - \tau)$ are 4 ps FWHM Gaussian envelopes delayed by τ , A_1 is the (modulated) amplitude of the first pulse and A_2 the (constant) amplitude of the delayed pulse. In the simulation, we adjust the pulse amplitudes A_1 and A_2 to match the intra-cavity polariton number N we estimated in the previous paragraph. The pulse intensities, averaged over a modulation cycle, are chosen to be equal, as was the case for the experiments. Of course there is only one physical time axis t , but we introduced a separate variable t_{mod} for numerical convenience. Because of the large separation between timescales $1/f_{\text{rep}} \ll 1/f_{\text{mod}}$, we can consider $t_{\text{mod}} = \text{const.}$ for each individual pulse.

We calculate the solution $\psi(t)$ for every τ and we repeat this procedure for different values of $A_1(t_{\text{mod}}) = \sqrt{I_1} \sin(\omega_m t_{\text{mod}})$, thus simulating the experimental procedure (time-resolved four-wave mixing). We then Fourier transform $\psi(t)$ to obtain the calculated Fourier spectrum $\mathcal{I}_{\text{model}}(\omega, \tau)$ that we directly compare to the experiment as shown in Fig. 5.8. The top row shows the linear response at ω_m , the bottom row the nonlinear response at $3\omega_m$, both evaluated for increasing input powers towards the right. In the end, the simulation includes only two free parameters: the interaction strength g and a global scaling factor ϕ that accounts for the finite detection efficiency in our experiment $\mathcal{I}(\omega, \tau) = \phi \mathcal{I}_{\text{model}}(\omega, \tau)$, where ϕ is common to all values of ω and τ . We determine the parameter ϕ by fitting $\mathcal{I}_{\text{model}}(\omega = \omega_m, \tau)$ to our experiments. Then, we obtain g by adjusting $\mathcal{I}_{\text{model}}(\omega = 3\omega_m, \tau)$ to best reproduce our measurements. Note that, given the estimate of $N = |\psi|^2 \propto \mathcal{I}(\omega_m, \tau)$, the information about g is contained in the ratio of $\mathcal{I}(3\omega_m, \tau)/\mathcal{I}(\omega_m, \tau)$, where ϕ drops out.

We show, in Fig. 5.8, the results of our fit, which yields a value of $g = 0.54 \pm 0.08 \text{ } \mu\text{eV}$ for the polariton interaction strength (accounting for statistical errors only, s.d.). To convert this single mode interaction energy into a 2D

polariton-polariton interaction constant U_p , we multiply g by the polariton mode area A : $U_p = A \times g$. Based on the numerical aperture of our objective NA = 0.15, we expect the excitation beam to extend over $A = 11 \mu\text{m}^2$, which results in $U = 6.2 \mu\text{eV} \mu\text{m}^2$. Finally, we estimate the exciton-exciton interaction strength by dividing U_p by the exciton content squared:

$$U_x = A \cdot g / |X|^4 = 12.5_{-2}^{+2(18)} \mu\text{eV} \mu\text{m}^2 \quad (5.3)$$

This result is compatible with other values reported in the literature [11, 31, 32, 47, 48, 231, 235, 247, 248]. The largest sources of errors on the measurement of U_x originate from the estimate of N and A which are subject to large systematic errors (given in parentheses). Our estimate of N could indeed easily be off by a factor of two. Additionally, our estimate of A might deviate from the spot size estimate due to polariton diffusion and will eventually be modified by the exciton-exciton interactions. Altogether, this leads to the error estimate of Eq. (5.3). We observe a small deviation in the power dependence between experiment and fit. This discrepancy is due to a systematic calibration error of the input power which also led to the observed deviation in the slopes measured in Fig. 5.4(c). However, the resulting systematic error on g is small compared to the first two contributions. We expect our measurement technique to give more accurate results in experimental geometries that allow imaging the polariton cloud in real-space and measuring in transmission. This would lift the constraint of cross-polarization between incident and detected light and allow for additional separation of nonlinear terms according to emission angle.

5.2.3 Interaction Strength in FQH States

By estimating the polariton occupation number N and analysis of the FWM signal for exciton-exciton interactions, we were able to benchmark the measurement technique in absolute terms. The agreement between the experiments and the model, as well as obtaining the expected strength of exciton-exciton interactions validates our approach. We now return to the interaction strength in the FQH regime. Applying the same analysis to the nonlinear

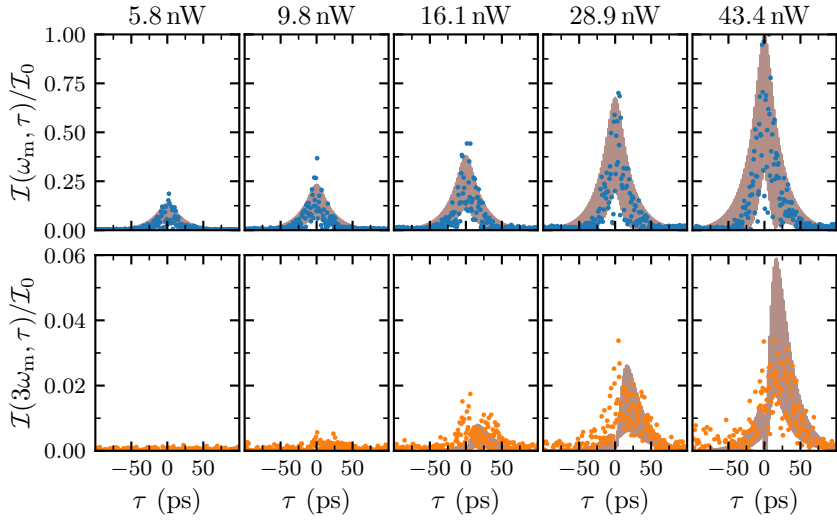


Figure 5.8: Comparing FWM data to GPE predictions for an intrinsic QW. Top row: comparison between the measured (blue circles) and calculated (shaded area) $\mathcal{I}(\omega_m, \tau)$ for different input powers, used to calibrate the detection efficiency ϕ . Bottom row: comparison between the measured (orange circles) and calculated (shaded area) $\mathcal{I}(3\omega_m, \tau)$ for different input powers, yields a value of $g = 0.54 \mu\text{eV}$ for the polariton interaction strength.

signal at $\nu = 2/5$ yields

$$U_p = 57_{-7}^{+7(80)} \mu\text{eV } \mu\text{m}^2, \quad (5.4)$$

where the first uncertainty is statistical (s.d.) and the second (in parenthesis), is our best estimate of systematic errors stemming from our estimation of the polariton number and mode area. We note again that, while the absolute measurement of U_p is susceptible to large systematic errors, the relative variation of U_p is only susceptible to statistical errors.

Although our model reproduces the delay-time-dependence of our measurements for the neutral QW, the observed response close to fractional filling factors is not fully captured by this description in terms of a Kerr nonlinearity, as is evident from Fig. 5.9. While the signal at ω_m matches to the experiment (top row), the nonlinear part at $3\omega_m$ (bottom row) deviates. Most notably, although the mean-field model predicts that $\mathcal{I}(3\omega_m, \tau)$ only takes large values for positive delays (see $\mathcal{I}(3\omega_m, \tau)$ in Fig. 5.8, we observe, in the fractional quantum Hall polariton case, that $\mathcal{I}(3\omega_m, \tau)$ is symmetric about $\tau = 0$ and thus takes large values for negative delays as well (see for example the symmetric shape of $\mathcal{I}(3\omega_m, \tau)$ in Fig. 5.4(b) above). To obtain a quantitative estimate of the interaction constant of fractional quantum Hall polaritons that we can compare to the value obtained for exciton polaritons in a neutral quantum well, we therefore apply the procedure described in the previous paragraph (measurement and model of exciton-polariton interactions), where we restrict the fit to the signal observed at positive delays.

This remark notwithstanding, we repeat the steps described above to give a first estimate of the interaction constant. The lifetime was adjusted to $\gamma = 16$ ps to account for the observed narrowing of the linewidth. We find that interactions are enhanced by a factor 4.6 ± 0.9 in the 2DES sample as compared to the neutral QW sample. For estimating the relative enhancement of interactions, note that the only relevant error bar is statistical ($U = 57 \pm 7 \mu\text{eV } \mu\text{m}^2$) since the systematic error affects all the measurements the same way. We emphasize that the measured LP_{σ^-} linewidth at $\nu = 2/5$, $\gamma \simeq 67 \pm 5 \mu\text{eV}$, is comparable to linewidths used in recent state of the art experiments [31, 32]. The lower polariton matter content and linewidth were extracted from Fig. 5.2(b). Finally, the same analysis is repeated once more for the case $\nu = 2/3$.

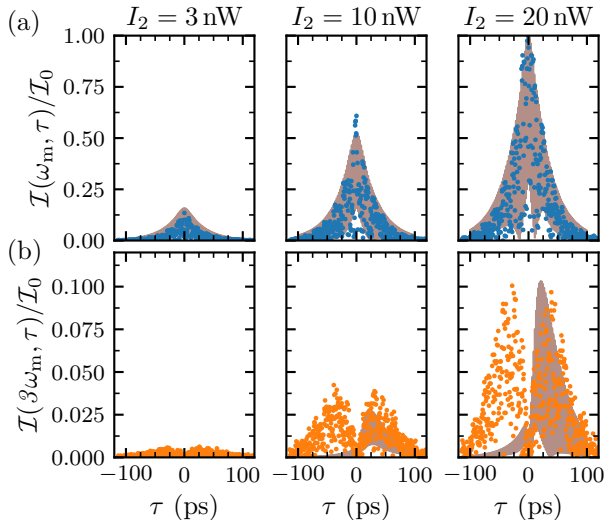


Figure 5.9: Estimation of the polariton interaction constant at $2/5$. Comparison of the linear $\mathcal{I}(\omega_m, \tau)$ (top row, blue circles) and nonlinear response $\mathcal{I}(3\omega_m, \tau)$ (bottom row, orange circles) at $\nu = 2/5$ with the GPE model (gray).

The results for all of our measurements of U are summarized in Table 5.1 for the 2DEG sample at different filling factors as well as for the undoped sample. In the table, we only provide the statistical error bars that are relevant to compare relative variations of U between columns of the Table. At $\nu = 2/5$, we observe that interactions are enhanced by more than an order of magnitude as compared to a neighboring filling factor (taken at $B = 3.0$ T). This is consistent with our estimation of the enhancement of interaction based on measuring the area of $\mathcal{I}(3\omega_m, \tau)$. Compared to the undoped QW, we find that U is increased by a factor 4.6 ± 0.9 at $\nu = 2/5$. This result indicates that away from $\nu = 2/5$ and $\nu = 2/3$, polaron-polariton interactions may be reduced as compared to exciton-polaritons in the neutral quantum well. Nevertheless, in the $\nu = 2/5$ case, the ratio $U/(A\gamma)$ approaches unity (for $A = 1 \mu\text{m}^2$), which indicates that polariton blockade is within reach.

We conclude by discussing a possible objection to our claims based on changes in detuning between the cavity and attractive polaron resonances. Since polaritons interact through their matter part, a change in the attractive

Parameter	Undoped	2DES	2DES	2DES
	QW	$\nu = 2/3$	$\nu = 2/5$	$B = 3 \text{ T}$
U ($\mu\text{eV } \mu\text{m}^2$)	12.5 ± 2	38 ± 4	57 ± 7	≤ 4.5
γ (μeV)	300 ± 30	87 ± 4	67 ± 5	97 ± 4
N (nW^{-1})	7.5 ± 1	3.6 ± 0.3	2.2 ± 0.3	3.3 ± 0.4

Table 5.1: Summary of the estimated interaction constants and fitted linewidths for the undoped and 2DES experiments. The polariton number N is estimated as described in Section 5.2.2 given per cw-equivalent laser excitation power. The quoted error bars are statistical (1 s.d.).

polaron content of the polaritons as a function of B would also lead to a modification of polariton-polariton interactions: polaritons with a higher polaron content will indeed show larger interactions⁶. Therefore, for $\nu = 2/5$, we may ask if part of the enhancement of the nonlinear signal, presented in Fig. 5.5, could be due to variations in the matter content of LP as we vary the magnetic field. This is in fact not the case as we demonstrate in the following. Our estimation of the enhancement of the nonlinearity is based on a comparison of the quantity $R_a = \langle \mathcal{I}(3\omega_m, \tau) \rangle_\tau / \langle \mathcal{I}(\omega_m, \tau) \rangle_\tau$ for different values of ν . We note that R_a is proportional to $U_p N$, where N is the injected number of lower polaritons. For a pulsed excitation experiment where the pulse spectral width is larger than the polariton linewidth, N is proportional to the LP photonic content $|C|^2 = 1 - |X|^2$. Therefore, the nonlinear signal R_a is proportional to $UN \propto |X|^4(1 - |X|^2)$, which reaches its maximum for $|X|^2 = 2/3$. In the specific case of $\nu = 2/5$, the lower polariton becomes more matter-like at $B = 3.15 \text{ T}$ ($|X|^2 = 0.88$) than it is at $B = 3 \text{ T}$ ($|X|^2 = 0.8$). Because $|X|^4(1 - |X|^2)$ is a decreasing function of $|X|^2$ for $|X|^2 > 2/3$, it turns out the observed change in matter component by itself cannot explain the measured increase of R_a . Equivalently, if U_p had remained constant as we increased the field from $B = 3 \text{ T}$ to $B = 3.15 \text{ T}$, we

⁶Recent T-matrix calculations actually suggest that polariton interactions may exceed exciton interactions in certain conditions [249, Chapter 2], which is beyond the simple picture $U_p = |X|^4 U_x$ we introduced earlier.

would have observed a reduction of R_a . As a result, we conclude that our estimation of the enhancement of U based on the evolution of R_a around $\nu = 2/5$ is conservative and that we may be underestimating the increase of U_p by not taking into account the changes in $|X|^2$.

5.2.4 Increase of Polariton Coherence Time

We have observed, in Fig. 5.5(b), an interesting evolution of the (mostly linear) term $\mathcal{I}(\omega_m, \tau)$ as we tune B : the characteristic decay time of $\mathcal{I}(\omega_m, \tau)$ (i.e. the polariton coherence time T_{LP}) increases for $\nu = 2/3$ and $\nu = 2/5$. We present, in this section, a detailed study of this effect versus input pump power. We show, in Fig. 5.10(a), a semi-log plot of a typical delay trace $\mathcal{I}(\omega_m, \tau)$ (green). To extract T_{LP} , we fit the envelope of this trace by a double exponential decay (black line): T_{LP} is directly given by the exponential decay time. In the following Figs. 5.10(b) to 5.10(d), we plot the fitted values of T_{LP} as a function of input pump power around filling factors $\nu = 1, 2/3, 2/5$. In every panel, we show a data set recorded when B is tuned to the corresponding quantum Hall states (blue points), and another data set recorded at a slightly different filling factor (orange points).

At exactly $\nu = 2/3$ and $\nu = 2/5$, we observe that T_{LP} first increases sharply and then stabilizes at a value two to three times larger to its low-power value. This increase of T_{LP} coincides with the enhancement (and high power saturation) of the nonlinearity at filling factors $\nu = 2/3$ and $\nu = 2/5$ discussed above. In stark contrast, slightly away from these filling factors, as well as for $\nu = 1$, T_{LP} stays relatively stable around its low power value. In another set of experiments, we extracted T_{LP} by measuring the Lorentzian width of $LP_{\sigma-}$ in white light reflectivity spectra as a function of input power; this study (not shown here) led to the same observations. These results suggest a nonlinear behavior of $\mathcal{I}(\omega_m, \tau)$ at fractional filling factors. However, monitoring the average value $\langle \mathcal{I}(\omega_m, \tau) \rangle_{\tau}$ versus power (particularly evident in Fig. 5.4(c)) shows that $\langle \mathcal{I}(\omega_m, \tau) \rangle_{\tau}$ remains linear in excitation power. At this stage, the origin of this power dependent enhancement of T_{LP} thus remains unknown. While the measured increase in nonlinearity is clearly an advantage for implementing strongly interacting polaritons, it is unclear whether the observed (high power) increased coherence time and thus decreased linewidth could also be beneficial for realizing polariton blockade. This is due to limitations

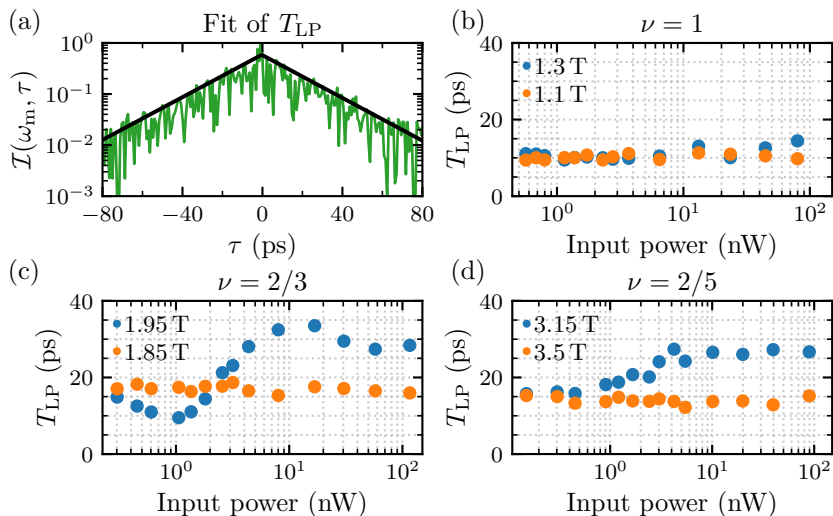


Figure 5.10: Increase in polariton coherence time T_{LP} with input power at fractional quantum Hall states. (a) Extraction of T_{LP} , showing an exemplary linear response in a logarithmic plot with the fit to the envelope in green. The inverse slope corresponds to T_{LP} . (b-d) Dependence of T_{LP} on input power for the filling factors $\nu = 1$, $\nu = 2/3$ and $\nu = 2/5$. Blue circles correspond to the magnetic field at the quantum Hall state, orange circles to a magnetic field nearby.

on the photon number, which might constrain such an experiment to input powers below a few nanowatts [30]. We remark that the enhanced coherence time was also reproduced on sample B, shown in Fig. 5.6(b). Despite these comments, the observed increase in coherence time has its merits. One would expect a decrease in polariton coherence time with increased pump power due to accumulation of excitons and charge carriers [250]. The fact that the coherence time is not decreasing at these input powers is encouraging for future experiments, and is consistent with the fact that we observe narrow LP linewidths even with large attractive polaron contents.

5.3 Conclusion and Perspectives

We demonstrated an increased nonlinear optical response at FQH states $\nu = 2/5$ and $\nu = 2/3$. Strong enhancement of polariton-polariton inter-

actions around FQHE states opens up new perspectives for the study of strongly correlated electron as well as for photonic systems. Our experiments show that despite their qualitatively similar linear optical response, fractional and integer QH states show strikingly different nonlinear optical signatures: this suggests that nonlinear spectroscopy could reveal signatures of strongly correlated electronic systems that are not accessible by linear optical or transport measurements. Understanding the physical mechanism for enhanced nonlinear response and prolonged polariton coherence times for FQHE states constitutes an interesting problem for future studies.

Embedding our sample in a zero-dimensional cavity with a mode area of $A = 1 \mu\text{m}^2$ would yield $U_p/(A\gamma) = 0.85$, which indicates that polariton blockade regime is within reach. Since GaAs is the material of choice for high quality 2DEGs, the GaAs substrate should be removed to allow for optical transmission experiments [128]. The substrate could be replaced by a dielectric mirror which would improve the cavity quality considerably. For confinement into zero dimensions, a dimpled fiber cavity could be used [251]. However, due to increased vibration noise in a dilution refrigerator compared to a helium bath at 4 K, it might be desirable to give up mechanical degrees of freedom for cavity alignment and tunability in exchange for a more robust cavity design to ensure stable cavity operation [252–255]. In addition to prospects for realizing antibunched single photon emission, improving on previous works [31, 32], we envision photon correlation measurements as a promising spectroscopic tool for investigating electronic phase transitions between different quantum Hall states.

Chapter Summary and Outlook

6

In this dissertation, we studied a unique combination of photonic and electronic systems. An optical cavity was resonantly coupled to excitations of a 2D electron gas, and together they were subjected to millikelvin temperatures and external magnetic fields. This opened up experimental studies of one of the most fascinating strongly correlated electronic systems discovered to date, the quantum Hall regime of a two-dimensional electron gas. Furthermore, special heterostructure design and reaching the strong coupling regime of cavity QED allowed for the hybridization of photons with many-body polaron excitations in the 2DEG to form a sensitive optical probe. Thanks to said hybridization, this platform allows for non-perturbative control of polaritons, and thereby photons, simply by tailoring the polaron part of the wave function. This feature takes polaron-polaritons beyond a tool to study the quantum Hall effect—but enables engineering of novel photonic devices by making use of well-developed technologies to control electronic systems.

Polaron-polaritons are collective excitations of excitons dressed by Fermi sea electron-hole pairs. The cavity character ensures further delocalization in space over micrometer length scales. Via their polaron component, these particles remain sensitive to the surrounding electron gas. We identified jumps in the Fermi energy connected with transitions between quantum Hall states and found discontinuities related to the incompressible nature of the electrons at particular fillings. Through careful sample design, protecting the donor impurities from optical illumination, perturbations of the electron density by the probe were minimized compared to earlier devices. Polarization selective polariton spectroscopy reveals the electronic spin polarization. We studied skyrmion spin textures in the vicinity of the $\nu = 1$ quantum Hall ferromagnet by measuring the evolution of the spin polarization as function of ν . We an-

6. Summary and Outlook

alyzed the question whether it is possible to move neutral optical excitations with electric and magnetic fields in the context of polaron-polaritons. We found that tailoring electron density profiles directly exerts in-plane forces on the immersed polaritons. Hence, the transport of polaritons could be achieved via the much easier task of controlling the charge carrying electrons, which readily respond to the external fields. Extending this idea to spin polarized electrons yields polariton polarization control, allowing us to exert spin-selective forces on polaritons. Finally, we turned our attention to the problem of polariton-polariton interactions. It is an ongoing challenge to increase such interactions, because they remain too weak to realize strong single photon interactions. Achieving this task could lead to a new type of high repetition rate single photon source based on polariton blockade while at the same time realizing the building block for an optical analog computing and quantum simulation platform. We observed an enhanced nonlinear response from polaron-polaritons when coupled to fractional quantum Hall states $\nu = 2/5$ and $\nu = 2/3$. This suggests enhanced effective photon-photon interactions. Our findings demonstrate the prospects of this avenue to progress towards stronger interactions: instead of relying on ever increasing optical and excitonic confinement—to tailoring the exciton or polaron into more exotic complexes that increase the bare interaction strength.

There are limitations to our work that simultaneously highlight fruitful areas for further advancements. We discussed how our sample layout faces a trade-off between optical and electronic transport qualities. While the doping quantum well design minimizes the impact of undesired impurity ionization, they inhibited electronic transport experiments by providing parallel channels for the current to flow. This limitation could be overcome by patterning additional gate structures to selectively deplete the DQWs (see e.g. [228]) and hence improve the transport properties, without compromising the optical properties of the device. While we achieved polariton acceleration via density control of the 2DEG, other proposed mechanisms could be investigated which are of both practical and fundamental interest, such as polaron transconductivity [207], polariton transport via Coulomb drag [202–204] or the complementary effect of photon drag [256]. An exciting goal consists of the realization of artificial gauge fields for polaritons [28, 194, 257], with potential applications for analog (quantum) simulation with polaritons [12, 13] and creating topological [191] and correlated states of light [25, 29, 258, 259].

We expect such studies to advance the understanding of optical excitations in doped semiconductors and their interactions, which is a topic of current interest [84, 85, 87, 88, 91].

The most important challenge to advance quantum simulation based on polaritons, and optical systems in general, lies in realizing an effective single photon nonlinearity [4]. The strength of interactions has to be compared with the photon bandwidth, hence a significant step forward could be achieved by improving the microcavity quality [112, 260], preferably by replacing the MBE grown DBR stacks altogether. This would entail multiple benefits, besides reduced loss and higher reflectivity dielectric coatings for the cavity. The 2DEG quality in terms of mobility (and observable fractional states) is an order of magnitude lower for our structures compared to optimized 2DEGs from the very same growth chamber, capable of realizing state-of-the-art 2DEGs. Furthermore, the 2DEG being buried deeply from the surface, below the top DBR stack, is a hindrance when it comes to processing and gating the devices—especially on short length scales relevant for exotic quasiparticle braiding [22, 186, 187]. Another step into this direction might require the spatial separation of the 2DEG and the optical probe and control into separate quantum wells to further reduce the perturbation induced by optical pumping. In the context of tunneling spectroscopy, the idea of a remote probing quantum well was applied with great success [261, 262]. Exploring exciton-polariton mediated superconductivity of 2D electrons remains an outstanding goal [263, 264]. We conclude by mentioning that all our ideas could find a natural implementation with 2D van-der-Waals materials as alternative to the GaAs platform. Semiconducting layers providing optoelectronic functionality [265] can readily be integrated with graphene hosting the quantum Hall effect [266–268] and other correlated states [269, 270], creating a rich playground for further study at the interplay between photonics, light-matter coupling and strongly correlated electrons.

Bibliography

- [1] M. A. Nielsen and I. L. Chuang, *Quantum Computation and Quantum Information* (Cambridge University Press, Cambridge, 2010).
- [2] R. P. Feynman, “Simulating physics with computers”, *Int. J. Theor. Phys.* **21**, 467–488 (1982).
- [3] A. Aspuru-Guzik and P. Walther, “Photonic quantum simulators”, *Nat. Phys.* **8**, 285–291 (2012).
- [4] M. J. Hartmann, “Quantum simulation with interacting photons”, *J. Opt.* **18**, 104005 (2016).
- [5] E. Urban, T. A. Johnson, T. Henage, L. Isenhower, D. D. Yavuz, T. G. Walker, and M. Saffman, “Observation of Rydberg blockade between two atoms”, *Nature Phys* **5**, 110–114 (2009).
- [6] A. Gaëtan, Y. Miroshnychenko, T. Wilk, A. Chotia, M. Viteau, D. Comparat, P. Pillet, A. Browaeys, and P. Grangier, “Observation of collective excitation of two individual atoms in the Rydberg blockade regime”, *Nature Phys* **5**, 115–118 (2009).
- [7] N. Jia, N. Schine, A. Georgakopoulos, A. Ryou, L. W. Clark, A. Sommer, and J. Simon, “A strongly interacting polaritonic quantum dot”, *Nat. Phys.* **14**, 550–554 (2018).
- [8] H. Deng, H. Haug, and Y. Yamamoto, “Exciton-polariton Bose-Einstein condensation”, *Rev. Mod. Phys.* **82**, 1489–1537 (2010).
- [9] I. Carusotto and C. Ciuti, “Quantum fluids of light”, *Rev. Mod. Phys.* **85**, 299–366 (2013).

- [10] J. Kasprzak, M. Richard, S. Kundermann, A. Baas, P. Jeambrun, J. M. J. Keeling, F. M. Marchetti, M. H. Szymańska, R. André, J. L. Staehli, V. Savona, P. B. Littlewood, B. Deveaud, and L. S. Dang, “Bose–Einstein condensation of exciton polaritons”, *Nature* **443**, 409–414 (2006).
- [11] A. Amo, J. Lefrère, S. Pigeon, C. Adrados, C. Ciuti, I. Carusotto, R. Houdré, E. Giacobino, and A. Bramati, “Superfluidity of polaritons in semiconductor microcavities”, *Nat. Phys.* **5**, 805–810 (2009).
- [12] A. Amo and J. Bloch, “Exciton-polaritons in lattices: A non-linear photonic simulator”, *Comptes Rendus Physique, Polariton Physics / Physique Des Polaritons* **17**, 934–945 (2016).
- [13] N. G. Berloff, M. Silva, K. Kalinin, A. Askitopoulos, J. D. Töpfer, P. Cilibrizzi, W. Langbein, and P. G. Lagoudakis, “Realizing the classical XY Hamiltonian in polariton simulators”, *Nature Mater* **16**, 1120–1126 (2017).
- [14] D. G. Angelakis, ed., *Quantum Simulations with Photons and Polaritons*, Quantum Science and Technology (Springer, Cham, 2017).
- [15] T. Boulier, M. J. Jacquet, A. Maître, G. Lerario, F. Claude, S. Pigeon, Q. Glorieux, A. Amo, J. Bloch, A. Bramati, and E. Giacobino, “Microcavity Polaritons for Quantum Simulation”, *Adv. Quantum Technol.* **3**, 2000052 (2020).
- [16] S. Ghosh and T. C. H. Liew, “Quantum computing with exciton-polariton condensates”, *npj Quantum Inf* **6**, 1–6 (2020).
- [17] D. Sanvitto and S. Kéna-Cohen, “The road towards polaritonic devices”, *Nat. Mater.* **15**, 1061–1073 (2016).
- [18] C. Schneider, K. Winkler, M. D. Fraser, M. Kamp, Y. Yamamoto, E. A. Ostrovskaya, and S. Höfling, “Exciton-polariton trapping and potential landscape engineering”, *Rep. Prog. Phys.* **80**, 016503 (2017).
- [19] S. Smolka, W. Wuester, F. Haupt, S. Faelt, W. Wegscheider, and A. Imamoglu, “Cavity quantum electrodynamics with many-body states of a two-dimensional electron gas”, *Science* **346**, 332–335 (2014).

-
- [20] M. Koschorreck, D. Pertot, E. Vogt, B. Fröhlich, M. Feld, and M. Köhl, “Attractive and repulsive Fermi polarons in two dimensions”, *Nature* **485**, 619–622 (2012).
- [21] M. Sidler, P. Back, O. Cotlet, A. Srivastava, T. Fink, M. Kroner, E. Demler, and A. Imamoglu, “Fermi polaron-polaritons in charge-tunable atomically thin semiconductors”, *Nature Phys* **13**, 255–261 (2017).
- [22] C. Nayak, S. H. Simon, A. Stern, M. Freedman, and S. Das Sarma, “Non-Abelian anyons and topological quantum computation”, *Rev. Mod. Phys.* **80**, 1083–1159 (2008).
- [23] F. Grusdt, N. Y. Yao, D. Abanin, M. Fleischhauer, and E. Demler, “Interferometric measurements of many-body topological invariants using mobile impurities”, *Nat. Commun.* **7**, 11994 (2016).
- [24] A. Muñoz de las Heras, E. Macaluso, and I. Carusotto, “Anyonic Molecules in Atomic Fractional Quantum Hall Liquids: A Quantitative Probe of Fractional Charge and Anyonic Statistics”, *Phys. Rev. X* **10**, 041058 (2020).
- [25] R. O. Umucalılar and I. Carusotto, “Fractional Quantum Hall States of Photons in an Array of Dissipative Coupled Cavities”, *Phys. Rev. Lett.* **108**, 206809 (2012).
- [26] M. Hafezi, M. D. Lukin, and J. M. Taylor, “Non-equilibrium fractional quantum Hall state of light”, *New J. Phys.* **15**, 063001 (2013).
- [27] L. W. Clark, N. Schine, C. Baum, N. Jia, and J. Simon, “Observation of Laughlin states made of light”, *Nature* **582**, 41–45 (2020).
- [28] M. Aidelsburger, S. Nascimbene, and N. Goldman, “Artificial gauge fields in materials and engineered systems”, *Comptes Rendus Physique, Quantum Simulation / Simulation Quantique* **19**, 394–432 (2018).
- [29] A. Imamoglu, H. Schmidt, G. Woods, and M. Deutsch, “Strongly Interacting Photons in a Nonlinear Cavity”, *Phys. Rev. Lett.* **79**, 1467–1470 (1997).
- [30] A. Verger, C. Ciuti, and I. Carusotto, “Polariton quantum blockade in a photonic dot”, *Phys. Rev. B* **73**, 193306 (2006).

- [31] G. Muñoz-Matutano, A. Wood, M. Johnsson, X. Vidal, B. Q. Baragiola, A. Reinhard, A. Lemaître, J. Bloch, A. Amo, G. Nogues, B. Besga, M. Richard, and T. Volz, “Emergence of quantum correlations from interacting fibre-cavity polaritons”, *Nat. Mater.* **18**, 213 (2019).
- [32] A. Delteil, T. Fink, A. Schade, S. Höfling, C. Schneider, and A. İmamoglu, “Towards polariton blockade of confined exciton–polaritons”, *Nat. Mater.* **18**, 219 (2019).
- [33] L. Jacak, P. Sitko, K. Wieczorek, and A. Wójs, *Quantum Hall systems: Braid groups, composite fermions and fractional charge* (Oxford University Press, New York, 2003).
- [34] M. O. Goerbig, *Quantum Hall Effects*, (2009) [arXiv:0909.1998 \[cond-mat\]](#).
- [35] J. Klaers, J. Schmitt, F. Vewinger, and M. Weitz, “Bose–Einstein condensation of photons in an optical microcavity”, *Nature* **468**, 545–548 (2010).
- [36] M. E. Levinstein and S. L. Rumyantsev, “GALLIUM ARSENIDE (GaAs)”, in *Handbook Series on Semiconductor Parameters* (World Scientific, 1996), pp. 77–103.
- [37] Y. A. Goldberg, “ALUMINIUM GALLIUM ARSENIDE ($\text{Al}_x\text{Ga}_{1-x}\text{As}$)”, in *Handbook Series on Semiconductor Parameters* (World Scientific, 1996), pp. 1–36.
- [38] S. Gehrsitz, F. K. Reinhart, C. Gourgon, N. Herres, A. Vonlanthen, and H. Sigg, “The refractive index of $\text{Al}_x\text{Ga}_{1-x}\text{As}$ below the band gap: Accurate determination and empirical modeling”, *Journal of Applied Physics* **87**, 7825–7837 (2000).
- [39] J. R. Chelikowsky and M. L. Cohen, “Nonlocal pseudopotential calculations for the electronic structure of eleven diamond and zinc-blende semiconductors”, *Phys. Rev. B* **14**, 556–582 (1976).
- [40] T. Ihn, *Semiconductor nanostructures: quantum states and electronic transport* (Oxford University Press, New York, 2010).
- [41] I. Vurgaftman, J. R. Meyer, and L. R. Ram-Mohan, “Band parameters for III–V compound semiconductors and their alloys”, *Journal of Applied Physics* **89**, 5815–5875 (2001).

-
- [42] S. B. Nam, D. C. Reynolds, C. W. Litton, R. J. Almassy, T. C. Collins, and C. M. Wolfe, “Free-exciton energy spectrum in GaAs”, *Phys. Rev. B* **13**, 761–767 (1976).
- [43] M. S. Skolnick, T. A. Fisher, and D. M. Whittaker, “Strong coupling phenomena in quantum microcavity structures”, *Semicond. Sci. Technol.* **13**, 645–669 (1998).
- [44] S. Schmitt-Rink, D. S. Chemla, and D. A. B. Miller, “Linear and nonlinear optical properties of semiconductor quantum wells”, *Adv. Phys.* **38**, 89–188 (1989).
- [45] V. Savona, L. Andreani, P. Schwendimann, and A. Quattropani, “Quantum well excitons in semiconductor microcavities: Unified treatment of weak and strong coupling regimes”, *Solid State Communications* **93**, 733–739 (1995).
- [46] J. J. Hopfield, “Theory of the Contribution of Excitons to the Complex Dielectric Constant of Crystals”, *Phys. Rev.* **112**, 1555–1567 (1958).
- [47] C. Ciuti, V. Savona, C. Piermarocchi, A. Quattropani, and P. Schwendimann, “Role of the exchange of carriers in elastic exciton-exciton scattering in quantum wells”, *Phys. Rev. B* **58**, 7926–7933 (1998).
- [48] F. Tassone and Y. Yamamoto, “Exciton-exciton scattering dynamics in a semiconductor microcavity and stimulated scattering into polaritons”, *Phys. Rev. B* **59**, 10830–10842 (1999).
- [49] W. Schäfer and M. Wegener, *Semiconductor Optics and Transport Phenomena*, Advanced Texts in Physics (Springer-Verlag, Berlin Heidelberg, 2002).
- [50] K. v. Klitzing, G. Dorda, and M. Pepper, “New Method for High-Accuracy Determination of the Fine-Structure Constant Based on Quantized Hall Resistance”, *Phys. Rev. Lett.* **45**, 494–497 (1980).
- [51] D. C. Tsui, H. L. Stormer, and A. C. Gossard, “Two-Dimensional Magnetotransport in the Extreme Quantum Limit”, *Phys. Rev. Lett.* **48**, 1559–1562 (1982).
- [52] K. von Klitzing, “The quantized Hall effect”, *Rev. Mod. Phys.* **58**, 519–531 (1986).

- [53] H. L. Stormer, D. C. Tsui, and A. C. Gossard, “The fractional quantum Hall effect”, *Rev. Mod. Phys.* **71**, S298–S305 (1999).
- [54] R. Willett, J. P. Eisenstein, H. L. Störmer, D. C. Tsui, A. C. Gossard, and J. H. English, “Observation of an even-denominator quantum number in the fractional quantum Hall effect”, *Phys. Rev. Lett.* **59**, 1776–1779 (1987).
- [55] M. A. Lampert, “Mobile and Immobile Effective-Mass-Particle Complexes in Nonmetallic Solids”, *Phys. Rev. Lett.* **1**, 450–453 (1958).
- [56] K. Kheng, R. T. Cox, M. Y. d’Aubigné, F. Bassani, K. Saminadayar, and S. Tatarenko, “Observation of negatively charged excitons X^- in semiconductor quantum”, *Phys. Rev. Lett.* **71**, 1752–1755 (1993).
- [57] G. Finkelstein, H. Shtrikman, and I. Bar-Joseph, “Optical Spectroscopy of a Two-Dimensional Electron Gas near the Metal-Insulator Transition”, *Phys. Rev. Lett.* **74**, 976–979 (1995).
- [58] A. J. Shields, M. Pepper, M. Y. Simmons, and D. A. Ritchie, “Spin-triplet negatively charged excitons in GaAs quantum wells”, *Phys. Rev. B* **52**, 7841–7844 (1995).
- [59] I. Bar-Joseph, “Trions in GaAs quantum wells”, *Semicond. Sci. Technol.* **20**, R29 (2005).
- [60] D. Andronikov, V. Kochereshko, A. Platonov, T. Barrick, S. A. Crooker, and G. Karczewski, “Singlet and triplet trion states in high magnetic fields: Photoluminescence and reflectivity spectra of modulation-doped CdTe/Cd_{0.7}Mg_{0.3}Te quantum wells”, *Phys. Rev. B* **72**, 165339 (2005).
- [61] G. D. Mahan, “Excitons in Degenerate Semiconductors”, *Phys. Rev.* **153**, 882–889 (1967).
- [62] P. Hawrylak, “Optical properties of a two-dimensional electron gas: Evolution of spectra from excitons to Fermi-edge singularities”, *Phys. Rev. B* **44**, 3821–3828 (1991).
- [63] T. Brunhes, R. André, A. Arnoult, J. Cibert, and A. Wasiela, “Oscillator strength transfer from X to X^+ in a CdTe quantum-well microcavity”, *Phys. Rev. B* **60**, 11568–11571 (1999).

-
- [64] R. Rapaport, R. Harel, E. Cohen, A. Ron, E. Linder, and L. N. Pfeiffer, “Negatively Charged Quantum Well Polaritons in a GaAs/AlAs Microcavity: An Analog of Atoms in a Cavity”, *Phys. Rev. Lett.* **84**, 1607–1610 (2000).
- [65] R. Rapaport, E. Cohen, A. Ron, E. Linder, and L. N. Pfeiffer, “Negatively charged polaritons in a semiconductor microcavity”, *Phys. Rev. B* **63**, 235310 (2001).
- [66] G. Malpuech, A. Kavokin, A. Di Carlo, and J. J. Baumberg, “Polariton lasing by exciton-electron scattering in semiconductor microcavities”, *Phys. Rev. B* **65**, 153310 (2002).
- [67] P. G. Lagoudakis, M. D. Martin, J. J. Baumberg, A. Qarry, E. Cohen, and L. N. Pfeiffer, “Electron-Polariton Scattering in Semiconductor Microcavities”, *Phys. Rev. Lett.* **90**, 206401 (2003).
- [68] A. Qarry, G. Ramon, R. Rapaport, E. Cohen, A. Ron, A. Mann, E. Linder, and L. N. Pfeiffer, “Nonlinear emission due to electron-polariton scattering in a semiconductor microcavity”, *Phys. Rev. B* **67**, 115320 (2003).
- [69] M. Perrin, P. Senellart, A. Lemaître, and J. Bloch, “Polariton relaxation in semiconductor microcavities: Efficiency of electron-polariton scattering”, *Phys. Rev. B* **72**, 075340 (2005).
- [70] A. Gabbay, Y. Preezant, E. Cohen, B. M. Ashkinadze, and L. N. Pfeiffer, “Fermi Edge Polaritons in a Microcavity Containing a High Density Two-Dimensional Electron Gas”, *Phys. Rev. Lett.* **99**, 157402 (2007).
- [71] N. S. Averkiev and M. M. Glazov, “Light-matter interaction in doped microcavities”, *Phys. Rev. B* **76**, 045320 (2007).
- [72] D. K. Efimkin and A. H. MacDonald, “Many-body theory of trion absorption features in two-dimensional semiconductors”, *Phys. Rev. B* **95**, 035417 (2017).
- [73] D. Pimenov, J. von Delft, L. Glazman, and M. Goldstein, “Fermi-edge exciton-polaritons in doped semiconductor microcavities with finite hole mass”, *Phys. Rev. B* **96**, 155310 (2017).

- [74] S. P. Rath and R. Schmidt, “Field-theoretical study of the Bose polaron”, *Phys. Rev. A* **88**, 053632 (2013).
- [75] M.-G. Hu, M. J. Van de Graaff, D. Kedar, J. P. Corson, E. A. Cornell, and D. S. Jin, “Bose Polarons in the Strongly Interacting Regime”, *Phys. Rev. Lett.* **117**, 055301 (2016).
- [76] N. B. Jørgensen, L. Wacker, K. T. Skalmstang, M. M. Parish, J. Levinsen, R. S. Christensen, G. M. Bruun, and J. J. Arlt, “Observation of Attractive and Repulsive Polarons in a Bose-Einstein Condensate”, *Phys. Rev. Lett.* **117**, 055302 (2016).
- [77] S. Giorgini, L. P. Pitaevskii, and S. Stringari, “Theory of ultracold atomic Fermi gases”, *Rev. Mod. Phys.* **80**, 1215–1274 (2008).
- [78] R. A. Suris, “Correlation Between Trion and Hole in Fermi Distribution in Process of Trion Photo-Excitation in Doped QWs”, in *Optical Properties of 2D Systems with Interacting Electrons*, edited by W. J. Ossau and R. Suris (Springer Netherlands, Dordrecht, 2003), pp. 111–124.
- [79] M. Combescot and J. Tribollet, “Trion oscillator strength”, *Solid State Communications* **128**, 273–277 (2003).
- [80] M. Combescot, J. Tribollet, G. Karczewski, F. Bernardot, C. Testelin, and M. Chamorro, “Many-body origin of the “trion line” in doped quantum wells”, *EPL* **71**, 431 (2005).
- [81] A. Schirotzek, C.-H. Wu, A. Sommer, and M. W. Zwierlein, “Observation of Fermi Polarons in a Tunable Fermi Liquid of Ultracold Atoms”, *Phys. Rev. Lett.* **102**, 230402 (2009).
- [82] R. Schmidt, T. Enss, V. Pietilä, and E. Demler, “Fermi polarons in two dimensions”, *Phys. Rev. A* **85**, 021602 (2012).
- [83] P. Massignan, M. Zaccanti, and G. M. Bruun, “Polarons, dressed molecules and itinerant ferromagnetism in ultracold Fermi gases”, *Rep. Prog. Phys.* **77**, 034401 (2014).
- [84] D. K. Efimkin and A. H. MacDonald, “Exciton-polarons in doped semiconductors in a strong magnetic field”, *Phys. Rev. B* **97**, 235432 (2018).

-
- [85] F. Rana, O. Koksals, and C. Manolatu, “Many-body theory of the optical conductivity of excitons and trions in two-dimensional materials”, *Phys. Rev. B* **102**, 085304 (2020).
- [86] F. Rana, O. Koksals, M. Jung, G. Shvets, and C. Manolatu, “Many-body theory of radiative lifetimes of exciton-trion superposition states in doped two-dimensional materials”, *Phys. Rev. B* **103**, 035424 (2021).
- [87] D. K. Efimkin, E. K. Laird, J. Levinsen, M. M. Parish, and A. H. MacDonald, “Electron-exciton interactions in the exciton-polaron problem”, *Phys. Rev. B* **103**, 075417 (2021).
- [88] A. Imamoglu, O. Cotlet, and R. Schmidt, “Exciton-polarons in two-dimensional semiconductors and the Tavis-Cummings model”, *Comptes Rendus Phys.*, 1–8 (2021).
- [89] D. C. Reynolds, K. K. Bajaj, C. W. Litton, P. W. Yu, W. T. Masselink, R. Fischer, and H. Morkoc, “Sharp-line photoluminescence spectra from GaAs-GaAlAs multiple-quantum-well structures”, *Phys. Rev. B* **29**, 7038–7041 (1984).
- [90] G. Eytan, Y. Yayan, M. Rappaport, H. Shtrikman, and I. Bar-Joseph, “Near-Field Spectroscopy of a Gated Electron Gas: A Direct Evidence for Electron Localization”, *Phys. Rev. Lett.* **81**, 1666–1669 (1998).
- [91] M. M. Glazov, “Optical properties of charged excitons in two-dimensional semiconductors”, *J. Chem. Phys.* **153**, 034703 (2020).
- [92] F. Chevy, “Universal phase diagram of a strongly interacting Fermi gas with unbalanced spin populations”, *Phys. Rev. A* **74**, 063628 (2006).
- [93] I. V. Kukushkin, K. von Klitzing, K. Ploog, V. E. Kirpichev, and B. N. Shepel, “Reduction of the electron density in GaAs-Al_xGa_{1-x}As single heterojunctions by continuous photoexcitation”, *Phys Rev B* **40**, 4179–4182 (1989).
- [94] B. B. Goldberg, D. Heiman, A. Pinczuk, L. Pfeiffer, and K. W. West, “Magneto-optics in the integer and fractional quantum Hall and electron solid regimes”, *Surf. Sci.* **263**, 9–17 (1992).

- [95] J. G. Groshaus, P. Plochocka-Polack, M. Rappaport, V. Umansky, I. Bar-Joseph, B. S. Dennis, L. N. Pfeiffer, K. W. West, Y. Gallais, and A. Pinczuk, “Absorption in the Fractional Quantum Hall Regime: Trion Dichroism and Spin Polarization”, *Phys. Rev. Lett.* **98**, 156803 (2007).
- [96] W. Wüster, “Cavity quantum electrodynamics with many-body states of a two-dimensional electron system”, Doctoral Thesis (ETH Zurich, 2015).
- [97] P. M. Mooney, “Deep donor levels (*DX* centers) in III-V semiconductors”, *Journal of Applied Physics* **67**, R1–R26 (1990).
- [98] M. Rother, *2D Schroedinger Poisson solver AQUILA*, 2010.
- [99] M. Lupatini, P. Knüppel, S. Faelt, R. Winkler, M. Shayegan, A. Imamoglu, and W. Wegscheider, “Spin Reversal of a Quantum Hall Ferromagnet at a Landau Level Crossing”, *Phys. Rev. Lett.* **125**, 067404 (2020).
- [100] M. Lupatini, “Polaron-polaritons and quantum Hall ferromagnetism in hole gases”, Doctoral Thesis (ETH Zurich, 2020).
- [101] C. Weisbuch, M. Nishioka, A. Ishikawa, and Y. Arakawa, “Observation of the coupled exciton-photon mode splitting in a semiconductor quantum microcavity”, *Phys. Rev. Lett.* **69**, 3314–3317 (1992).
- [102] A. Esser, R. Zimmermann, and E. Runge, “Theory of Trion Spectra in Semiconductor Nanostructures”, *Phys. Status Solidi B Basic Res.* **227**, 317–330 (2001).
- [103] D. Gammon, E. S. Snow, B. V. Shanabrook, D. S. Katzer, and D. Park, “Fine Structure Splitting in the Optical Spectra of Single GaAs Quantum Dots”, *Phys. Rev. Lett.* **76**, 3005–3008 (1996).
- [104] A. Bracker, E. Stinaff, D. Gammon, M. Ware, J. Tischler, D. Park, D. Gershoni, A. Filinov, M. Bonitz, F. Peeters, and C. Riva, “Binding energies of positive and negative trions: From quantum wells to quantum dots”, *Phys. Rev. B* **72**, 035332 (2005).
- [105] G. Ramon, R. Rappaport, A. Qarry, E. Cohen, A. Mann, A. Ron, and L. N. Pfeiffer, “Scattering of polaritons by a two-dimensional electron gas in a semiconductor microcavity”, *Phys. Rev. B* **65**, 085323 (2002).

-
- [106] S. Ravets, P. Knüppel, S. Faelt, O. Cotlet, M. Kroner, W. Wegscheider, and A. Imamoglu, “Polaron Polaritons in the Integer and Fractional Quantum Hall Regimes”, *Phys. Rev. Lett.* **120**, 057401 (2018).
- [107] M. Lupatini, “Spin Reversal of a Quantum Hall Ferromagnet at a Landau Level Crossing”, *Data Collect. ETH Zurich*, [10.3929/ethz-b-000422205](https://doi.org/10.3929/ethz-b-000422205) (2020).
- [108] R. Prange, M. Cage, K. Klitzing, S. Girvin, A. Chang, F. Duncan, M. Haldane, R. Laughlin, A. Pruisken, and D. Thouless, *The Quantum Hall Effect*, Graduate Texts in Contemporary Physics (Springer, New York, 1989).
- [109] Z. F. Ezawa and G. Tsitsishvili, “Quantum Hall ferromagnets”, *Rep. Prog. Phys.* **72**, 086502 (2009).
- [110] S. Das Sarma and A. Pinczuk, eds., *Perspectives in Quantum Hall Effects: Novel Quantum Liquids in Low-dimensional Semiconductor Structures*, A Wiley-Interscience Publication (John Wiley & Sons, 1997).
- [111] S. L. Sondhi, S. M. Girvin, J. P. Carini, and D. Shahar, “Continuous quantum phase transitions”, *Rev. Mod. Phys.* **69**, 315–333 (1997).
- [112] M. Steger, G. Liu, B. Nelsen, C. Gautham, D. W. Snoke, R. Balili, L. Pfeiffer, and K. West, “Long-range ballistic motion and coherent flow of long-lifetime polaritons”, *Phys. Rev. B* **88**, 235314 (2013).
- [113] J. Hayakawa, K. Muraki, and G. Yusa, “Real-space imaging of fractional quantum Hall liquids”, *Nat. Nanotechnol.* **8**, 31–35 (2013).
- [114] J. N. Moore, J. Hayakawa, T. Mano, T. Noda, and G. Yusa, “Optically Imaged Striped Domains of Nonequilibrium Electronic and Nuclear Spins in a Fractional Quantum Hall Liquid”, *Phys. Rev. Lett.* **118**, 076802 (2017).
- [115] J. B. Miller, I. P. Radu, D. M. Zumbühl, E. M. Levenson-Falk, M. A. Kastner, C. M. Marcus, L. N. Pfeiffer, and K. W. West, “Fractional quantum Hall effect in a quantum point contact at filling fraction $5/2$ ”, *Nature Phys* **3**, 561–565 (2007).

- [116] G. L. Paravicini-Bagliani, F. Appugliese, E. Richter, F. Valmorra, J. Keller, M. Beck, N. Bartolo, C. Rössler, T. Ihn, K. Ensslin, C. Ciuti, G. Scalari, and J. Faist, “Magneto-transport controlled by Landau polariton states”, *Nat. Phys.* **15**, 186 (2019).
- [117] K. Lai, W. Kundhikanjana, M. A. Kelly, Z.-X. Shen, J. Shabani, and M. Shayegan, “Imaging of Coulomb-Driven Quantum Hall Edge States”, *Phys. Rev. Lett.* **107**, 176809 (2011).
- [118] S. Ilani, J. Martin, E. Teitelbaum, J. H. Smet, D. Mahalu, V. Umansky, and A. Yacoby, “The microscopic nature of localization in the quantum Hall effect”, *Nature* **427**, 328–332 (2004).
- [119] K. Cong, G. T. Noe II, and J. Kono, “Excitons in Magnetic Fields”, in *Encyclopedia of Modern Optics* (Elsevier, 2018), pp. 63–81.
- [120] D. M. Whittaker and A. J. Shields, “Theory of X^- at high magnetic fields”, *Phys. Rev. B* **56**, 15185–15194 (1997).
- [121] I. Lerner and Y. E. Lozovik, “Two-dimensional electron-hole system in a strong magnetic field as an almost ideal exciton gas”, *Zh. Eksp. Teor. Fiz* **80**, 1488–1503 (1981).
- [122] D. C. Rogers, J. Singleton, R. J. Nicholas, C. T. Foxon, and K. Woodbridge, “Magneto-optics in GaAs-Ga_{1-x}Al_xAs quantum wells”, *Phys. Rev. B* **34**, 4002–4009 (1986).
- [123] A. Pinczuk, J. P. Valladares, D. Heiman, A. C. Gossard, J. H. English, C. W. Tu, L. Pfeiffer, and K. West, “Observation of roton density of states in two-dimensional Landau-level excitations”, *Phys. Rev. Lett.* **61**, 2701–2704 (1988).
- [124] P. Plochocka, J. M. Schneider, D. K. Maude, M. Potemski, M. Rappaport, V. Umansky, I. Bar-Joseph, J. G. Groshaus, Y. Gallais, and A. Pinczuk, “Optical Absorption to Probe the Quantum Hall Ferromagnet at Filling Factor $\nu = 1$ ”, *Phys. Rev. Lett.* **102**, 126806 (2009).
- [125] E. H. Aifer, B. B. Goldberg, and D. A. Broido, “Evidence of Skyrmion Excitations about $\nu = 1$ in n -Modulation-Doped Single Quantum Wells by Interband Optical Transmission”, *Phys. Rev. Lett.* **76**, 680–683 (1996).

-
- [126] J. G. Groshaus, V. Umansky, H. Shtrikman, Y. Levinson, and I. Bar-Joseph, “Absorption Spectrum Around $\nu = 1$: Evidence for a Small-Size Skyrmion”, *Phys. Rev. Lett.* **93**, 096802 (2004).
- [127] D. Heiman, B. B. Goldberg, A. Pinczuk, C. W. Tu, A. C. Gossard, and J. H. English, “Optical Anomalies of the Two-Dimensional Electron Gas in the Extreme Magnetic Quantum Limit”, *Phys. Rev. Lett.* **61**, 605–608 (1988).
- [128] B. B. Goldberg, D. Heiman, M. J. Graf, D. A. Broido, A. Pinczuk, C. W. Tu, J. H. English, and A. C. Gossard, “Optical transmission spectroscopy of the two-dimensional electron gas in GaAs in the quantum hall regime”, *Phys. Rev. B* **38**, 10131–10134 (1988).
- [129] A. J. Turberfield, S. R. Haynes, P. A. Wright, R. A. Ford, R. G. Clark, J. F. Ryan, J. J. Harris, and C. T. Foxon, “Optical detection of the integer and fractional quantum Hall effects in GaAs”, *Phys. Rev. Lett.* **65**, 637–640 (1990).
- [130] E. I. Rashba, “Excitons in incompressible quantum liquids”, *Pure Appl. Chem.* **67**, 409–418 (1995).
- [131] G. Yusa, H. Shtrikman, and I. Bar-Joseph, “Charged Excitons in the Fractional Quantum Hall Regime”, *Phys. Rev. Lett.* **87**, 216402 (2001).
- [132] S. Nomura, M. Yamaguchi, H. Tamura, T. Akazaki, Y. Hirayama, M. Korkusinski, and P. Hawrylak, “Photoluminescence fine structures in the fractional quantum Hall effect regime”, *Phys. Rev. B* **89**, 115317 (2014).
- [133] C. Kallin and B. I. Halperin, “Excitations from a filled Landau level in the two-dimensional electron gas”, *Phys. Rev. B* **30**, 5655–5668 (1984).
- [134] D. Paquet, T. M. Rice, and K. Ueda, “Two-dimensional electron-hole fluid in a strong perpendicular magnetic field: Exciton Bose condensate or maximum density two-dimensional droplet”, *Phys. Rev. B* **32**, 5208–5221 (1985).

- [135] T. Graß, O. Cotlet, A. İmamoğlu, and M. Hafezi, “Optical excitations in compressible and incompressible two-dimensional electron liquids”, [Phys. Rev. B **101**, 155127 \(2020\)](#).
- [136] K. J. Nash, M. S. Skolnick, M. K. Saker, and S. J. Bass, “Many body shakeup in quantum well luminescence spectra”, [Phys. Rev. Lett. **70**, 3115–3118 \(1993\)](#).
- [137] G. Finkelstein, H. Shtrikman, and I. Bar-Joseph, “Shakeup processes in the recombination spectra of negatively charged excitons”, [Phys. Rev. B **53**, 12593–12596 \(1996\)](#).
- [138] G. Finkelstein, H. Shtrikman, and I. Bar-Joseph, “Mechanism of shakeup processes in the photoluminescence of a two-dimensional electron gas at high magnetic fields”, [Phys. Rev. B **56**, 10326–10331 \(1997\)](#).
- [139] M. J. Manfra, B. B. Goldberg, L. Pfeiffer, and K. West, “Optical determination of the spin polarization of a quantum Hall ferromagnet”, [Physica E: Low-dimensional Systems and Nanostructures **1**, 28–35 \(1997\)](#).
- [140] I. V. Kukushkin, “Magneto-Optics of Composite Fermions and Skyrmions”, in *Strongly Correlated Fermions and Bosons in Low-Dimensional Disordered Systems*, edited by I. V. Lerner, B. L. Altshuler, V. I. Fal’ko, and T. Giamarchi (Springer Netherlands, Dordrecht, 2002), pp. 185–218.
- [141] J. Sinova, A. H. MacDonald, and S. M. Girvin, “Disorder and interactions in quantum Hall ferromagnets near $\nu = 1$ ”, [Phys. Rev. B **62**, 13579–13587 \(2000\)](#).
- [142] V. Zhitomirsky, R. Chughtai, R. J. Nicholas, and M. Henini, “Spin polarization of 2D electrons in the quantum Hall ferromagnet: evidence for a partially polarized state around filling factor one”, [Phys. E Low-Dimens. Syst. Nanostructures **12**, 12–15 \(2002\)](#).
- [143] S. L. Sondhi, A. Karlhede, S. A. Kivelson, and E. H. Rezayi, “Skyrmions and the crossover from the integer to fractional quantum Hall effect at small Zeeman energies”, [Phys. Rev. B **47**, 16419–16426 \(1993\)](#).

-
- [144] H. A. Fertig, L. Brey, R. Côté, and A. H. MacDonald, “Charged spin-texture excitations and the Hartree-Fock approximation in the quantum Hall effect”, *Phys. Rev. B* **50**, 11018–11021 (1994).
- [145] S. E. Barrett, G. Dabbagh, L. N. Pfeiffer, K. W. West, and R. Tycko, “Optically Pumped NMR Evidence for Finite-Size Skyrmions in GaAs Quantum Wells near Landau Level Filling $\nu = 1$ ”, *Phys. Rev. Lett.* **74**, 5112–5115 (1995).
- [146] R. Tycko, S. Barrett, G. Dabbagh, L. Pfeiffer, and K. West, “Electronic states in gallium arsenide quantum wells probed by optically pumped NMR”, *Science* **268**, 1460–1463 (1995).
- [147] A. Schmeller, J. P. Eisenstein, L. N. Pfeiffer, and K. W. West, “Evidence for Skyrmions and Single Spin Flips in the Integer Quantized Hall Effect”, *Phys. Rev. Lett.* **75**, 4290–4293 (1995).
- [148] S. M. Girvin, “Spin and Isospin: Exotic Order in Quantum Hall Ferromagnets”, *Physics Today* **53**, 39–45 (2000).
- [149] C. M. Townsley, R. Chughtai, R. J. Nicholas, and M. Henini, “Observation of skyrmions in a two-dimensional hole system”, *Phys. Rev. B* **71**, 073303 (2005).
- [150] L. Bryja, A. Wójs, and M. Potemski, “Quantum Hall skyrmions in a hole gas with a large spin gap”, *Phys. Rev. B* **73**, 241302 (2006).
- [151] Z. Schlesinger, S. J. Allen, Y. Yafet, A. C. Gossard, and W. Wiegmann, “Cyclotron resonance in the two-dimensional hole gas in (Ga,Al)As/GaAs heterostructures”, *Phys. Rev. B* **32**, 5231–5236 (1985).
- [152] S. J. Hawkesworth, S. Hill, T. J. B. M. Janssen, J. M. Chamberlain, J. Singleton, U. Ekenberg, G. M. Summers, G. A. Davies, R. J. Nicholas, E. C. Valadares, M. Henini, and J. A. A. J. Perenboom, “Cyclotron resonance of high-mobility GaAs/AlGaAs (311) 2DHGs”, *Semicond. Sci. Technol.* **8**, 1465–1469 (1993).
- [153] B. E. Cole, J. M. Chamberlain, M. Henini, T. Cheng, W. Batty, A. Wittlin, J. A. A. J. Perenboom, A. Ardavan, A. Polisski, and J. Singleton, “Cyclotron resonance in ultra-low-hole-density narrow p-type GaAs/(Al,Ga)As quantum wells”, *Phys. Rev. B* **55**, 2503–2511 (1997).

- [154] M. Kubisa, L. Bryja, K. Ryczko, J. Misiewicz, C. Bardot, M. Potemski, G. Ortner, M. Bayer, A. Forchel, and C. B. Sørensen, “Photoluminescence investigations of two-dimensional hole Landau levels in p-type single $\text{Al}_x\text{Ga}_{1-x}\text{As}/\text{GaAs}$ heterostructures”, *Phys. Rev. B* **67**, 035305 (2003).
- [155] F. Fischer, R. Winkler, D. Schuh, M. Bichler, and M. Grayson, “Transport evidence of the lowest Landau-level spin-index anticrossing in (110) GaAs two-dimensional holes”, *Phys. Rev. B* **75**, 073303 (2007).
- [156] Y. Liu, S. Hasdemir, D. Kamburov, A. L. Graninger, M. Shayegan, L. N. Pfeiffer, K. W. West, K. W. Baldwin, and R. Winkler, “Even-denominator fractional quantum Hall effect at a Landau level crossing”, *Phys. Rev. B* **89**, 165313 (2014).
- [157] Y. Liu, S. Hasdemir, M. Shayegan, L. N. Pfeiffer, K. W. West, and K. W. Baldwin, “Unusual Landau level pinning and correlated $\nu = 1$ quantum Hall effect in hole systems confined to wide GaAs quantum wells”, *Phys. Rev. B* **92**, 195156 (2015).
- [158] D. R. Leadley, R. J. Nicholas, D. K. Maude, A. N. Utjuzh, J. C. Portal, J. J. Harris, and C. T. Foxon, “Searches for skyrmions in the limit of zero g -factor”, *Semicond. Sci. Technol.* **13**, 671–679 (1998).
- [159] S. P. Shukla, M. Shayegan, S. R. Parihar, S. A. Lyon, N. R. Cooper, and A. A. Kiselev, “Large skyrmions in an $\text{Al}_{0.13}\text{Ga}_{0.87}\text{As}$ quantum well”, *Phys. Rev. B* **61**, 4469–4472 (2000).
- [160] R. Winkler, *Spin-orbit coupling effects in two-dimensional electron and hole systems*, Springer Tracts in Modern Physics v. 191 (Springer, Berlin Heidelberg, 2003).
- [161] D. A. Abanin, S. A. Parameswaran, S. A. Kivelson, and S. L. Sondhi, “Nematic valley ordering in quantum Hall systems”, *Phys. Rev. B* **82**, 035428 (2010).
- [162] Y. P. Shkolnikov, S. Misra, N. C. Bishop, E. P. De Poortere, and M. Shayegan, “Observation of Quantum Hall “Valley Skyrmions””, *Phys. Rev. Lett.* **95**, 066809 (2005).

-
- [163] M. Padmanabhan, T. Gokmen, and M. Shayegan, “Ferromagnetic Fractional Quantum Hall States in a Valley-Degenerate Two-Dimensional Electron System”, *Phys. Rev. Lett.* **104**, 016805 (2010).
- [164] T. Gokmen and M. Shayegan, “Density and strain dependence of $\nu = 1$ energy gap in a valley-degenerate AlAs quantum well”, *Phys. Rev. B* **81**, 115336 (2010).
- [165] A. Kumar, S. A. Parameswaran, and S. L. Sondhi, “Microscopic theory of a quantum Hall Ising nematic: Domain walls and disorder”, *Phys. Rev. B* **88**, 045133 (2013).
- [166] B. E. Feldman, M. T. Randeria, A. Gyenis, F. Wu, H. Ji, R. J. Cava, A. H. MacDonald, and A. Yazdani, “Observation of a nematic quantum Hall liquid on the surface of bismuth”, *Science* **354**, 316–321 (2016).
- [167] M. S. Hossain, M. A. Mueed, M. K. Ma, Y. J. Chung, L. N. Pfeiffer, K. W. West, K. W. Baldwin, and M. Shayegan, “Anomalous coupling between magnetic and nematic orders in quantum Hall systems”, *Phys. Rev. B* **98**, 081109 (2018).
- [168] B. B. Goldberg, D. Heiman, A. Pinczuk, L. Pfeiffer, and K. West, “Optical investigations of the integer and fractional quantum Hall effects: Energy plateaus, intensity minima, and line splitting in band-gap emission”, *Phys. Rev. Lett.* **65**, 641–644 (1990).
- [169] M. Byszewski, B. Chwalisz, D. K. Maude, M. L. Sadowski, M. Potemski, T. Saku, Y. Hirayama, S. Studenikin, D. G. Austing, A. S. Sachrajda, and P. Hawrylak, “Optical probing of composite fermions in a two-dimensional electron gas”, *Nat. Phys.* **2**, 239–243 (2006).
- [170] J. P. Eisenstein, H. L. Stormer, L. N. Pfeiffer, and K. W. West, “Evidence for a spin transition in the $\nu = 2/3$ fractional quantum Hall effect”, *Phys Rev B* **41**, 7910–7913 (1990).
- [171] B. Verdene, J. Martin, G. Gamez, J. Smet, K. von Klitzing, D. Mahalu, D. Schuh, G. Abstreiter, and A. Yacoby, “Microscopic manifestation of the spin phase transition at filling factor $2/3$ ”, *Nature Phys* **3**, 392–396 (2007).

- [172] J. H. Blokland, P. C. M. Christianen, B. M. Ashkinadze, V. V. Rudenkov, L. N. Pfeiffer, and J. C. Maan, “Optical probing of electronic fractional quantum Hall states”, *Phys. Rev. B* **81**, 201304 (2010).
- [173] L. V. Kulik, A. S. Zhuravlev, V. E. Bisti, V. E. Kirpichev, M. N. Khannanov, and I. V. Kukushkin, “Resonance reflection of light from a $\nu = 1/3$ Laughlin liquid”, *Jetp Lett.* **100**, 581–584 (2015).
- [174] E. Wigner, “On the Interaction of Electrons in Metals”, *Phys. Rev.* **46**, 1002–1011 (1934).
- [175] C. C. Grimes and G. Adams, “Evidence for a Liquid-to-Crystal Phase Transition in a Classical, Two-Dimensional Sheet of Electrons”, *Phys. Rev. Lett.* **42**, 795–798 (1979).
- [176] J. Yoon, C. C. Li, D. Shahar, D. C. Tsui, and M. Shayegan, “Wigner Crystallization and Metal-Insulator Transition of Two-Dimensional Holes in GaAs at $B = 0$ ”, *Phys. Rev. Lett.* **82**, 1744–1747 (1999).
- [177] I. Shapir, A. Hamo, S. Pecker, C. P. Moca, Ö. Legeza, G. Zarand, and S. Ilani, “Imaging the electronic Wigner crystal in one dimension”, *Science* **364**, 870–875 (2019).
- [178] Y. E. Lozovik and V. Yudson, “Crystallization of a two-dimensional electron gas in a magnetic field”, *ZhETF Pisma Redaktsiui* **22**, 26 (1975).
- [179] T. Smoleński, P. E. Dolgirev, C. Kuhlenkamp, A. Popert, Y. Shimazaki, P. Back, X. Lu, M. Kroner, K. Watanabe, T. Taniguchi, I. Esterlis, E. Demler, and A. Imamoğlu, “Signatures of Wigner crystal of electrons in a monolayer semiconductor”, *Nature* **595**, 53–57 (2021).
- [180] M. Stern, P. Plochocka, V. Umansky, D. K. Maude, M. Potemski, and I. Bar-Joseph, “Optical Probing of the Spin Polarization of the $\nu = 5/2$ Quantum Hall State”, *Phys. Rev. Lett.* **105**, 096801 (2010).
- [181] L. Tiemann, G. Gamez, N. Kumada, and K. Muraki, “Unraveling the Spin Polarization of the $\nu = 5/2$ Fractional Quantum Hall State”, *Science* **335**, 828–831 (2012).

-
- [182] X. Lin, R. Du, and X. Xie, “Recent experimental progress of fractional quantum Hall effect: 5/2 filling state and graphene”, [National Science Review](#) **1**, 564–579 (2014).
- [183] L. Du, U. Wurstbauer, K. W. West, L. N. Pfeiffer, S. Fallahi, G. C. Gardner, M. J. Manfra, and A. Pinczuk, “Observation of new plasmons in the fractional quantum Hall effect: Interplay of topological and nematic orders”, [Sci. Adv.](#) **5**, eaav3407 (2019).
- [184] A. S. Zhuravlev, A. B. Van’kov, L. V. Kulik, I. V. Kukushkin, V. E. Kirpichev, J. H. Smet, K. v. Klitzing, V. Umansky, and W. Wegscheider, “Inelastic light scattering study of the $\nu = 1$ quantum Hall ferromagnet”, [Phys. Rev. B](#) **77**, 155404 (2008).
- [185] B. A. Piot, W. Desrat, D. K. Maude, D. Kazazis, A. Cavanna, and U. Gennser, “Disorder-Induced Stabilization of the Quantum Hall Ferromagnet”, [Phys. Rev. Lett.](#) **116**, 106801 (2016).
- [186] J. Nakamura, S. Liang, G. C. Gardner, and M. J. Manfra, “Direct observation of anyonic braiding statistics”, [Nat. Phys.](#) **16**, 931–936 (2020).
- [187] H. Bartolomei, M. Kumar, R. Bisognin, A. Marguerite, J.-M. Berroir, E. Bocquillon, B. Plaças, A. Cavanna, Q. Dong, U. Gennser, Y. Jin, and G. Fève, “Fractional statistics in anyon collisions”, [Science](#) **368**, 173–177 (2020).
- [188] T. Chervy, P. Knüppel, H. Abbaspour, M. Lupatini, S. Fält, W. Wegscheider, M. Kroner, and A. Imamoğlu, “Accelerating Polaritons with External Electric and Magnetic Fields”, [Phys. Rev. X](#) **10**, 011040 (2020).
- [189] P. Knüppel, “Accelerating Polaritons with External Electric and Magnetic Fields”, [Data Collect. ETH Zurich](#), [10.3929/ethz-b-000387816](#) (2020).
- [190] L. Lu, J. D. Joannopoulos, and M. Soljačić, “Topological photonics”, [Nat. Photonics](#) **8**, 821–829 (2014).
- [191] T. Ozawa, H. M. Price, A. Amo, N. Goldman, M. Hafezi, L. Lu, M. C. Rechtsman, D. Schuster, J. Simon, O. Zilberberg, and I. Carusotto, “Topological photonics”, [Rev. Mod. Phys.](#) **91**, 015006 (2019).

- [192] J. L. O'Brien, A. Furusawa, and J. Vučković, "Photonic quantum technologies", *Nat. Photonics* **3**, 687–695 (2009).
- [193] N. Engheta, "Circuits with Light at Nanoscales: Optical Nanocircuits Inspired by Metamaterials", *Science* **317**, 1698–1702 (2007).
- [194] H.-T. Lim, E. Togan, M. Kroner, J. Miguel-Sanchez, and A. Imamoğlu, "Electrically tunable artificial gauge potential for polaritons", *Nat Commun* **8**, 1–6 (2017).
- [195] T. Karzig, C.-E. Bardyn, N. H. Lindner, and G. Refael, "Topological Polaritons", *Phys. Rev. X* **5**, 031001 (2015).
- [196] O. Bleu, D. D. Solnyshkov, and G. Malpuech, "Measuring the quantum geometric tensor in two-dimensional photonic and exciton-polariton systems", *Phys. Rev. B* **97**, 195422 (2018).
- [197] Á. Gutiérrez-Rubio, L. Chirulli, L. Martín-Moreno, F. J. García-Vidal, and F. Guinea, "Polariton Anomalous Hall Effect in Transition-Metal Dichalcogenides", *Phys. Rev. Lett.* **121**, 137402 (2018).
- [198] S. Klemmt, T. H. Harder, O. A. Egorov, K. Winkler, R. Ge, M. A. Bandres, M. Emmerling, L. Worschech, T. C. H. Liew, M. Segev, C. Schneider, and S. Höfling, "Exciton-polariton topological insulator", *Nature* **562**, 552–556 (2018).
- [199] D. Sanvitto, F. Pulizzi, A. J. Shields, P. C. M. Christianen, S. N. Holmes, M. Y. Simmons, D. A. Ritchie, J. C. Maan, and M. Pepper, "Observation of Charge Transport by Negatively Charged Excitons", *Science* **294**, 837–839 (2001).
- [200] F. Pulizzi, D. Sanvitto, P. Christianen, A. Shields, S. Holmes, M. Simmons, D. Ritchie, M. Pepper, and J. Maan, "Optical imaging of trion diffusion and drift in GaAs quantum wells", *Phys. Rev. B* **68**, 205304 (2003).
- [201] D. V. Kulakovskii and Y. E. Lozovik, "Screening and rearrangement of excitonic states in double layer systems", *J. Exp. Theor. Phys.* **98**, 1205–1213 (2004).
- [202] O. L. Berman, R. Y. Kezerashvili, and Y. E. Lozovik, "Can we move photons?", *Physics Letters A* **374**, 3681–3684 (2010).

-
- [203] O. L. Berman, R. Y. Kezerashvili, and Y. E. Lozovik, “Drag effects in a system of electrons and microcavity polaritons”, *Phys. Rev. B* **82**, 125307 (2010).
- [204] B. N. Narozhny and A. Levchenko, “Coulomb drag”, *Rev. Mod. Phys.* **88**, 025003 (2016).
- [205] D. M. Myers, B. Ozden, J. Beaumariage, L. N. Pfeiffer, K. West, and D. W. Snoke, *Pushing Photons with Electrons: Observation of the Polariton Drag Effect*, (2018) [arXiv:1808.07866 \[cond-mat\]](https://arxiv.org/abs/1808.07866).
- [206] I. Y. Chestnov, Y. G. Rubo, and A. V. Kavokin, “Pseudo-drag of a polariton superfluid”, *Phys. Rev. B* **100**, 085302 (2019).
- [207] O. Cotlet, F. Pientka, R. Schmidt, G. Zarand, E. Demler, and A. Imamoglu, “Transport of Neutral Optical Excitations Using Electric Fields”, *Phys. Rev. X* **9**, 041019 (2019).
- [208] F. Haupt, A. Imamoglu, and M. Kroner, “Single Quantum Dot as an Optical Thermometer for Millikelvin Temperatures”, *Phys. Rev. Applied* **2**, 024001 (2014).
- [209] D. Fritzsche, “Heterostructures in MODFETs”, *Solid-State Electronics* **30**, 1183–1195 (1987).
- [210] S. M. Sze and K. K. Ng, *Physics of semiconductor devices* (John Wiley & Sons, Hoboken, New Jersey, 2006).
- [211] M. J. Kane, N. Apsley, D. A. Anderson, L. L. Taylor, and T. Kerr, “Parallel conduction in GaAs/Al_xGa_{1-x}As modulation doped heterojunctions”, *J. Phys. C: Solid State Phys.* **18**, 5629–5636 (1985).
- [212] M. Reed, W. Kirk, and P. Kobiela, “Investigation of parallel conduction in GaAs/Al_xGa_{1-x}As modulation-doped structures in the quantum limit”, *IEEE J. Quantum Electron.* **22**, 1753–1759 (1986).
- [213] D. A. Syphers, K. P. Martin, and R. J. Higgins, “Determination of transport coefficients in high mobility heterostructure systems in the presence of parallel conduction”, *Appl. Phys. Lett.* **49**, 534–536 (1986).

- [214] G. Gregoris, J. Beerens, S. B. Amor, L. Dmowski, J. C. Portal, D. L. Sivco, and A. Y. Cho, “A study of parallel conduction and the quantum Hall effect in GaInAs-AlInAs heterojunctions using magnetotransport measurements under hydrostatic pressure”, *J. Phys. C Solid State Phys.* **20**, 425–440 (1987).
- [215] S. Baer and K. Ensslin, *Transport Spectroscopy of Confined Fractional Quantum Hall Systems*, Vol. 183, Springer Series in Solid-State Sciences (Springer International Publishing, 2015).
- [216] G. Panzarini, L. C. Andreani, A. Armitage, D. Baxter, M. S. Skolnick, V. N. Astratov, J. S. Roberts, A. V. Kavokin, M. R. Vladimirova, and M. A. Kaliteevski, “Exciton-light coupling in single and coupled semiconductor microcavities: Polariton dispersion and polarization splitting”, *Phys. Rev. B* **59**, 5082–5089 (1999).
- [217] P. F. Fontein, J. A. Kleinen, P. Hendriks, F. A. P. Blom, J. H. Wolter, H. G. M. Lochs, F. A. J. M. Driessen, L. J. Giling, and C. W. J. Beenakker, “Spatial potential distribution in GaAs/Al_xGa_{1-x}As heterostructures under quantum Hall conditions studied with the linear electro-optic effect”, *Phys. Rev. B* **43**, 12090–12093 (1991).
- [218] M. Cage and C. Lavine, “Potential and Current Distributions Calculated Across A Quantum Hall-Effect Sample at Low and High Currents”, *J. Res. Natl. Inst. Stand. Technol.* **100**, 529 (1995).
- [219] K. V. Kavokin, I. A. Shelykh, A. V. Kavokin, G. Malpuech, and P. Bigenwald, “Quantum Theory of Spin Dynamics of Exciton-Polaritons in Microcavities”, *Phys. Rev. Lett.* **92**, 017401 (2004).
- [220] M. Onoda, S. Murakami, and N. Nagaosa, “Hall Effect of Light”, *Phys. Rev. Lett.* **93**, 083901 (2004).
- [221] A. Kavokin, G. Malpuech, and M. Glazov, “Optical Spin Hall Effect”, *Phys. Rev. Lett.* **95**, 136601 (2005).
- [222] C. Leyder, M. Romanelli, J. P. Karr, E. Giacobino, T. C. H. Liew, M. M. Glazov, A. V. Kavokin, G. Malpuech, and A. Bramati, “Observation of the optical spin Hall effect”, *Nature Phys* **3**, 628–631 (2007).

-
- [223] A. Amo, T. C. H. Liew, C. Adrados, E. Giacobino, A. V. Kavokin, and A. Bramati, “Anisotropic optical spin Hall effect in semiconductor microcavities”, *Phys. Rev. B* **80**, 165325 (2009).
- [224] M. Maragkou, C. E. Richards, T. Ostatnický, A. J. D. Grundy, J. Zajac, M. Hugues, W. Langbein, and P. G. Lagoudakis, “Optical analogue of the spin Hall effect in a photonic cavity”, *Opt. Lett.*, **OL** **36**, 1095–1097 (2011).
- [225] K. Lekenta, M. Król, R. Mirek, K. Łempicka, D. Stephan, R. Mazur, P. Morawiak, P. Kula, W. Piecek, P. G. Lagoudakis, B. Piętka, and J. Szczytko, “Tunable optical spin Hall effect in a liquid crystal microcavity”, *Light Sci Appl* **7**, 1–6 (2018).
- [226] A. Gianfrate, O. Bleu, L. Dominici, V. Ardizzone, M. De Giorgi, D. Ballarini, G. Lerario, K. W. West, L. N. Pfeiffer, D. D. Solnyshkov, D. Sanvitto, and G. Malpuech, “Measurement of the quantum geometric tensor and of the anomalous Hall drift”, *Nature* **578**, 381–385 (2020).
- [227] S. M. Girvin, “Spin and Isospin: Exotic Order in Quantum Hall Ferromagnets”, in *The Multifaceted Skyrmion*, edited by M. Rho and I. Zahed (World Scientific, 2015), pp. 351–365.
- [228] J. Nakamura, S. Fallahi, H. Sahasrabudhe, R. Rahman, S. Liang, G. C. Gardner, and M. J. Manfra, “Aharonov–Bohm interference of fractional quantum Hall edge modes”, *Nat. Phys.* **15**, 563–569 (2019).
- [229] P. Knüppel, S. Ravets, M. Kroner, S. Fält, W. Wegscheider, and A. Imamoglu, “Nonlinear optics in the fractional quantum Hall regime”, *Nature* **572**, 91–94 (2019).
- [230] P. Knüppel, “Nonlinear optics in the fractional quantum Hall regime”, *Data Collect. ETH Zurich*, [10.3929/ethz-b-000338463](https://doi.org/10.3929/ethz-b-000338463) (2019).
- [231] L. Ferrier, E. Wertz, R. Johne, D. D. Solnyshkov, P. Senellart, I. Sagnes, A. Lemaître, G. Malpuech, and J. Bloch, “Interactions in Confined Polariton Condensates”, *Phys. Rev. Lett.* **106**, 126401 (2011).
- [232] Y. Sun, P. Wen, Y. Yoon, G. Liu, M. Steger, L. N. Pfeiffer, K. West, D. W. Snoke, and K. A. Nelson, “Bose-Einstein Condensation of Long-Lifetime Polaritons in Thermal Equilibrium”, *Phys. Rev. Lett.* **118**, 016602 (2017).

- [233] N. Takemura, S. Trebaol, M. Wouters, M. T. Portella-Oberli, and B. Deveaud, “Polaritonic Feshbach resonance”, *Nat. Phys.* **10**, 500–504 (2014).
- [234] P. Cristofolini, G. Christmann, S. I. Tsintzos, G. Deligeorgis, G. Konstantinidis, Z. Hatzopoulos, P. G. Savvidis, and J. J. Baumberg, “Coupling Quantum Tunneling with Cavity Photons”, *Science*, 1219010 (2012).
- [235] I. Rosenberg, D. Liran, Y. Mazuz-Harpaz, K. West, L. Pfeiffer, and R. Rapaport, “Strongly interacting dipolar-polaritons”, *Sci. Adv.* **4**, eaat8880 (2018).
- [236] E. Togan, H.-T. Lim, S. Faelt, W. Wegscheider, and A. Imamoglu, “Enhanced Interactions between Dipolar Polaritons”, *Phys. Rev. Lett.* **121**, 227402 (2018).
- [237] P. Stepanov, I. Amelio, J.-G. Rousset, J. Bloch, A. Lemaître, A. Amo, A. Minguzzi, I. Carusotto, and M. Richard, “Dispersion relation of the collective excitations in a resonantly driven polariton fluid”, *Nat Commun* **10**, 3869 (2019).
- [238] R. W. Boyd, *Nonlinear Optics* (Elsevier, Amsterdam, 2008).
- [239] K. L. Hall, G. Lenz, E. P. Ippen, and G. Raybon, “Heterodyne pump–probe technique for time-domain studies of optical nonlinearities in waveguides”, *Opt. Lett.*, **OL 17**, 874–876 (1992).
- [240] A. Mecozzi and J. Mørk, “Transient and time-resolved four-wave mixing with collinear pump and probe pulses using the heterodyne technique”, *Pure Appl. Opt.* **7**, 335 (1998).
- [241] B. Patton, U. Woggon, and W. Langbein, “Coherent Control and Polarization Readout of Individual Excitonic States”, *Phys. Rev. Lett.* **95**, 266401 (2005).
- [242] V. Kohnle, Y. Léger, M. Wouters, M. Richard, M. T. Portella-Oberli, and B. Deveaud, “Four-wave mixing excitations in a dissipative polariton quantum fluid”, *Phys. Rev. B* **86**, 064508 (2012).
- [243] G. Nardin, T. M. Autry, K. L. Silverman, and S. T. Cundiff, “Multidimensional coherent photocurrent spectroscopy of a semiconductor nanostructure”, *Opt. Express* **21**, 28617 (2013).

-
- [244] C. L. Smallwood and S. T. Cundiff, “Multidimensional Coherent Spectroscopy of Semiconductors”, *Laser & Photonics Reviews* **12**, 1800171 (2018).
- [245] M. Wouters and I. Carusotto, “Excitations in a Nonequilibrium Bose-Einstein Condensate of Exciton Polaritons”, *Phys. Rev. Lett.* **99**, 140402 (2007).
- [246] J. Keeling and N. G. Berloff, “Spontaneous Rotating Vortex Lattices in a Pumped Decaying Condensate”, *Phys. Rev. Lett.* **100**, 250401 (2008).
- [247] A. S. Brichkin, S. I. Novikov, A. V. Larionov, V. D. Kulakovskii, M. M. Glazov, C. Schneider, S. Höfling, M. Kamp, and A. Forchel, “Effect of Coulomb interaction on exciton-polariton condensates in GaAs pillar microcavities”, *Phys. Rev. B* **84**, 195301 (2011).
- [248] A. V. Nalitov, D. D. Solnyshkov, N. A. Gippius, and G. Malpuech, “Voltage control of the spin-dependent interaction constants of dipolaritons and its application to optical parametric oscillators”, *Phys. Rev. B* **90**, 235304 (2014).
- [249] O. Cotlet, “Bose - Fermi mixtures with electrons and polaritons”, Doctoral Thesis (ETH Zurich, 2019).
- [250] Á. Cuevas et al., “First observation of the quantized exciton-polariton field and effect of interactions on a single polariton”, *Sci. Adv.* **4**, eaa06814 (2018).
- [251] B. Besga, C. Vaneph, J. Reichel, J. Estève, A. Reinhard, J. Miguel-Sánchez, A. Imamoglu, and T. Volz, “Polariton Boxes in a Tunable Fiber Cavity”, *Phys. Rev. Appl.* **3**, 014008 (2015).
- [252] D. Najer, I. Söllner, P. Sekatski, V. Dolique, M. C. Löbl, D. Riedel, R. Schott, S. Starosielec, S. R. Valentin, A. D. Wieck, N. Sangouard, A. Ludwig, and R. J. Warburton, “A gated quantum dot strongly coupled to an optical microcavity”, *Nature* **575**, 622–627 (2019).
- [253] M. Salz, Y. Herrmann, A. Nadarajah, A. Stahl, M. Hettrich, A. Stacey, S. Praver, D. Hunger, and F. Schmidt-Kaler, “Cryogenic platform for coupling color centers in diamond membranes to a fiber-based microcavity”, *Appl. Phys. B* **126**, 131 (2020).

- [254] Y. Fontana, R. Zifkin, E. Janitz, C. D. R. Rosenblueth, and L. Childress, “A mechanically stable and tunable cryogenic Fabry–Pérot microcavity”, *Rev. Sci. Instrum.* **92**, 053906 (2021).
- [255] S. Vadia, J. Scherzer, H. Thierschmann, C. Schäfermeier, C. D. Savio, T. Taniguchi, K. Watanabe, D. Hunger, K. Karraï, and A. Högele, *Open-cavity in closed-cycle cryostat as a quantum optics platform*, (2021) [arXiv:2103.05619](https://arxiv.org/abs/2103.05619) [[cond-mat](#), [physics:physics](#), [physics:quant-ph](#)].
- [256] J. H. Strait, G. Holland, W. Zhu, C. Zhang, B. R. Ilic, A. Agrawal, D. Pacifici, and H. J. Lezec, “Revisiting the Photon-Drag Effect in Metal Films”, *Phys. Rev. Lett.* **123**, 053903 (2019).
- [257] I. Y. Chestnov, S. M. Arakelian, and A. V. Kavokin, “Giant synthetic gauge field for spinless microcavity polaritons in crossed electric and magnetic fields”, *New J. Phys.* **23**, 023024 (2021).
- [258] M. J. Hartmann, F. G. S. L. Brandão, and M. B. Plenio, “Strongly interacting polaritons in coupled arrays of cavities”, *Nature Phys* **2**, 849–855 (2006).
- [259] I. Carusotto, D. Gerace, H. E. Tureci, S. De Liberato, C. Ciuti, and A. Imamoglu, “Fermionized Photons in an Array of Driven Dissipative Nonlinear Cavities”, *Phys. Rev. Lett.* **103**, 033601 (2009).
- [260] B. Nelsen, G. Liu, M. Steger, D. W. Snoke, R. Balili, K. West, and L. Pfeiffer, “Dissipationless Flow and Sharp Threshold of a Polariton Condensate with Long Lifetime”, *Phys. Rev. X* **3**, 041015 (2013).
- [261] J. Jang, H. M. Yoo, L. N. Pfeiffer, K. W. West, K. W. Baldwin, and R. C. Ashoori, “Full momentum- and energy-resolved spectral function of a 2D electronic system”, *Science* **358**, 901–906 (2017).
- [262] H. M. Yoo, K. W. Baldwin, K. West, L. Pfeiffer, and R. C. Ashoori, “Spin phase diagram of the interacting quantum Hall liquid”, *Nat. Phys.* **16**, 1022–1027 (2020).
- [263] F. P. Laussy, T. Taylor, I. A. Shelykh, and A. V. Kavokin, “Superconductivity with excitons and polaritons: review and extension”, *JNP* **6**, 064502 (2012).

-
- [264] O. Cotlet, S. Zeytinoğlu, M. Sigrist, E. Demler, and A. Imamoglu, “Superconductivity and other collective phenomena in a hybrid Bose-Fermi mixture formed by a polariton condensate and an electron system in two dimensions”, *Phys. Rev. B* **93**, 054510 (2016).
- [265] K. F. Mak and J. Shan, “Photonics and optoelectronics of 2D semiconductor transition metal dichalcogenides”, *Nature Photon* **10**, 216–226 (2016).
- [266] Y. Zhang, Y.-W. Tan, H. L. Stormer, and P. Kim, “Experimental observation of the quantum Hall effect and Berry’s phase in graphene”, *Nature* **438**, 201–204 (2005).
- [267] K. S. Novoselov, Z. Jiang, Y. Zhang, S. V. Morozov, H. L. Stormer, U. Zeitler, J. C. Maan, G. S. Boebinger, P. Kim, and A. K. Geim, “Room-Temperature Quantum Hall Effect in Graphene”, *Science* **315**, 1379–1379 (2007).
- [268] K. I. Bolotin, F. Ghahari, M. D. Shulman, H. L. Stormer, and P. Kim, “Observation of the fractional quantum Hall effect in graphene”, *Nature* **462**, 196–199 (2009).
- [269] Y. Cao, V. Fatemi, A. Demir, S. Fang, S. L. Tomarken, J. Y. Luo, J. D. Sanchez-Yamagishi, K. Watanabe, T. Taniguchi, E. Kaxiras, R. C. Ashoori, and P. Jarillo-Herrero, “Correlated insulator behaviour at half-filling in magic-angle graphene superlattices”, *Nature* **556**, 80–84 (2018).
- [270] X. Lu, P. Stepanov, W. Yang, M. Xie, M. A. Aamir, I. Das, C. Urgell, K. Watanabe, T. Taniguchi, G. Zhang, A. Bachtold, A. H. MacDonald, and D. K. Efetov, “Superconductors, orbital magnets and correlated states in magic-angle bilayer graphene”, *Nature* **574**, 653–657 (2019).

List of Figures and Tables

List of Figures

2.1	Band structure and material properties of gallium arsenide. . .	16
2.2	Gallium arsenide quantum well and allowed optical transitions. . .	17
2.3	Optical microcavity based on distributed Bragg reflectors. . .	20
2.4	Polariton anticrossing and energy-momentum dispersion relation.	23
2.5	Integer and fractional quantum Hall effects.	27
2.6	Spectroscopy of a 2D hole gas as function of hole density. . .	30
2.7	Cryogenic optical setups.	33
2.8	Electron temperature estimation.	34
2.9	Lens configurations of the optical microscopy setup.	35
2.10	Sample heterostructures along their growth direction.	39
2.11	Conduction band diagram for sample A.	41
2.12	Processed sample chip and contacting for sample C.	43
2.13	Polaron-polariton formation in a GaAs QW.	46
2.14	Polaron-polariton formation at different densities.	48
3.1	Optical transitions in a magnetic field perpendicular to the 2DEG plane.	53
3.2	Landau level spectroscopy and coupling to QH states in sample B. Comparison between absorption (reflectivity) and emission in a region without optical cavity.	55
3.3	Polarization resolved Landau level spectroscopy for sam- ple C. Comparison of white light reflectivity spectra with and without optical cavity in the IQH regime.	59

3.4	Cavity spectroscopy of sample A in the IQH regime, as we tune B for fixed E_{cav}	60
3.5	Electronic spin polarization in sample A around $\nu = 1$ and evidence for skyrmions.	62
3.6	Landau level crossing and associated hole spin flip of the ground state in sample C and depolarization of the QH ferromagnet.	66
3.7	Cavity spectroscopy in the fractional quantum Hall regime, sample A.	68
3.8	Cavity spectroscopy in the QH regime for sample B.	71
3.9	Emission from sample B* without cavity in the FQH regime and feature of electronic incompressibility.	73
3.10	Polaron-polariton energy-momentum dispersion around $\nu = 2/5$	74
3.11	FQH regime below $\nu = 1/3$ and beyond $\nu = 1$	75
3.12	Light sensitivity of sample A, investigated at the $\nu = 1$ plateau.	77
3.13	Features of incoherent emission at higher energy excitation.	79
4.1	Polariton Hall bar device structure and electrical contacts.	86
4.2	Electrical transport characteristics of the Hall bar device.	89
4.3	Schematic of the free space optical setup.	90
4.4	Map of the Hall bar LP emission energy.	92
4.5	Linear polarization eigenbasis of the Hall bar.	93
4.6	Electrically controlled polariton landscape via density gradients.	95
4.7	Additional evidence for density gradients.	99
4.8	Polariton acceleration in density gradients.	99
4.9	Coupled oscillator model for the polariton acceleration.	103
4.10	Polariton acceleration in external electric and magnetic fields.	104
4.11	Spin density gradients in the QH regime.	106
4.12	Spin-selective polariton acceleration.	109
5.1	Quantum Hall polariton resonances—linear spectroscopy.	116
5.2	Polaron-Polariton characterization at $\nu = 2/5$	117
5.3	Optical setup for four-wave mixing experiments.	118

5.4	FWM traces and power dependence obtained for $\nu = 2/5$. . .	123
5.5	Enhancing interactions between quantum Hall polaritons at fractional filling factors.	125
5.6	Additional FWM data from sample B.	127
5.7	Polariton characterization for the depleted QW.	129
5.8	Comparing FWM data to GPE predictions for an intrinsic QW.	132
5.9	Estimation of interaction constant at $2/5$	134
5.10	Increase in polariton coherence time at FQH states.	137

List of Tables

2.1	Binary DBR mirror etching recipe.	42
2.2	Summary of the electrical and optical sample characterization.	44
4.1	Polariton Hall bar fabrication steps.	87
4.2	Polariton dispersion curve-fitting parameters.	97
5.1	Summary of interaction constants and linewidths.	135

Acknowledgments

I am deeply grateful to my supervisor Ataç İmamoğlu. A true role model for being a good scientist, his passion and constructive attitude were an endless source of inspiration. It is a privilege to be immersed in his outstanding team. I would like to thank all members and guests of the Quantum Photonics Group for the productive and enjoyable times spent together. This thesis would not have been possible without the nurturing support of Martin Kroner. He provided invaluable advice in all matters ranging from conceptual questions to the most technical details and was always listening to my concerns.

I was exceptionally lucky to start my journey with Sylvain Ravets. With passion, integrity, optimism and zest he was leading the way. It was a great pleasure to follow suit, pushing against the boundaries of our knowledge together. I am extremely grateful to Thibault Chervy, who became my second mentor. He kept me on my toes to keep exploring new directions and broadened my understanding of the scientific community, how to contribute and thrive.

Many people collaborated with me and contributed to my research and personal growth: thank you! Aymeric Delteil for taking me under his wing early on and together with Yves Delley for inviting me into their world of quantum dots. Yuta Tsuchimoto, my first collaborator and friend ever since. Werner Wegscheider and Stefan Fält for collaborating continuously on revisions of our samples. Everything I know about cleanroom fabrication I owe to Emre Togan. Mirko Lupatini and Mansour Shayegan for our hole gas adventures. Tomasz Smoleński for being a physicist in pursuit of excellence like no other, inspiring everyone around him to catch up. For the fruitful collaborations: Hadis Abbaspour, Ovidiu Cotlet, Nicola Dietler, Thomas Fink,

Acknowledgments

Hyang-Tag Lim, Shima Rajabali, Gian-Marco Schnüriger, Roland Winkler and Sun Zhe. For her vital support: Manuela Weber-Semler.

I am grateful to some especially helpful individuals, among them Andrea Bergschneider, Livio Ciorciaro, Xiaobo Lu, Peter Märki, Puneet Murthy, Alexander Popert and Yuya Shimazaki. For many enlightening discussions and their valuable advice, I want to thank Jacqueline Bloch, Antoine Browaeys, Iacopo Carusotto, Eugene Demler, Tobias Donner, Dmitri Efetov, Jérôme Faist, Tobias Grass, Mohammad Hafezi, Thomas Ihn, Jan Klärs, Giacomo Scalari, Richard Schmidt, Ajit Srivastava, Jacek Szczytko, Sina Zeytinoğlu and Oded Zilberberg.

I appreciate all the friendly interactions that added to my life inside and outside of the labs; in particular around hiking, bouldering, card games and coffee table discussions including Ivan Amelio, Patrick Back, Francesco Colangelo, Bertrand Evrard, Felix Helmrich, Olivier Huber, Fabian Kaufmann, Natasha Kiper, Clemens Kuhlenkamp, Tobia Nova, Ido Schwartz, Meinrad Sidler, Li Bing Tan, Deepankur Thureja and many others.

Excellent teachers deserve credit for inspiring me to pursue the sciences. First and foremost, my physics teacher Rolf Heeb who enthusiastically shared his passion and curiosity for nature and the beauty of physics. I would like to extend my thanks to his exceptional crew of mentors and young aspiring scientists that make up academia Wattwil.

Family and friends—thank you for your unwavering support and patience. Harriet & Peter Knüppel, to whom I owe everything. Sophia Erni for our companionship; Michaja Bösch and Nando Helbling for the cheerful times, together with Simon Frei for always keeping me on track.

Curriculum Vitae

Personal Details

Name	Patrick Knüppel
Born	June 7, 1992 in Stade, Germany
Citizenship	Austrian and German
E-mail	quantumhallpolaritons@gmail.com

Education

2017–2021	Doctoral Studies in Experimental Physics at the Institute for Quantum Electronics, ETH Zurich
2015–2016	Master of Science in Physics, ETH Zurich
2011–2014	Bachelor of Science in Physics, ETH Zurich
2007–2011	Matura, High School Wattwil, Switzerland

Publication List

- (1) M. Lupatini, P. Knüppel, S. Faelt, R. Winkler, M. Shayegan, A. Imamoglu, and W. Wegscheider, “Spin Reversal of a Quantum Hall Ferromagnet at a Landau Level Crossing”, *Phys. Rev. Lett.* **125**, 067404 (2020).
- (2) T. Chervy, P. Knüppel, H. Abbaspour, M. Lupatini, S. Fält, W. Wegscheider, M. Kroner, and A. Imamoglu, “Accelerating Polaritons with External Electric and Magnetic Fields”, *Phys. Rev. X* **10**, 011040 (2020).
- (3) T. Smoleński, O. Cotlet, A. Popert, P. Back, Y. Shimazaki, P. Knüppel, N. Dietler, T. Taniguchi, K. Watanabe, M. Kroner, and A. Imamoglu, “Interaction-Induced Shubnikov–de Haas Oscillations in Optical Conductivity of Monolayer MoSe₂”, *Phys. Rev. Lett.* **123**, 097403 (2019).
- (4) P. Knüppel, S. Ravets, M. Kroner, S. Fält, W. Wegscheider, and A. Imamoglu, “Nonlinear optics in the fractional quantum Hall regime”, *Nature* **572**, 91–94 (2019).
- (5) S. Ravets, P. Knüppel, S. Faelt, O. Cotlet, M. Kroner, W. Wegscheider, and A. Imamoglu, “Polaron Polaritons in the Integer and Fractional Quantum Hall Regimes”, *Phys. Rev. Lett.* **120**, 057401 (2018).
- (6) Y. Tsuchimoto, P. Knüppel, A. Delteil, Z. Sun, M. Kroner, and A. Imamoglu, “Proposal for a quantum interface between photonic and superconducting qubits”, *Phys. Rev. B* **96**, 165312 (2017).